UNIVERSITY OF CALIFORNIA SAN DIEGO

First Principles Modeling of Lithium Solid Electrolytes

A dissertation submitted in partial satisfaction of the
requirements for the degree
Doctor of Philosophy

in

NanoEngineering

by

Zhi Deng

Committee in charge:

Professor Shyue Ping Ong, Chair
Professor Jian Luo
Professor Francesco Paesani
Professor Yu Qiao
Professor Kesong Yang

2018

The dissertation of Zhi Deng is approved, and it is acceptable in quality and form for publication on microfilm and electronically:

_____

_____

_____

_____

_____

Chair

University of California San Diego

2018

TABLE OF CONTENTS

LIST OF FIGURES

LIST OF TABLES

ACKNOWLEDGMENTS

First and foremost, I would like to express my gratitude to my advisor, Dr. Shyue Ping Ong, for constantly offering me guidance and support along the way finishing this thesis. His high standards, not only in pursuing scientific research, but also in many other aspects, have helped me explore my potential as a computational material scientist and a better professional. I am also grateful to the current and previous members of my dissertation committee, Dr. Jian Luo, Dr. Francesco Paesani, Dr. Yu Qiao, Dr. Kesong Yang and Dr. Shirley Meng, for their insightful advice on my research work.

My special appreciation goes to my collaborators in the Materials Virtual Lab (MAVRL), Dr. Iek-Heng Chu, Dr. Balachandran Radhakrishnan, Dr. Zhenbin Wang, Zhuoying Zhu, Dr. Chi Chen, Dr. Xiang-Guo Li and Hanmei Tang. It is hard to imagine finishing this thesis without your contributions or inspirations taken from casual discussions with you. My acknowledgments also go to all my colleagues in MAVRL for making graduate school at UC San Diego a lifelong memory. I would also thank experimental collaborators in Dr. Shirley Meng's lab, Han Nguyen, Dr. Sunny Hy, Erik Wu and Dr. Abhik Banerjee, for sharing their expertise from an entirely different perspective.

Last but not least, my deepest gratitude goes to my parents for their unconditional love and support. To my girlfriend, Xiao Yu, I thank you for always being there, hearing me out on either my joy of success or pain of frustration. I could not have completed this bittersweet journey without your love.

Chapter 3, in part, is a reprint of the material "Data-Driven First-Principles Methods for the Study and Design of Alkali Superionic Conductors" as it appears in Chemistry of Materials, Zhi Deng, Zhuoying Zhu, Iek-Heng Chu and Shyue Ping Ong, 2016, 29 (1). pp 281-288. The dissertation author was the primary investigator and author of this paper.

Chapter 4, in full, is a reprint of the material "Elastic Properties of Alkali Superionic Conductor Electrolytes from First Principles Calculations" as it appears in Journal of the Elec-

trochemical Society, Zhi Deng, Zhenbin Wang, Iek-Heng Chu, Jian Luo and Shyue Ping Ong, 2016, 163 (2), pp A67-A74. The dissertation author was the primary investigator and author of this paper. The data calculations were done by collaborator, Zhenbin Wang.

Chapter 5, in full, is a reprint of the material "Rational Composition Optimization of the Lithium-Rich $Li_3OCl_{1-x}Br_x$ Anti-Perovskite Superionic Conductors" as it appears in Chemistry of Materials, Zhi Deng, Balachandran Radhakrishnan and Shyue Ping Ong, 2015, 27 (10), pp 3749-3755. The dissertation author was the primary investigator and author of this paper.

Chapter 6, in full, is currently being prepared for submission for publication of the material "An Electrostatic Spectral Neighbor Analysis Potential (eSNAP) for Lithium Nitride", Zhi Deng, Chi Chen, Xiang-Guo Li and Shyue Ping Ong. The dissertation author was the primary investigator and author of this paper.

VITA

2013	B. E. in Materials Science and Engineering, Tsinghua University
2015	M. S. in NanoEngineering, University of California San Diego
2018	Ph. D. in NanoEngineering, University of California San Diego

PUBLICATIONS

Z. Deng, C. Chen, X.-G. Li and S. P. Ong, "An Electrostatic Spectral Neighbor Analysis Potential (eSNAP) for Lithium Nitride," *In preparation*.

Z. Deng, Z. Zhu, I.-H. Chu, and S. P. Ong, "Data-Driven First-Principles Methods for the Study and Design of Alkali Superionic Conductors," *Chemistry of Materials*, 2017, vol. 29, pp. 281–288.

Z. Deng, Y. Mo, and S. P. Ong, "Computational studies of solid-state alkali conduction in rechargeable alkali-ion batteries," *NPG Asia Materials*, 2016, vol. 8, p. e254.

Z. Deng, Z. Wang, I.-H. Chu, J. Luo, and S. P. Ong, "Elastic Properties of Alkali Superionic Conductor Electrolytes from First Principles Calculations," *Journal of The Electrochemical Society*, 2016, vol. 163, pp. A67–A74.

Z. Deng, B. Radhakrishnan, and S. P. Ong, "Rational Composition Optimization of the Lithium-Rich $Li_3OCl_{1-x}Br_x$ Anti-Perovskite Superionic Conductors," *Chemistry of Materials*, 2015, vol. 27, pp. 3749–3755.

ABSTRACT OF THE DISSERTATION

First Principles Modeling of Lithium Solid Electrolytes

by

Zhi Deng

Doctor of Philosophy in NanoEngineering

University of California San Diego, 2018

Professor Shyue Ping Ong, Chair

Developing all-solid-state lithium batteries with inorganic solid electrolytes can potentially address the safety concerns caused by using flammable organic liquid electrolytes in traditional lithium-ion batteries. Though the discovery of new solid electrolytes with exceptionally high (on par or even exceeding organic solvents) ionic conductivities have re-energized all-solid-state lithium battery research in recent years, many practical challenges remain, hindering large-scale applications. In this thesis, we demonstrate how density functional theory (DFT) calculations can be used to provide crucial materials insights to address these challenges. This thesis is broadly divided into two topics.

In the first topic (Chapters 3 and 4), we will investigate bulk solid electrolyte properties

such as ionic conductivity, diffusion mechanisms, electrochemical stability and mechanical properties using DFT calculations. We will show that Li excess interstitials are crucial to achieving reasonable ionic conductivity in Li_6PS_5Cl by promoting diffusion between Li_6S cages. Li_6PS_5Cl is also shown to be metastable with limited intrinsic electrochemical window. We have also carried out a large scale study of the elastic properties of most known alkali solid electrolyte candidates, quantifying relationships between the chemistry and mechanical properties.

In the second topic (Chapters 5 and 6), we develop approaches to apply atomistic-level DFT calculated data to probe diffusion at much larger length scales. By combining bond percolation analysis with DFT-calculated local-environment dependent diffusion barriers, we identify composition ranges with potentially improved ionic conductivities in the anti-perovskite $Li_3OCl_xBr_{1-x}$ superionic conductor. We also demonstrate how large-scale DFT calculations can be used to train a quantum-accurate interatomic potential for Li_3N. This electrostatic Spectral Neighbor Analysis Potential (eSNAP), which combines a rigorously defined local environment descriptor with an electrostatic model, is then applied to large scale transport studies that are well outside the accessibility of expensive *ab initio* molecular dynamics (AIMD), such as the computation of thermodynamic factors and grain boundary diffusivity.

Chapter 1

Introduction

Today, with one of the highest energy densities among known energy storage technologies, rechargeable lithium-ion (Li-ion) battery has become ubiquitous in powering consumer electronics. In addition, Li-ion battery is finding increasingly large-scale applications, such as electric or hybrid vehicles and grid energy storage.

Despite the successful commercialization of rechargeable Li-ion battery as early as 1991, safety hazards still remain primarily due to the usage of flammable organic solvents in the electrolytes. These safety risks will be severely magnified in large-scale energy storage applications. A strategy to potentially address the safety concerns is replacing the organic liquid electrolyte with an inorganic solid electrolyte, making the battery all-solid-state. Besides diminished flammability, other possible benefits for developing all-solid-state batteries include extended battery cycle life, absence of electrolyte leakage or vaporization and ease of miniaturization.[4, 5]

In this chapter, we first briefly discuss the requirements for electrolyte materials in Li-ion batteries from the operation mechanism. Then, we dive into the history of lithium solid electrolytes, and discuss some unique requirements to be fulfilled for solid electrolytes. The chapter concludes with the objectives and over view of this thesis.

1.1 Lithium-Ion Battery

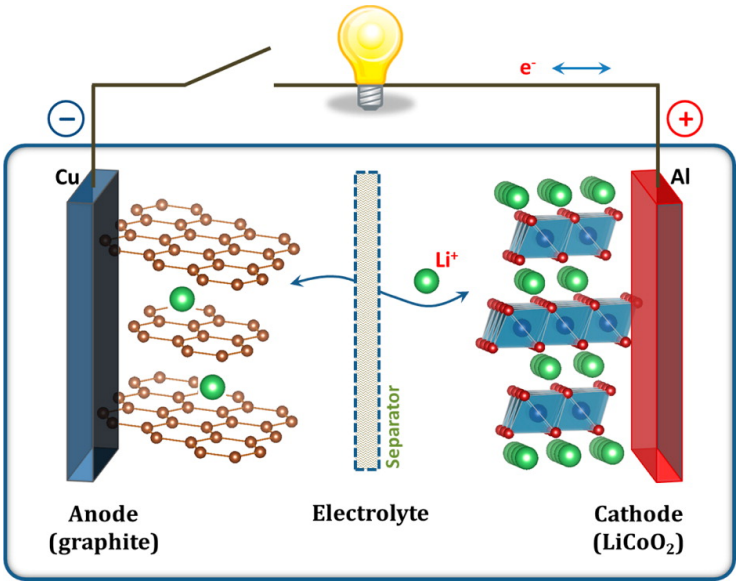

Figure 1.1: Schematic illustration of a rechargeable Li-ion battery.[1]

Figure 1.1 shows a schematic of a rechargeable Li-ion battery. During discharge, Li ions are transported from the high chemical potential component - anode, through the electrolyte, to the low chemical potential component - cathode. In the meantime, energy is released in the form of electrical work by the electrons traveling through the external circuit from anode to cathode. The battery is charged by applying a voltage on the electrodes, and Li ions and electrons travel backwards through the electrolyte and the external circuit, respectively.

The operation mechanism of Li-ion battery clearly reveals the requirements for electrolyte. An ideal electrolyte should be an ionic conductor allowing the transportation of Li ions, and an electronic insulator forcing the electrons to travel through external circuit and suppressing battery self-discharge. In addition, an electrolyte should be electrochemically stable within a wide Li chemical potential range to enable the usage of high voltage cathode-anode pairs.

In all-solid-state lithium batteries, inorganic lithium superionic conductors are used as solid electrolytes, replacing the conventional organic liquid electrolytes. Inorganic lithium solid electrolytes are generally good electronic insulators due to the dominance of ionic bondings in

these materials. However, historically the ionic conductivity of inorganic lithium solid electrolytes has been unsatisfactory, leading to issues such as low power density in most all-solid-state lithium batteries. As a benchmark, the typical organic electrolyte, a solvent mixture of a cyclic carbonate (e.g., ethylene carbonate, EC) and a linear carbonate (e.g., dimethylcarbonate, DMC) with $LiPF_6$ salt, has a Li conductivity on the order of 10 mS/cm at room temperature.[6] Research on all-solid-state lithium batteries has been extensively focused on developing solid electrolytes with high ionic conductivity, in the hope of achieving ionic conductivity comparable to or even higher than that in organic liquid electrolytes.

1.2 Inorganic Solid Electrolytes

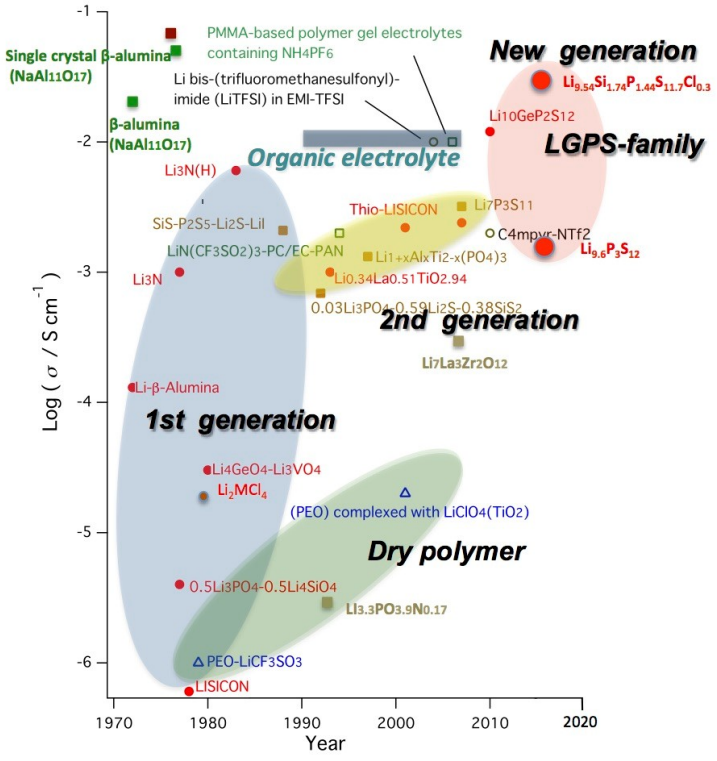

Figure 1.2: History of lithium superionic conductors.[2]

Figure 1.2 shows the history of the development of lithium superionic conductors and

achieved room temperature ionic conductivities. The first generation materials were found along the discovery of superionic conduction phenomena, including lithium nitride Li_3N, LISICON $Li_{14}Zn(GeO_4)_4$[7] and LISICON-like materials (e.g., Li_4GeO_4-Li_3VO_4[8] and Li_3PO_4-Li_4SiO_4[9]). The LISICON and LISICON-like materials generally have poor ionic conductivity. Though Li_3N exhibits higher ionic conductivity than others, its high chemical instability has hindered its applications as solid electrolyte in batteries. The second generation materials emerged along with the commercialization and further optimization of Li-ion batteries, including NASICON-like LATP $Li_{1+x}Al_xTi_{2-x}(PO_4)_3$[10], perovskite LLTO $(Li, La)TiO_3$[11], thio-LISICON Li_3PS_4-Li_4GeS_4[12], Li_2S-P_2S_5 glass-cermaic $Li_7P_3S_{11}$[13] and garnet LLZO $Li_7La_3Zr_2O_{12}$[14]. The ionic conductivities of the second generation materials are on the order of 1 mS/cm. The only exception is garnet LLZO of which the ionic conductivity is 1 order of magnitude lower, but it is particularly interesting because of its extraordinary stability against lithium metal anode, the "Holy Grail" for all lithium batteries.[14] Thio-LISICON shares similar crystal structure with LISICON, and the substitution of oxygen with more polarizable sulfur has boosted the ionic conductivity by 2 - 3 orders of magnitude.[12] This finding opened up the opportunities in the sulfide chemistries as potential solid electrolytes, and eventually led to the development of the next generation. The discovery of LGPS $Li_{10}Ge_2PS_{12}$ marks the beginning of the third generation materials. Similar in chemistry but completely different in crystal structure, LGPS has a room temperature ionic conductivity of 12 mS/cm, which is 1 order of magnitude higher than that in thio-LISICON, and is even comparable to organic liquid electrolyte.[15] Recently, two more materials belonging to the LGPS family were reported, one being $Li_{9.54}Si_{1.74}P_{1.44}S_{11.7}Cl_{0.3}$ with highest room temperature ionic conductivity of 25 mS/cm so far, and the other one being $Li_{9.6}P_3S_{12}$ with slightly lower ionic conductivity but good stability against lithium metal.[16]

In addition to high ionic conductivity, good electrochemical stability is another factor that needs to be taken into consideration in applying a superionic conductor as solid electrolyte. And it is the fundamental reason why garnet LLZO and $Li_{9.6}P_3S_{12}$ are more attractive despite their

relatively low ionic conductivities. The LGPS material was previously claimed to be stable up to 5 V vs. Li/Li^+ from conventional cyclic voltammetry (CV) measurements.[15] However, it was later found to have rather limited electrochemical window from theoretical predictions,[17, 18] and it is supported from refined CV measurements where the electrochemical window of LGPS is between 1.7 to 2.1 V vs. Li/Li^+.[19] In fact, from theoretical calculations, nearly all known solid electrolyte candidates have limited electrochemical window.[18] Similar to the formation of a stable SEI for liquid electrolytes, most claimed electrochemical stable cases in solid electrolytes may be attributed to the passivation at the interface. Other interfacial engineering approaches, such as artificial coating layer, may also protect solid electrolytes from the extreme electrochemical conditions at both cathode and anode.

High ionic conductivity and good electrochemical stability are the requirements for all electrolyte materials, whether in liquid or solid state. For solid electrolytes, suitable mechanical properties are also desired, and less attention has been paid in this perspective. One of the critical challenge in all-solid-state batteries is achieving an intimate conformal contact between solid electrolyte and electrodes in battery fabrication and maintaining it during battery operation. Typical commercial cathodes (e.g., $LiCoO_2$, $LiMn_2O_4$ and $LiFePO_4$) and anodes (e.g., graphitic carbons) exhibit strains of up to 10% during electrochemical cycling due to the insertion and extraction of Li ions.[20] The solid electrolyte should be able to deform without the formation of cracks or pores to maintain the interfacial contact during these volume changes. Therefore, a less rigid solid electrolyte is preferred in this case to accommodate large strains without having large stress response. On the other hand, as a potential strategy in enabling lithium metal anode, a solid electrolyte should be able to suppress the formation of lithium dendrite during cycling.[21] A more rigid solid electrolyte with high shear modulus and hardness would be more suitable here.[22]

1.3 Objectives and Overview

Despite the great progress made on discovering lithium superionic conductors, the factors that determine the ionic conductivity in materials remain poorly understood. Understanding the mechanism of superionic conduction may assist in optimizing known materials with room for improvements. The knowledge may also serve as a guideline in discovering new materials. Moreover, other properties for a solid electrolyte, such as electrochemical stability and mechanical properties, are closely related to the electrode/electrolyte interfacial issues in all-solid-state lithium batteries. The buried nature of solid-solid interface has made experimental probing extremely difficult. The mechanical properties are in principle intrinsic for a material, but experimental measurements are usually highly dependent on other various factors.

First principles calculations based on density functional theory (DFT) have been widely applied in studying materials in Li-ion batteries.[23, 24] The simulations based directly on physical laws may provide unique insights on the atomic scale without any experimental input, thus assisting the interpretation of experimental observations. With the growing of computational power and the proper design of infrastructure and database for high-throughput DFT calculations,[25, 26, 27] we are able to realize *in silico* material design and provide guidelines for experiments using the predictions made.

In this thesis, we focus on investigating the critical properties for solid electrolyte materials using first principles calculations. This thesis is broadly divided into two topics. In the first topic, we will investigate bulk solid electrolyte properties such as ionic conductivity, diffusion mechanisms, electrochemical stability and mechanical properties using DFT calculations. In the second topic, we develop approaches to apply atomistic-scale DFT calculated data to probe diffusion at much larger length scales. A brief description for each subsequent chapter is listed as follows:

- Chapter 2 provides an overview of methods for modeling solid electrolytes using first

principles calculations.

- Chapter 3 presents a complete evaluation of argyrodite Li_6PS_5Cl as solid electrolyte from first principles calculations, including its phase stability, electrochemical stability and ionic conductivity.

- Chapter 4 presents a comprehensive investigation on the elastic properties of known superionic conductors aiming to fill the knowledge gap of mechanical properties for all solid electrolyte candidates.

- Chapter 5 presents a rational composition optimization strategy for maximizing the ionic conductivity of lithium-rich antiperovskite $Li_3OCl_{1-x}Br_x$ guided by a combination of first principles calculations and percolation theory.

- Chapter 6 presents a quantum-accurate force field for ionic systems in attempt to dissociate the limitations of first principles calculations. We use lithium nitride Li_3N as an example to showcase the development of the force field from machine learning methods. We also apply the force field in large scale diffusion modelings of Li_3N, which is impossible in the restraint of first principles calculations.

- Chapter 7 summarizes the advances made in this thesis and provides an outlook on future developments for first principles modeling of solid electrolytes.

Chapter 2

Methods

In this thesis, material property assessments rely heavily on the computation of total energies for any given atomic arrangements. First principles calculations can provide accurate total energy estimation from physical laws. In addition, molecular dynamics (MD) is an indispensable tool for modeling transport properties, such as ionic conductivity, a critical metric for Li solid electrolytes.

This chapter begins with a brief overview of the density functional theory (DFT), the core theory enabling material modeling using quantum mechanics, followed by a short discussion on the high-throughput DFT calculation infrastructure and the simulations and analyses powered by it. Then we briefly present the fundamentals of MD simulations, followed by some important transport properties obtained from MD. Next we present an automated workflow implementation for automated *ab initio* MD (AIMD) simulations, the primary tool for modeling transport properties used in this thesis. In the end, we discuss the limitations associated with AIMD and propose a strategy in attempting to address them.

2.1 Ground State Energies from Density Functional Theory

2.1.1 Many-Body Schrödinger Equation

Under the Born-Oppenheimer approximation where the nuclei are fixed, determining the ground state energy of a system with N electrons (located at coordinates $\mathbf{r}_1, \mathbf{r}_1, \ldots, \mathbf{r}_n$) involves solving the time-independent many-body Schrödinger equation:

$$\hat{H}\Psi = E\Psi, \tag{2.1}$$

where the Hamiltonian $\hat{H}$ contains kinetic, electron-electron interaction and electron-nuclei interaction terms. The wave function $\Psi(\mathbf{r}_1, \mathbf{r}_1, \ldots, \mathbf{r}_n)$ depends only on the coordinates of electrons. Since the many-body wave function contains $3N$ degrees of freedom, the problem is simply intractable to solve directly for larger systems with more than a few electrons.

2.1.2 The Hohenberg-Kohn Theorems and the Kohn-Sham Equation

The density functional theory (DFT) was first put on a firm theoretical footing in the framework of the Hohenberg-Kohn (H-K) theorems. The H-K theorems state that the electron density $n(\mathbf{r})$ is uniquely determined for any system of interacting particles in an external potential, and a universal functional for the energy is defined in terms of the density and the ground state is the global minimum of this functional.[28] The central variable in DFT is the electron density instead of the many-body wave function. The conceptual difference has significantly reduced the difficulty in solving the Schrödinger equation from $3N$ electron coordinates to electron density in 3 spatial coordinates.

Though H-K theorems prove the existence of the density functional, the expression for the functional remains unknown. DFT became a practically useful theory only after Kohn and Sham proposed their ansatz. The Kohn-Sham (K-S) approach involves mapping the interacting

system to a fictitious auxiliary system of non-interacting electrons with an effective K-S potential such that the ground state electron density is identical to that in the interacting system.[29] The total energy from K-S equation is written as:

$$E_{KS}[n] = T_s[n] + \int V_{ext}(\mathbf{r})n(\mathbf{r})\mathrm{d}^3\mathbf{r} + E_H[n] + E_{xc}[n], \tag{2.2}$$

where V_{ext} is the external potential acting on the electrons due to the nuclei, T_s is the independent-particle kinetic energy

$$T_s = \frac{1}{2}\sum_i \int |\nabla\phi_i|^2 \mathrm{d}^3\mathbf{r}, \tag{2.3}$$

E_H is the Hartree (or Coulomb) energy of electrons

$$E_H = \int \frac{n(\mathbf{r})n(\mathbf{r}')}{|\mathbf{r}-\mathbf{r}'|}\mathrm{d}^3\mathbf{r}\mathrm{d}^3\mathbf{r}', \tag{2.4}$$

and E_{xc} is the exchange and correlation energy accounting for the interactions among electrons.

2.1.3 Exchange-Correlation Approximations

The K-S approach would be theoretically exact, if the exact exchange-correlation functional were known. However, the exchange-correlation functional is approximated in practice. In the simplest possible assumption, the local-density approximation (LDA) uses the exchange and correlation energy of the homogeneous gas on realistic systems (molecules and solids). LDA is known to overbind.[30] A straightforward way to refine the LDA is to add a gradient of the density, leading to the generalized-gradient approximation (GGA). GGA will effectively fix the overbinding issues due to applying LDA in realistic systems.[30]

2.1.4 Solving the K-S Equation for Periodic Systems

For periodic systems such as crystalline solids, solving the K-S equation involves the integration of plane-wave basis functions in reciprocal space over the Brillouin Zone. The plane-wave expansion needs to be truncated at certain energy cutoff since the solutions with lower energies are more physically important than those with higher energies. Both *k*-point density and energy cutoff need to be carefully selected to ensure the convergence DFT calculations while keeping the computational cost low.

In addition, a common strategy to reduce the computational cost is applying pseudopotentials instead of considering all electrons in a solid. In this approach, only valence electrons are allowed to participate in assorted chemical bondings, while the core electrons are "frozen", being considered together with the nuclei as rigid non-polarizable ion cores.

2.2 High-Throughput DFT Calculation Infrastructure

Although first principles calculations based on DFT should in essence be accurate and parameter-free, certain approximations and parameter selections are still inevitable in practice. A high-throughput DFT calculation infrastructure aims at evaluating the properties of thousands of known crystalline solids. Except for the crystal structure, other inputs required for a DFT calculation are chosen in a consistent manner to ensure convergence of results and compatibility for different runs.

In this thesis, we adopt the same high-throughput infrastructure used by the Materials Project (MP).[25] All DFT calculations were performed using the Vienna *ab initio* Simulation Package (VASP)[31] within the projector augmented-wave method[32]. The GGA functional developed by Perdew, Burke and Ernzerhof (PBE)[33] was applied exclusively unless otherwise stated. The choice of pseudopotential, plane-wave energy cutoff and *k*-point density was made consistently with MP. In particular, an energy cutoff of 520 eV and a *k*-point density of at least

1000/(number of atoms in unit cell) were applied in spin-polarized total energy calculations. The conjugate gradient method was used where optimizing the nuclei configuration is needed.[34]

The high-throughput infrastructure has enabled numerous simulations and analyses to be performed in a manner where the crystal structure is the only input. For instance, the calculations of full elastic tensors used in Chapter 4, and the nudged elastic band calculations used in Chapter 5 modeling the transition state of vacancy migration along specific paths. Most important of all, it provides a set of well tested settings in earlier works[17, 35] for running *ab initio* molecular dynamics (AIMD) simulations, a method used for modeling ion transportations in solid electrolytes in this thesis. Last but not least, thermodynamic analyses used in Chapter 3 where constructing phase diagrams is involved, have been a lot more efficient with the data already available in MP database.

All VASP interfacing and post-processing including assorted analyses were performed using the Python Materials Genomics (pymatgen) library.[26]

2.3 Molecular Dynamics Simulations

2.3.1 Fundamentals of Molecular Dynamics

Molecular dynamics (MD) is a computer simulation technique for studying the motions of atoms and molecules. Atoms and molecules in the system are allowed to interact during the time period of simulation, giving a view of the dynamic evolution of the system. In each timestep, the trajectories of atoms and molecules are propagated following Newtonian dynamics, where the forces on particles and the potential energy of the system are determined using either empirical interatomic potentials or quantum mechanical methods. MD has been widely applied in the field of materials science as a modeling approach for atomistic simulations.

The description of interatomic interactions is the key that enables MD simulations. Classical MD is powered by empirical potentials. The functional form of these potentials are drastically

simplified with only a few fitting parameters to satisfy physical considerations. Therefore, evaluating potential energy from empirical potentials is cheap enough to support simulations on larger systems ($>$ 1000 particles) or for longer periods of time ($>$ 1ns). However, the numerical accuracy of empirical potentials is necessarily limited by the approximations made in selecting the functional form. Moreover, the specific functional isgenerally not transferable to another system with different bonding types.

Given the structural and chemical complexity in known solid electrolyte candidates, classical MD may not be suitable due to the limited transferability and questionable accuracy associated with empirical potentials. Especially for newly discovered materials, a properly fitted potential may not be available. Evaluating the interatomic interactions using quantum mechanical methods, such as DFT, can overcome the issues with empirical potentials. The resulted *ab initio* MD (AIMD) simulations have good transferability regardless of bonding types and chemistries. The accuracy from quantum mechanics is more trustworthy even if certain approximations are inevitable in DFT calculations. On the other hand, since the evaluation of energy and forces for each timestep requires solving the Schrödinger equation, high computational cost is inevitable for running AIMD simulations.

2.3.2 Applications in Modeling Solid Electrolytes

In the studies for solid electrolytes, a variety of properties related to ionic conduction can be obtained in MD simulations. The self-diffusivity of Li D^* is calculated from the trajectories using the Einstein relation:

$$D^* = \frac{1}{2dt}\langle[\mathbf{r}(t) - \mathbf{r}(0)]^2\rangle, \tag{2.5}$$

where t is time and d is the number of dimensions where diffusion occurs, and $\langle[\mathbf{r}(t) - \mathbf{r}(0)]^2\rangle$ is the mean square displacement (MSD) averaged over all diffusion atoms. The conductivity of Li

σ is calculated using the Nernst-Einstein equation:

$$\sigma = \frac{\rho z^2 F^2}{RT} D_\sigma, \tag{2.6}$$

where ρ is the molar density of Li, z is the charge of Li ion (+1), F is the Faraday constant, and R is the gas constant. The charge diffusivity D_σ is related to the self-diffusivity according to

$$D^* = \Theta D_\sigma, \tag{2.7}$$

where Θ is a thermodynamic factor. For dilute non-interacting systems such as ideal gases, the charge diffusivity is nearly identical to the self-diffusivity and $\Theta = 1$. Otherwise, a value much larger than 1 is expected for Θ.

In principle, with the combination of Equations 2.5, 2.6 and 2.7, the ionic conductivity of a solid electrolyte can be computed directly from the trajectories generated in an MD simulation. However, it is impractical to do so at ambient temperatures due to the poor Li mobility in solid electrolytes. The lack of ion hopping events observed during low-temperature MD simulations will make the diffusivities extremely difficult to converge. In order to achieve convergence within limited MD duration, the simulations are usually performed at elevated temperatures. Under the assumption of no phase transitions and an abundance of mobile defect carriers, the diffusivity in a solid typically follows an Arrhenius relationship:

$$D = D_0 \exp(-\frac{E_a}{kT}), \tag{2.8}$$

where D_0 is the maximum self-diffusivity at infinite temperature, E_a is the overall activation energy of diffusion, and k is the Boltzmann constant. The diffusivities obtained at high temperatures can then be extrapolated to lower temperatures using Equation 2.8.

In addition to the calculations of diffusivities and conductivities, other important properties

related to ionic conduction, such as the diffusion pathways and correlated motions of charge carriers, can also be obtained by analyzing the trajectories from MD simulations.

2.4 Automated AIMD Workflow

For studying Li diffusion in solid electrolytes, the length of an AIMD simulation is typically tens to hundreds of picoseconds to ensure the convergence of diffusivity. In this thesis, we apply several strategies to keep the computational cost for running AIMD simulations low. For example, a constant volume (NVT) ensemble is chosen over a constant pressure (NpT) ensemble since the latter requires higher plane-wave energy cutoff to avoid Pulay stress error arising from volume variation. Further computational cost savings is achieved by switching off spin polarization, using a lower plane-wave energy cutoff ($<$ 400 eV, varies with chemistry) and a sparser Γ point only *k*-mesh, etc.

Despite assorted budget saving efforts, the calculations will still last for days or even weeks, well beyond the wall times of typical supercomputing clusters. Besides, simulations at multiple temperatures are often required for extrapolation. The traditional approach of performing AIMD simulations are therefore in need of significant human intervention, with a high likelihood of errors. To address this challenge, we have developed an automated AIMD workflow using FireWorks[27], a workflow management software. Figure 2.1 shows the schematic of a typical AIMD workflow for Li diffusion studies. The crystal structure is first relaxed to an optimized geometry, from which a sufficiently large simulation supercell box is created. Then, AIMD jobs with different targeting temperatures are dynamically added to the workflow. Each AIMD job is running with a "WallTimeHandler" implemented in Custodian library[37], which terminates the job gracefully just prior to the wall time limit. A continuation job is then resubmitted until a pre-defined set of convergence criteria (e.g., a maximum number of time steps, etc.) is reached. Using this workflow, AIMD simulations can be performed with minimal human intervention

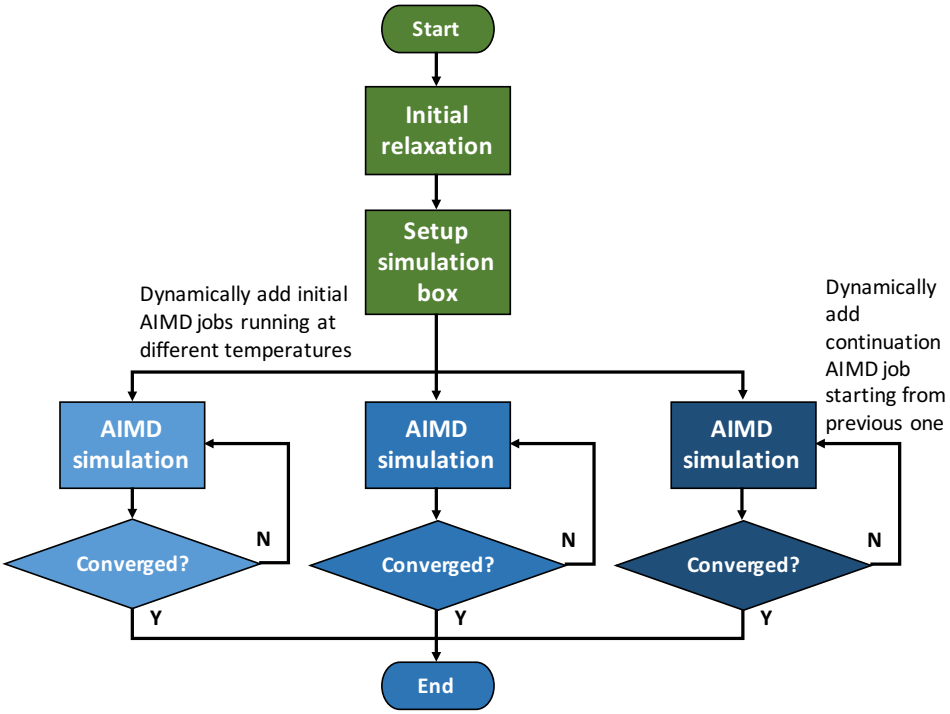

Figure 2.1: Schematic of the automated AIMD workflow implemented using the FireWorks workflow software. Processes in the green belong to initial relaxation job. Processes in blue belong to AIMD jobs running in parallel at different temperatures.[36]

except for an initial workflow and structure setup.

Another challenge is the considerable quantity of data (e.g., trajectories) generated in AIMD simulationsSecond compared to other first principles calculations. Though analyses can be performed directly from the raw outputs of the calculations, a more modern approach is to use state-of-the-art databases for data management. In this work, we use MongoDB, a NoSQL database to store the trajectories and analyses from AIMD simulations. Each MD snapshot, together with identifying information and the time step number, is stored as a single document within a collection. This storage scheme allows one to efficiently query for subsets of snapshots (e.g., every 10 or 100 time steps) for analysis. The results of all analyses (e.g., calculated diffusivities, conductivities, activation barriers, etc.) are stored in a separate collection for easy retrieval.

2.5 Limitations of AIMD

With the automated workflow, we are able to scale up the investigations using AIMD simulations. However, certain restrictions still apply due to the high computational costs. For instance, the system used in AIMD are rather small in size containing up to a few hundreds of atoms. The accessible simulation time scale is strictly limited to the level of sub-nanosecond. Calculations requiring a large number of particles or a longer simulation time therefore become inaccessible in AIMD. As an example, the estimation of thermodynamic factor Θ in Equation 2.7 is beyond the scope of AIMD. As a result, the self diffusivity D^* is plugged in Equation 2.6 by simply assuming $\Theta = 1$, which may lead to overestimated ionic conductivity.

Instead of switching to empirical potentials with limited accuracy and poor transferability, an alternative approach for constructing interatomic potentials is based on fitting to data from quantum mechanical calculations with flexible functional forms. These potentials can in principle reach exceptionally good numerical accuracy. Several methods have been proposed under this category.[38, 39] In this thesis, we will make our own effort to address the limitations associated with AIMD via this approach. More details are discussed in Chapter 6.

Chapter 3

Investigation of Argyrodite Li_6PS_5Cl as a Solid Electrolyte

Ionic conductivity and electrochemical stability are of technical importance for an electrolyte material whether it is liquid or solid. Meanwhile, phase stability is important for all material design problems. This chapter presents a comprehensive evaluations of argyrodite Li_6PS_5Cl on its phase stability, electrochemical stability and ionic conductivity. The sequence of properties is arranged in terms of computational costs and complexity with a modern high-throughput DFT calculation infrastructure.

3.1 Lithium Argyrodite

Argyrodite is an uncommon class of chalcogenide compounds. Kuhs *et al.* synthesized a series of argyrodite structures with common formula $A^{m+}_{12-n-x}B^{n+}X^{2-}_{6-x}Y^{-}_{x}$ (A: Cu, Ag, Cd, Hg; B: Ga, Si, Ge, Sn, P, As; X: S, Se, Te; Y: Cl, Br, I; $0 \leq x \leq 1$), and ionic conductivities were observed in certain Cu and Ag containing compounds.[40] Inspired by the similar ionic radii between Cu(I) ions (74 pm) and Li ions (73 pm), Deiseroth *et al.* synthesized Li containing argyrodites Li_6PS_5X

(X: Cl, Br, I), and confirmed the expected high mobility of Li ions.[41] In the cubic crystal structures with space group $F\bar{4}3m$, random occupation of atomic positions 48*h* and 24*g* by Li ions is the key role for facile Li diffusion.[41] Stadler *et al.* subsequently reported that Li_6PS_5Cl and Li_6PS_5Br have high ionic conductivity on the level of 0.1 mS/cm, low electronic conductivity and wide electrochemical window up to 5 V vs. Li/Li^+, while Li_6PS_5I shows relatively low ionic conductivity and poor electrochemical stability due to the ease oxidation of iodides.[42] Although the conductivity was later pushed higher by 1 order of magnitude, the performance of all-solid-state lithium batteries using Li_6PS_5Cl or Li_6PS_5Br as solid electrolyte is generally poor.[43, 44, 45, 46, 47, 48, 49]

In this work, we present a detailed investigation of Li argyrodite Li_6PS_5Cl as solid electrolyte with focus not just on the ionic conductivity, but also other technologically relevant properties such as phase and electrochemical stability. Like many other sulfide solid electrolytes, we find that the intrinsic electrochemical window of Li_6PS_5Cl is much narrower than the one claimed from experimental measurements. Moreover, we attribute the high ionic conductivity to Li excess in the structure induced by anion disordering and off-stoichiometric ratio of sulfur and chlorine. In a broader context, the emphasis of this work lies on the use of modern information technology (IT) and database infrastructure coupled with robust software packages to efficiently conduct and analyze DFT calculations.

3.2 Structure Enumeration

We obtained the initial crystal structure of Li_6PS_5Cl from the Inorganic Crystal Structure Database (ICSD)[50], a conventional cubic unit cell with formula $Li_{6.72}PS_5Cl$, i.e., excess of lithium. It also exhibits disorder, like many other solid electrolytes (e.g., LGPS $Li_{10}GeP_2S_{12}$). An ordered configuration with reasonably low energy is required for subsequent modelings. To obtain stoichiometric charge-balanced Li_6PS_5Cl, we adjusted the occupancy of Li 48*h* sites to

0.5, and enumerated all symmetrically distinct orderings of the primitive cell using pymatgen's wrapper to enumlib[51], an efficient Fortran code for enumeration of structure derivatives. A total of 48 unique structures were obtained and fully relaxed using DFT calculations. Although it has been shown both experimentally and theoretically that Li_6PS_5Cl may exhibit anti-site S/Cl disorder,[52] no attempt was made to model such disorder to keep the computational costs reasonable. The lowest energy structure is shown in Figure 3.1, and was used as the input to subsequent calculations and analyses. The relaxed lattice parameter a is 10.1 Å, 2.5% larger than experimental value.[41] This slight overestimation is due to the well-known tendency for the GGA functional to underbind.

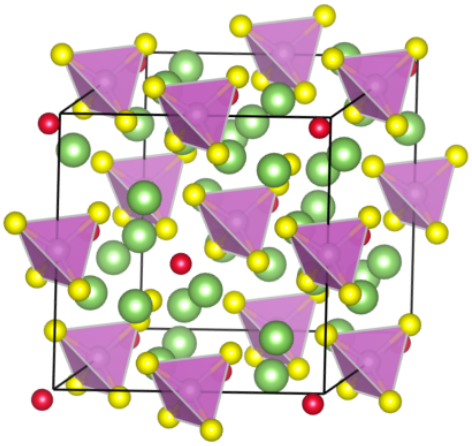

Figure 3.1: Lowest energy Li_6PS_5Cl structure determined from DFT calculations on all 48 symmetrically distinct orderings of the primitive experimental structure. Li in green, Cl in red, S in yellow and PS_4^{3-} polyhedra in purple.

3.3 Phase Stability

The necessity for phase stability is a common consideration in almost all materials design problems. The phase stability of a material can be estimated by constructing the relevant multi-component 0 K phase diagram. For the case of Li_6PS_5Cl, one would need to calculate the energies of all known phases in the Li-P-S-Cl chemical space, i.e., all Li, P, S, Cl, Li_xS_y, Li_xP_y, P_xS_y, P_xCl_y,

Li_xCl_y, S_xCl_y, $Li_xP_yS_z$, $P_xS_yCl_z$, $Li_xS_yCl_z$, $Li_xP_yCl_z$, $Li_xP_yS_zCl_w$ phases. The phase diagram can then be obtained via constructing the convex hull of the five-dimension $(\bar{E}, x_{Li}, x_P, x_S, x_{Cl})$ space, where $\bar{E}$ is the normalized energy per atom, and x_X is the atomic fraction of element X. Finally, the vertices lying on the convex hull[53] are projected into the Li-P-S-Cl compositional coordinate space to yield the phase diagram.[54] It should be noted that while finite temperature stability can be estimated by considering various (e.g., vibrational, configurational) contributions to the entropy for all relevant, such a computational and human resource-intensive effort is seldom carried as the DFT 0 K phase diagram typically yields a reasonable initial estimate of the relative stability of crystalline phases.

Even for a relatively "simple" quaternary compound such as Li_6PS_5Cl, a direct phase or electrochemical stability assessment is a significant computational undertaking due to the requirement to compute all phases in the Li-P-S-Cl system. Fortunately, one can leverage on existing large open databases such as the Materials Project (MP),[25] which contains the computed energies of all known ordered inorganic materials. Using pymatgen's high-level interface to the Materials Application Programming Interface,[55] one can query for the computed energies of all known ordered phases in the Li-P-S-Cl chemical space. To enhance the coverage of the phase space, we have also included derived phases obtained via O/S substitution from ordered Li-P-O tenary compounds. The phase diagram can then be constructed using pymatgen with all available entries (MP + derived + calculated entry for Li_6PS_5Cl). Care must be taken to ensure that the calculation parameters, e.g., choice of functional and pseudopotentials, are similar to those used in the MP to ensure compatibility. MP compatible VASP input files generation is also implemented in pymatgen.

Figure 3.2 shows the calculated pseudo-ternary Li_2S-P_2S_5-LiCl phase diagram. From the phase diagram, one may compute the energy above hull (E_{hull}) of Li_6PS_5Cl. The E_{hull} of a phase is defined as the normalized energy per atom for that phase above the linear combination of stable equilibrium phases at that composition in the phase diagram. A stable compound has an E_{hull} of

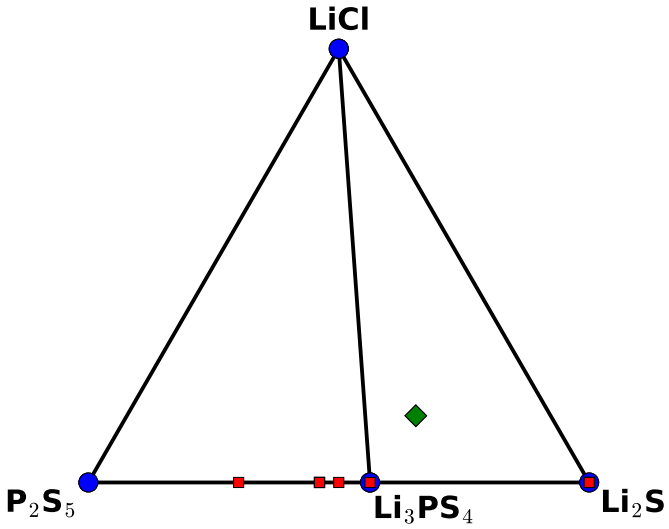

Figure 3.2: The pseudo-ternary Li_2S-P_2S_5-LiCl phase diagram. Blue circles with labeled compositions indicate stable phases. Li_6PS_5Cl is metastable (green diamond). Other unstable/metastable phases (including derived ones from O substitution by S in Li-P-O ternary compounds) are shown as red squares. The compositions of unstable/metastable phases along P_2S_5-Li_2S are $LiPS_3$, $Li_4P_2S_7$, $Li_7P_3S_{11}$, Li_3PS_4 and Li_2S.

0, and the higher the E_{hull}, the more unstable the compound is likely to be. The calculated E_{hull} of Li_6PS_5Cl is 21 meV/atom, indicating that it is metastable with respect to a linear combination of Li_3PS_4, Li_2S and LiCl at 0 K.

3.4 Electrochemical Stability

Another crucial property of a solid electrolyte is its electrochemical stability against the electrodes. This stability can be achieved either intrinsically, i.e., the solid electrolyte is completely inert against both the anode and cathode, or more realistically, via the formation of passivating layers. The phase equilibria at the electrolyte/electrode interface may be estimated using a grand potential phase diagram.[17, 56, 18] The solid electrolyte is subjected to a maximum range of electrochemical potential when the battery is in a fully charged state. Under such conditions, the Li-depleted cathode is effectively a Li sink at low Li chemical potential, while the anode is effectively a Li source with high Li chemical potential typically close to that of the bulk Li metal.

Assuming that the Li ion is the main mobile species, the electrolyte/anode and electrolyte/cathode interfaces can be approximated as open systems at $\mu_{\mathrm{Li}} = \mu^0_{\mathrm{Li}}$ and $\mu_{\mathrm{Li}} = \mu^0_{\mathrm{Li}} - e\Delta V$, respectively. Here, μ^0_{Li} is the chemical potential of the bulk Li metal, e is the elementary charge and ΔV refers to the voltage of the charged cathode versus Li/Li$^+$.[57] The relevant thermodynamic potential at 0 K is therefore the Li grand potential, given by the following expression:

$$\phi = E - \mu_{\mathrm{Li}} N_{\mathrm{Li}}, \tag{3.1}$$

where E is approximated as the computed DFT energy, N_{Li} is the number of Li atoms for a particular phase, and the PV term for solids is ignored.

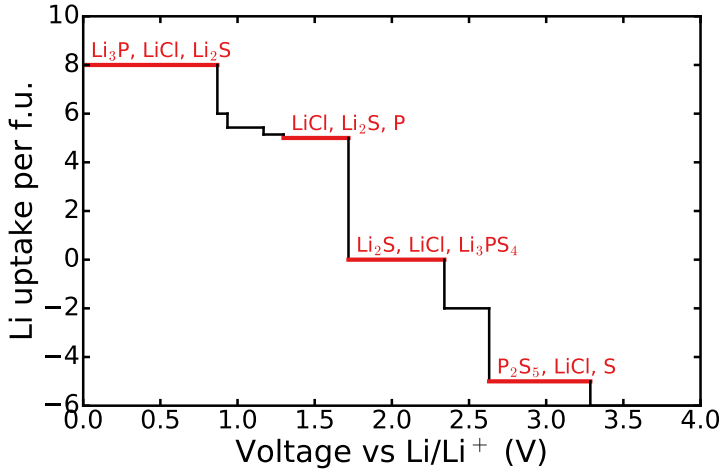

Figure 3.3: Plot of Li uptake per formula unit (f.u.) of Li_6PS_5Cl solid electrolyte (black solid) against voltage vs Li/Li$^+$. At low voltage (high Li chemical potential), Li_6PS_5Cl undergoes reduction and uptakes Li, whereas at high voltage (low Li chemical potential), Li_6PS_5Cl is oxidized and loses Li. Text indicates the predicted phase equilibria at corresponding regions of the profile. Only selected regions are annotated for brevity.

Using a similar phase diagram construction with ϕ instead of E , one can examine how the predicted phase equilibria at the solid electrolyte composition changes with Li chemical potential. Figure 3.3 shows the plot of the Li uptake per formula unit (f.u.) of Li_6PS_5Cl against voltage vs Li/Li$^+$. At low voltage (high Li chemical potential), the Li_6PS_5Cl solid electrolyte undergoes reduction and uptakes Li, while at high voltage (low Li chemical potential), electrolyte is oxidized

and loses Li. The plot clearly illustrates one of the major issues with sulfide solid electrolytes - the narrow range of intrinsic electrochemical stability. The Li_6PS_5Cl composition is stable against Li uptake and loss only within a narrow range of voltage ($1.7 \sim 2.3$ V). Nevertheless, we find that electronically insulating, ionically conducting phases (e.g., Li_2S, LiCl) are formed at both higher and lower voltages, which may potentially serve as good passivating interfacial phases that act as a barrier against further solid electrolyte decomposition.

3.5 Li Diffusivity and Conductivity

We performed AIMD simulations to investigate the Li diffusivity and conductivity in Li_6PS_5Cl. The simulations are under an NVT ensemble with the volume from structural optimization at 0 K adopted, and the simulation box only contains a single conventional unit cell of Li_6PS_5Cl. It is noted that MD simulations should ideally be performed on large supercells to avoid introducing artificial correlated diffusivity due to periodic boundary conditions. Due to the high cost of AIMD methods, only moderate cell sizes of at least 10 Å in each lattice direction are typically used. Therefore, for the case of Li_6PS_5Cl, the conventional cubic unit cell is a large enough system for AIMD simulations. The time step is set to 2 fs, a value typically sufficient for modeling Li diffusion.

In addition to the calculations of diffusivity and conductivity discussed in Chapter 2, more insights may be obtained by analyzing the trajectories from the AIMD simulations. A plot of the probability density function $P(\mathbf{r})$ can provide useful information on the low energy (high probability) sites in a superionic conductor, as well as the migration pathways between them.[58] P is often defined in a spatial 3D uniform grid, and can be computed by averaging the number of the Li ions at each grid point within a given time scale. P is normalized such that $\int_\Omega P \mathrm{d}\mathbf{r} = 1$ with Ω being the volume of the unit cell.

Many superionic conductors also exhibit correlated or cooperative ion motion, which can

be analyzed by computing the van Hove correlation function. The van Hove correlation can be split into the self-part G_s and the distinct-part G_d as follows:

$$G_s(r,t) = \frac{1}{4\pi r^2 N_d} \langle \sum_{i=1}^{N_d} \delta(r - |\mathbf{r}_i(t_0) - \mathbf{r}_i(t+t_0)|) \rangle_{t_0}, \tag{3.2}$$

$$G_d(r,t) = \frac{1}{4\pi r^2 \rho N_d} \langle \sum_{i \neq j}^{N_d} \delta(r - |\mathbf{r}_i(t_0) - \mathbf{r}_j(t+t_0)|) \rangle_{t_0}. \tag{3.3}$$

Here, $\delta(\cdot)$ is the one-dimensional Dirac delta function. The angular bracket stands for the ensemble average over the initial time t_0. $\mathbf{r}_i(t)$ denotes the position of the i^{th} particle at time t. N_d, r are the number of diffusing Li ions in the unit cell and radial distance, respectively. The presence of the average number density ρ serves as the "normalization factor" in G_d such that $G_d \longrightarrow 1$ when $r \gg 1$. For a given r and t, $G_s(r,t)$ describes how probable a particle diffuses away from its initial position by a distance of r after time t, whereas $G_d(r,t)$ describes the radial distribution of $N-1$ particles after time t with respect to the initial reference particle. In particular, $G_d(r,t)$ is reduced to the static pair distribution function when $t = 0$, which is often used to investigate the dynamics of structural changes.

Both the probability density and van Hove function analyses are already implemented in the open-source pymatgen-diffusion[59] add-on package.

Figure 3.4 shows the Arrhenius plot for Li_6PS_5Cl with diffusivities computed at four elevated temperatures (600 K to 1200 K with 200 K increments). We find that stoichiometric Li_6PS_5Cl is a poor ionic conductor ($\sigma_{300K} \approx 2 \times 10^{-3}$ mS/cm) with a high activation energy E_a of 524 meV.

The experimentally reported crystal structure has formula $Li_{6.72}PS_5Cl$, i.e., excess of Li. To more accurately model the reported phase, we performed similar analyses on a $Li_{6.25}PS_{5.25}Cl_{0.75}$ cell, which was constructed by introducing a single Li excess into the ordered stoichiometric Li_6PS_5Cl conventional cell with a Cl substituted by a S to ensure overall charge neutrality. The Li excess $Li_{6.25}PS_{5.25}Cl_{0.75}$ structure is only slightly less stable ($E_{\text{hull}} = 27$ meV/atom) than the

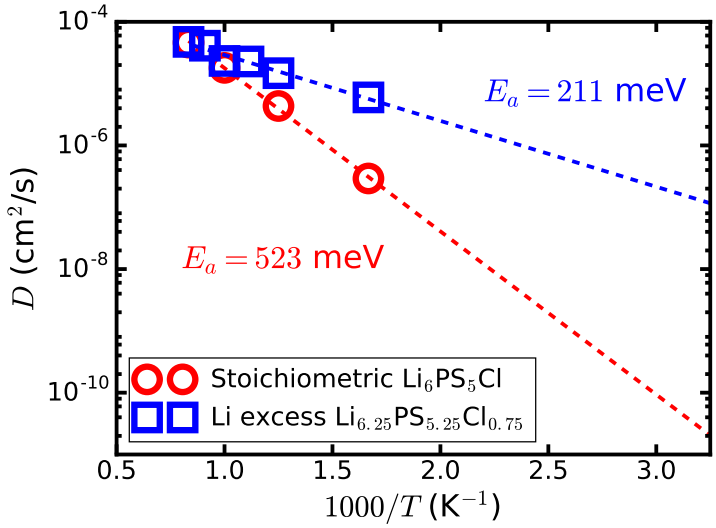

Figure 3.4: Arrhenius plots for stoichiometric Li_6PS_5Cl (red) and Li excess $Li_{6.25}PS_{5.25}Cl_{0.75}$ (blue). The standard deviations of E_a for stoichiometric Li_6PS_5Cl and Li excess $Li_{6.25}PS_{5.25}Cl_{0.75}$ are 13 and 18 meV, respectively.

stoichiometric Li_6PS_5Cl at 0 K. In terms of transport properties, Li excess $Li_{6.25}PS_{5.25}Cl_{0.75}$ exhibits a much higher room temperature ionic conductivity of 14 mS/cm and a much lower activation energy of 211 meV (Figure 3.4). The predicted room-temperature ionic conductivity is about one order of magnitude higher than previously measured total conductivities for this solid electrolyte. The predicted activation energy is in reasonable agreement with the experimentally reported values, though it should be noted that reported experimental values vary widely due to variations in the synthesis conditions and compositions.[60, 45]

Figure 3.5 shows the Li^+ probability density function (PDF) for Li excess $Li_{6.25}PS_{5.25}Cl_{0.75}$ at 800 K at various isovalues. We may observe from the PDF at higher isovalue (Figure 3.5a) that Li tends to move in a cage-like environment around each S 4*d* site, forming distorted Li_6S octahedrons. These results are similar to those reported in a previous study using bond valence methods.[60, 45] Because the cage-like trajectory is localized around a particular S site, this type of migration does not contribute to long-range ionic diffusion. Long-range diffusion happens due to migration between different cages, which can be observed at lower isovalues (Figure 3.5b).

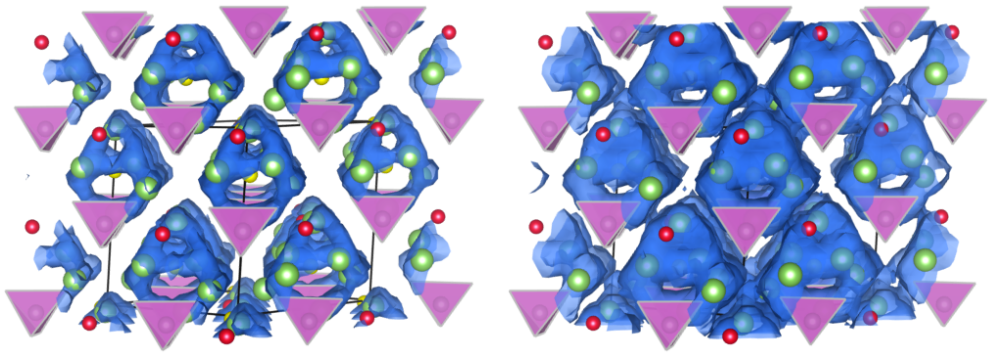

(a) $P = P_0$ (b) $P = P_0/8$

Figure 3.5: Li probability density distribution in Li excess $Li_{6.25}PS_{5.25}Cl_{0.75}$ obtained from AIMD simulations at 800 K. Isosurfaces (blue) of ionic probability densities are plotted at isovalues of P_0 and $P_0/8$, where $P_0 = 0.0025/a_0^3$ (a_0 is the Bohr radius).

The upper two plots in Figure 3.6 show the G_s for stoichiometric Li_6PS_5Cl and Li excess $Li_{6.25}PS_{5.25}Cl_{0.75}$, respectively. We observe that there is a persistent peak in G_s between 3.5 and 4.5 Å, which corresponds to the nearest Li-Li distances within the same cage, in both cases. However, this cage-related peak decays much more rapidly in the case of Li excess $Li_{6.25}PS_{5.25}Cl_{0.75}$ compared to stoichiometric Li_6PS_5Cl, and additional peaks at larger r values appear after ~ 30 ps. From the G_d plots (lower plots in Figure 3.6), we find that there is a high probability of a vacated Li site being rapidly occupied by another Li, though the time scale of these events is much shorter in the case of $Li_{6.25}PS_{5.25}Cl_{0.75}$, which is consistent with the faster diffusion observed in the Li excess material.

3.6 Discussion

In this work, we present a detailed outline of how a solid electrolyte can be comprehensively evaluated for multiple critical properties of interest using first principles calculations combined with modern IT infrastructure and software tools. The first principles calculations in themselves are not novel and have been used in many previous works, albeit on a more limited scale. However, the use of modern IT infrastructure and software tools dramatically transforms

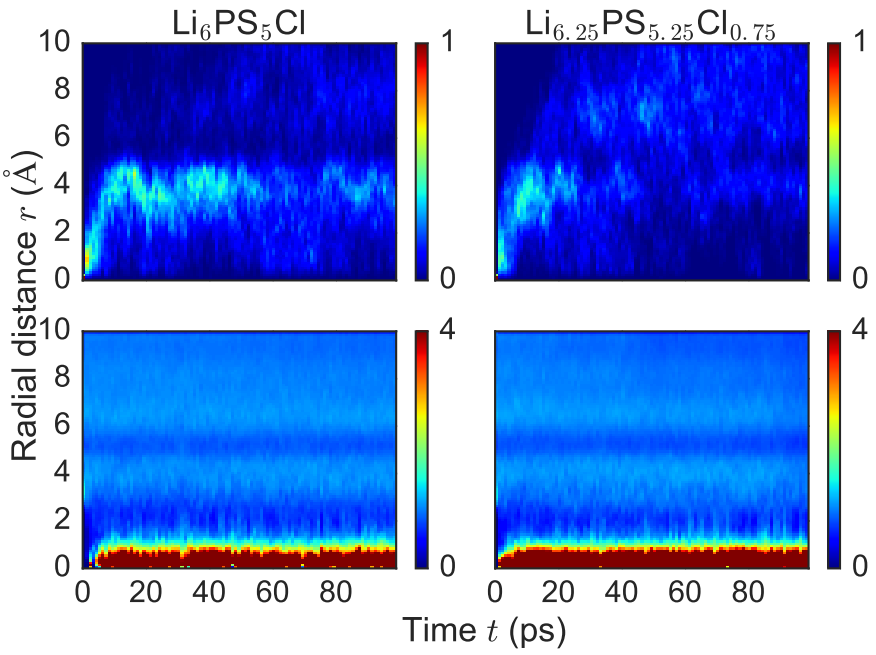

Figure 3.6: Plots of the self G_s (upper) and distinct G_d (lower) parts of the van Hove correlation function for stoichiometric Li_6PS_5Cl (left) and Li excess $Li_{6.25}PS_{5.25}Cl_{0.75}$ (right) obtained from AIMD simulations at 800 K.

the efficiency and scale in which such investigations can be carried out.

As a case study, we have demonstrated how all these techniques may be applied to argyrodite Li_6PS_5Cl. We find stoichiometric Li_6PS_5Cl to be a metastable, poor ionic conductor with limited intrinsic electrochemical stability, not unlike other thiophosphate superionics.[15, 61] Ionic conductivity is dramatically enhanced with the introduction of excess Li.

The most interesting feature about argyrodite Li_6PS_5Cl with and without Li excess is the existence of cage-like trapping of Li ions, a feature that can readily be observed in the van Hove correlation and probability density function analyses. Indeed, stoichiometric Li_6PS_5Cl exhibits low Li conductivity and high effective activation barriers in the AIMD simulations as motions within these cages do not contribute to long range diffusivity. The introduction of Li excess increases the occupancy of the interstitial sites and promotes inter-cage mobility, resulting in predicted conductivities and activation barriers that are much closer to experimentally observed

values.[60, 45] Similar alkali-excess-induced diffusion has been predicted in the cubic Na_3PS_4 superionic conductor.[62]

The predicted conductivity of 14 mS/cm for Li excess $Li_{6.25}PS_{5.25}Cl_{0.75}$ is about an order of magnitude higher than experimentally observed values of 1.1 mS/cm.[60, 45] There are three possible reasons for this discrepancy. First, there is uncertainty in the extrapolated conductivity ($12 \sim 18$ mS/cm) due to the statistical nature of AIMD simulations, which is magnified by the Arrhenius nature of the D vs $1/T$ relationship. Second, the experimentally reported values are for total conductivities, which are not directly comparable to the bulk conductivities computed in our simulations. This suggests that there may be scope for further enhancement of the conductivity via composition tuning or synthesis optimization to reduce grain boundary resistance.[63] Finally, the limited cell sizes used in AIMD simulations ($1 \times 1 \times 1$ conventional cell) may also lead to overestimated ionic conductivity due to artificial correlated diffusivity introduced by the periodic boundary conditions. However, a simulation cell size of ~ 10 Å in each direction usually yields reasonable diffusion estimates, as it is typically larger than correlation length scales.[17] Further convergence tests are not within the scope of this study due to the high computational cost involved in simulating a $2 \times 2 \times 2$ cell (416 atoms).

3.7 Conclusion

In this work, we present a detailed investigation of Li argyrodite Li_6PS_5Cl as solid electrolyte from efficiently using first principles calculations combined with modern IT infrastructure and software codes. The focus is on a holistic assessment of desired properties for a solid electrolyte, not just ionic conductivity but also phase and electrochemical stability. The electrochemical window of Li_6PS_5Cl is found to be much narrower than that claimed from experiments. In addition, we demonstrate the key structural feature for the high ionic conductivity is the Li excess in the structure induced by anion disordering and off-stoichiometric ratio of sulfur and

chlorine.

Chapter 3, in part, is a reprint of the material “Data-Driven First-Principles Methods for the Study and Design of Alkali Superionic Conductors” as it appears in Chemistry of Materials, Zhi Deng, Zhuoying Zhu, Iek-Heng Chu and Shyue Ping Ong, 2016, 29 (1). pp 281-288. The dissertation author was the primary investigator and author of this paper.

Chapter 4

Elastic Properties of Known Alkali Solid Electrolyte Candidates

The mechanical properties are a unique specification for solid electrolytes. In this chapter, we explore the mechanical properties of known Li/Na solid electrolyte candidates within the elastic region. First, we evaluate various functionals on reproducing elastic properties measured in experiments. We then use the chosen functional calculating the full elastic tensor and deriving elastic moduli for known solid electrolyte candidates. In the end, we discuss the implications of mechanical properties on the performance of all-solid-state batteries from three different perspectives.

4.1 Mechanical Properties of Solid Electrolytes

Unlike liquid electrolytes that flow freely like any fluids, solid electrolytes are rather firm and stable in shape. However, in the fabrication and operation of all-solid-state lithium batteries, a solid electrolyte capable of deformation would be preferred. A critical challenge in all-solid-state batteries is achieving and maintaining an intimate conformal contact with the electrodes during

operation. Typical commercial cathodes (e.g., $LiCoO_2$, $LiMn_2O_4$ and $LiFePO_4$) and anodes (e.g., graphitic and hard carbons) exhibit chemical strains of up to 10% during electrochemical cycling.[20] The challenge is even greater with cutting edge Si anodes, which exhibit volume changes in excess of 300%.[64] The solid electrolyte must therefore be able to deform without the formation of cracks or pores to maintain the electrode/electrolyte interface during these volume changes, which would require “soft" solid electrolytes that can acommodate large strains before failure. On the other hand, another potential application of solid electrolytes is in enabling Li metal anodes by suppressing Li dendrite formation,[21] for which a solid electrolyte with high shear modulus and hardness would be more suitable.[22]

Despite of great importance, there have been only a few works exploring the mechanical properties of solid electrolytes. Wolfenstine, Sakamoto and co-workers have reported on the Young’s modulus and fracture toughness of polycrystalline Al-stabilized cubic LLZO garnet and LLTO perovskite.[65, 66, 67] Jackman et al. also characterized Young’s modulus and fracture toughness of LATP.[68] In general, all these oxides exhibit relatively high Young’s moduli (100-200 GPa) and fracture toughnesses of ~ 1 MPa$/\sqrt{\text{m}}$. In the sulfide chemistry, Sakuda et al. measured the Young’s modulus of $Li_2S-P_2S_5$ glass electrolyte, which is tunable by its composition within the range of $18 \sim 25$ GPa.[69]

A common limitation of these experimental studies is that only the overall Young’s modulus, Poisson’s ratio and fracture toughness are measured. In rechargeable battery applications, the stresses/strains developed during operation are often anisotropic, requiring knowledge of the full elastic tensor. The full elastic tensor is also useful for understanding the development of internal stress fields during fabrication, which can often have critical impacts on final reliability performance of the device. Another potential issue is that the measured values (which are mainly for polycrystalline samples) are highly dependent on various factors such as moisture, porosity and microstructure, and the presence of secondary phases.[70, 65, 67, 68] Some chemistries are also inherently more challenging to handle experimentally, such as the sulfides which are typically

sensitive to moisture and air.

First principles calculations based on DFT can therefore be an invaluable complement to experiments in characterizing the intrinsic elastic properties (including the full elastic tensor) of solid electrolytes. An example is the work of Wang et al., who calculated the elastic properties of LGPS from first principles calculations.[71] However, data on most solid electrolyte candidates are still lacking.

In this work, we perform a comprehensive investigation of the elastic properties of 23 well-known ceramic alkali (18 Li-based and 5 Na-based) solid electrolyte candidates using first principles calculations. We will provide an assessment of the accuracy of three exchange-correlation functionals - the Perdew-Burke-Ernzerhof (PBE)[72], PBE revised for solids (PBEsol)[73] generalized gradient approximation functionals and the van der Waals (vdW) density functional with opt88 exchange (optB88-vdW)[74] - in predicting elastic properties. We report the calculated full elastic tensors and other derived elastic properties (e.g., bulk, shear and Young's modulus, Poisson's ratio, etc.) of these well-known candidates, and discuss observed trends with structure and chemistry. We will discuss the implications of the computed elastic properties for all-solid-state battery design. The data compiled in this work will also serve as a useful reference for future experiments as well as theoretical battery models.

4.2 Material Selection

We have selected 23 well-known Li-ion and Na-ion superionic conductors in a broad range of structures and chemistries for our study. It should be noted that a common strategy in optimizing the conductivity of many solid electrolytes is through the formation of solid solutions or the introduction of dopants. For the purposes of this work, we will limit our investigations to the elastic properties of end members or undoped structures, which should nonetheless be representative of entire classes of materials. A further desired outcome of this study is to ascertain

the effect of cation and anion chemistry on elastic properties. Where possible, we have included superionic conductors in both Li-ion and Na-ion chemistry and different anion chemistries if they are experimentally known.

The studied materials are as follows:

1. NAtrium SuperIonic CONductor (NASICON). The term NAtrium SuperIonic CONductor (NASICON) refers to a family of materials with general formula $AM(XO_4)_3$ (A: Li or Na, M: transition metal, X: P or Si), of which the framework structures consist of MO_6 octahedra and P/SiO_4 tetrahedra sharing common corners.[75, 76] Among the huge family, the solid solution $Na_{1+x}Zr_2P_{3-x}Si_xO_{12}$ and Al doped $LiTi_2(PO_4)_3$ (LATP) are two well-known alkali superionic conductors. We included end member $NaZr_2(PO_4)_3$ and undoped $LiT_2(PO_4)_3$ in this study. Both materials adopt a rhombohedral structure with space group $R\bar{3}c$.

2. Phosphate. Though γ-Li_3PO_4 is not a good superionic conductor, it is still of great fundamental interest for two reasons. Firstly, the LIthium SuperIonic CONductor (LISICON) is a solid solution of two γ-Li_3PO_4 type of materials (e.g., Li_4GeO_4).[7, 8] Also, the well-known glass electrolyte for thin-film Li-ion batteries, LIPON, is essentially N incorporated amorphous Li_3PO_4.[77, 78]

3. LLTO Perovskite. The lithium lanthanum titanium oxides (LLTO) have a general formula of $Li_{3x}La_{2/3-x}TiO_3$ ($0 \leq x \leq 0.16$). They adopt perovskite structure with A-site deficiency. LLTO are of interest as solid electrolyte because of their high bulk ionic conductivity (1 mS/cm) at room temperature).[11] Though the stoichiometry of LLTO is highly tunable, we only selected two compositions ($Li_{1/2}La_{1/2}TiO_3$ and $Li_{1/8}La_{5/8}TiO_3$) to represent this entire class of superionic conductors. For both compositions, we chose the ordered structures with lowest DFT energies found in the Materials Project[25] database.

4. Garnet. The ionic conduction in garnet-type structure $Li_5La_3M_2O_{12}$ (M: Ta or Nb,

$Ia\bar{3}d$ space group) was first reported by Weppner group.[79] Later, the same group reported $Li_7La_3Zr_2O_{12}$ (LLZO) with enhanced ionic conductivity to 0.4 mS/cm at room temperature.[14] The LLZO garnet is particularly attractive due to its excellent stability against lithium metal anode.[80] LLZO exists in two forms - a disordered cubic ($Ia\bar{3}d$ space group) form with higher conductivity[14] and an ordered tetragonal ($I4_1/acd$ space group) form with lower conductivity.[81] In this study, we have included the tetragonal ordered form of LLZO and the cubic $Li_5La_3M_2O_{12}$ (M: Ta or Nb).

5. Anti-perovskite. The anti-perovskites with general formula A_3OX (A: Li or Na, X: Cl or Br) are a recently discovered class of superionic conductors, with potential applications in both Li-ion and Na-ion chemistries.[82, 83, 84, 85, 86] We have included all ternary anti-perovskites formed by the Li and Na cations and the Br and Cl anions, i.e., Li_3OCl, Li_3OBr, Na_3OCl and Na_3OBr, in this study.

6. Thiophosphate. The thiophosphates include a variety of materials, typically characterized by the presence of ${PS_4}^{3-}$ tetrahedra (including condensed thiophosphates such as ${P_2S_7}^{3-}$), and P can partially be replaced by Ge, Si, Sn, etc.

   (a) Li_3PS_4. Isostructual with γ-Li_3PO_4, β-Li_3PS_4 is one of the end members of thio-LISICON solid solution $Li_{4-x}Ge_{1-x}P_xS_4$.[12] Nanoporous β-Li_3PS_4 shows significant improvement in ionic conductivity (~ 0.1 mS/cm) compared with its bulk form and γ-Li_3PS_4.[87] For calculating elastic properties of β-Li_3PS_4, between two types of symmetrically distinct partial occupied Li sites (Wycoff symbol: 4*b* and 4*c*), we assume that only 4*b* sites are fully occupied. Besides β-Li_3PS_4, we also have included the ordered γ-Li_3PS_4 structure (space group $Pmn2_1$) in this study for comparison.

   (b) $Li_{10}GeP_2S_{12}$. The recently reported $Li_{10}GeP_2S_{12}$ (LGPS) with space group $P4_2/nmc$ has one of the highest room temperature ionic conductivity (12 mS/cm) of known superionic conductors.[15, 17] The Sn and Si analogues have also been predicted

from first principles computations[35] to have similar ionic conductivity and were subsequently synthesized.[88, 89] For our calculations, we use the ordered structures of all the three materials from previous DFT studies.[17, 35] To preserve the tetragonal symmetry, we used the ordered structures with space group $P4_2/mc$.

(c) $Li_7P_3S_{11}$. Crystallized from $Li_2S-P_2S_5$ glass, $Li_7P_3S_{11}$ has a triclinic structure with space group $P\bar{1}$. The framework structure contains PS_4 tetrahedra and P_2S_7 ditetrahedra.[90] $Li_7P_3S_{11}$ has one of the highest ionic conductivity (17 mS/cm) at room temperature reported to-date.[61]

(d) Argyrodite Li_6PS_5X. The high Li-ion mobility in argyrodite Li_6PS_5X (X: Cl, Br, I) with space group $F\bar{4}3m$ was first reported by Deiseroth et al.[41] Argyrodites show ionic conductivity $\sim$ 1 mS/cm at room temperature in all-solid-state batteries. [60, 43, 44] In the argyrodite structures, Li-ions are randomly distributed in two types of sites. One of the sites (Wycoff symbol: 24*g*) is located at the center of a S_3 triangle with occupancy of 0.26, with two neighboring 48*h* sites with occupancy of 0.37. For this work, we assume that only the 24*g* sites are occupied.

(e) Na_3PS_4. The cubic Na_3PS_4 was reported by Hayashi et al. with ionic conductivity $\sim$ 0.2 mS/cm at room temperature.[91] Compared with the previously known tetragonal Na_3PS_4 with lower ionic conductivity, the cubic phase is believed to be a high temperature phase. The crystal structure was then confirmed to have $I\bar{4}3m$ space group.[92] Similar as the argyrodite structures, two types of Na sites are available in cubic Na_3PS_4. The 6*b* Na sites sit on either face-centered or edge-centered positions with occupancy of 0.8, while the 12*d* Na sites with occupancy of 0.1 are found between two 6*b* sites. To obtain an ordered structure, we assume that only the 6b sites are occupied.

4.3 Computational Details

Since the calculations of elastic tensors are sensitive to lattice constants, we first fully relaxed the structures until the residual force on each atom was less than 0.01 eV/Å. We used three different exchange-correlation functionals (PBE, PBEsol, optB88-vdW) to calculate the elastic constants. The PBEsol functional was selected since it has been shown to be more accurate than PBE in reproducing lattice constants.[73] The optB88-vdW functional was chosen to account for van de Waals (vdW) interactions in solid, which may be important in non-closed-packed structures.[93]

Recently, the Materials Project[25] has computed the elastic constants of inorganic compounds using an internally-developed code.[94] In this work, the elastic tensor, C_{ij} was calculated by performing six finite distortion of the lattice with the displacement of ± 0.015 Å and then fitted from the strain-stress relationship[95] implemented in VASP. We tested this approach against the data published in the Materials Project for LiH, Li_2O, Na_2O, CaS, MgO, Ga_2O_3, AlN, $BaZrO_3$, SrLiP, Sr_4Si_4Ru, and the results are in excellent agreement. The elastic moduli, such as bulk modulus B, shear modulus G and Young's modulus E were then derived based on the Voigt-Reuss-Hill (VRH) approximation.[96]

In the Voigt approximation, the elastic tensor, C_{ij} was predicted based on the uniform strain, giving the upper limit of the bulk modulus B and shear modulus G.

$$B_V = \frac{(c_{11}+c_{22}+c_{33})+2(c_{12}+c_{23}+c_{31})}{9}, \tag{4.1}$$

$$G_V = \frac{(c_{11}+c_{22}+c_{33})-(c_{12}+c_{23}+c_{31})+3(c_{44}+c_{55}+c_{66})}{15}. \tag{4.2}$$

In the Reuss approximation, the compliance tensor, s_{ij} was based on the uniform stress, leading

the lower boundary limit.

$$B_R = \frac{1}{(s_{11}+s_{22}+s_{33})+2(s_{12}+s_{23}+s_{31})}, \tag{4.3}$$

$$G_R = \frac{15}{4(s_{11}+s_{22}+s_{33})-4(s_{12}+s_{23}+s_{31})+3(s_{44}+s_{55}+s_{66})}, \tag{4.4}$$

where, the compliance tensor S_{ij} was described by

$$S_{ij} = C_{ij}^{-1}. \tag{4.5}$$

In Hill approximation, the arithmetic average of the Voigt and Reuss boundary limits was given by the following equations

$$B = \frac{B_V + B_R}{2}, \tag{4.6}$$

$$G = \frac{G_V + G_R}{2}. \tag{4.7}$$

In addition, Young's moduli E and Poisson's ration ν could be calculated by

$$E = \frac{9BG}{(3B+G)}, \tag{4.8}$$

$$\nu = \frac{(3B-2G)}{2(3B+G)}. \tag{4.9}$$

We also applied the Born elastic stability criterion [97, 98] to each of the systems studied to check if they were mechanically stable under zero pressure. This criterion in the harmonic approximation states that for a mechanically stable compound, the relevant elastic tensor must be positive definite, i.e., all its eigenvalues must be positive. The calculated elastic tensors for all systems studied in this work satisfy the Born criterion, regardless of the exchange-correlation functionals adopted.

4.4 Performance of Various Functionals

To assess the accuracy of various functionals for the computation of elastic properties, we calculated the elastic properties of Li_2S, Li_2O and Na_2S using the PBE, PBEsol and optB88-vdW functionals, presented in Table 4.1. These three materials are chosen based on the availability of experimental data on the full elastic tensors, as well as for their representativeness of the chemistries of interest in solid electrolytes, which includes both lithium and sodium oxide and sulfides.

Table 4.1: Calculated lattice parameter (a_0), elastic tensor (C_{ij}), bulk modulus (B), shear modulus (G), Young's modulus (E) and Poisson's ratio (ν) for Li_2S ($Fm\bar{3}m$), Li_2O ($Fm\bar{3}m$), and Na_2S ($Fm\bar{3}m$) with the PBE, PBEsol and optB88-vdW functionals.

Material	Method	a_0 (Å)	c_{11} (GPa)	c_{12} (GPa)	c_{44} (GPa)	B (GPa)	G (GPa)	E (GPa)	ν
	PBE	5.721	83.6	18.9	33.7	40.4	33.2	78.2	0.18
		(-0.56%)	(12.37%)	(9.57%)	(-5.64%)	(11.60%)	-	-	-
	PBEsol	5.663	87.2	21.2	35.4	43.2	34.4	81.6	0.19
		(0.46%)	(8.60%)	(-1.44%)	(-10.97%)	(5.47%)	-	-	-
Li_2S	optB88-vdW	5.693	88.0	20.9	36.1	43.2	35.1	82.6	0.18
		(-0.07%)	(7.76%)	(0%)	(-13.17%)	(5.47%)	-	-	-
	Exp.[99]	5.689	95.4	20.9	31.9	45.7	-	-	-
	PBE	4.656	198.6	18.8	58.6	78.7	69.6	161.3	0.16
		(-1.09%)	(1.68%)	(12.56%)	(0.17%)	(3.67%)	-	-	-
	PBEsol	4.596	208.7	21.5	61.1	83.9	72.5	169.0	0.16
		(0.22%)	(-3.32%)	(0%)	(-4.09%)	(-2.69%)	-	-	-
Li_2O	optB88-vdW	4.636	207.0	25.4	62.8	85.8	72.8	170.3	0.17
		(-0.65%)	(-2.48%)	(-18.14%)	(-6.98%)	(-5.02%)	-	-	-
	Exp.[100]	4.606	202	21.5	58.7	81.7	69.8	162.9	0.17
	PBE	6.571	54.3	15.5	17.1	28.4	18.0	44.5	0.24
		(-0.52%)	(32.96%)	(53.03%)	(18.57%)	(42.04%)	-	-	-
	PBEsol	6.510	57.0	17.0	17.6	30.3	18.5	46.2	0.25
		(0.41%)	(29.64%)	(48.48%)	(16.19%)	(38.16%)	-	-	-
Na_2S	optB88-vdW	6.521	55.8	17.2	18.5	30.0	18.8	46.7	0.24
		(0.24%)	(31.11%)	(47.88%)	(11.9%)	(38.78%)	-	-	-
	Exp.[101, 102]	6.537	81	33	21	49	-	-	-

[99] Lattice constants and elastic tensors measured at 10 K and 15 K, respectively

[100] Lattice constant, elastic tensor and moduli measured at 293K

[101, 102] Elastic tensors measured at 30 K

Values in parentheses denote percentage error from experimental values.

We observe that the standard PBE functional leads to lattice parameters that are somewhat larger than the experimental values ($\sim 0.5-1.1\%$), and the computed elastic constants and moduli are correspondingly smaller. This is consistent with the well-known tendency for PBE to underbind.[73]. The PBEsol and optB88-vdW functionals both correct this tendency, leading to lattice constants and elastic moduli that are much closer to the experimental values. We still observe a relatively large difference ($\sim 53\%$) between the computed and experimentally measured elastic constants and moduli for Na_2S. We believe that this is likely due to experimental error, given that Na_2S is highly moisture and air sensitive (and any degradation of the material can have a significant impact on measured elastic properties) and the experimental data was reported in 1977. Overall, we find all three functionals to reproduce the expected trend of $Na_2S < Li_2S \ll Li_2O$ in the elastic constants and moduli.

We also tested the three functionals against a small set of solid electrolytes whose bulk (B), shear (G) and Young's (E) modulus and Poisson's ratio (ν) have been previously determined (the full elastic tensor is not available experimentally). Table 4.2 summarizes the experimental and the calculated B, G, E and ν of three electrolyte materials using different exchange-correlation functionals. Similar to the previous test cases, the elastic moduli calculated with PBE are the smallest, while the optB88-vdW functional yields larger elastic moduli than PBEsol. For all three materials, the elastic moduli from all functionals are significantly higher than the values reported experimentally.[65, 67, 68] This difference can be attributed to a variety of factors. For example, the samples for characterization in experiments are all polycrystalline with finite grain size as well as porosity whereas they are modeled as infinite single crystals in plane-wave DFT. This can make a huge difference as in experiments, the elastic moduli of samples with different grain sizes or porosities vary.[65, 67, 68] The compositions used in our study are not exactly the same as experiments. In particular, the garnet $Li_7La_3Zr_2O_{12}$ studied in this work is the tetragonal form, while the reported experimental value is for the Al-stabilized cubic form. In fact, the elastic tensor moduli for the cubic $Li_5La_3Ta_2O_{12}$ and $Li_5La_3Nb_2O_{12}$ are much closer to the experimentally

reported values (see next section). Moreover, the DFT calculations are performed at 0 K, while experimental measurements are usually carried out at close to room temperature. Nevertheless, the trends in the elastic moduli are reproduced well with all three functionals.

Table 4.2: Calculated bulk modulus (B, in GPa), shear modulus (G, in GPa), Young's modulus (E, in GPa) and Poisson's ratio (ν) for t-$Li_7La_3Zr_2O_{12}$ LLZO garnet, $Li_{1/2}La_{1/2}TiO_3$ LLTO perovskite and $LiTi_2\,(PO_4)_3$ LTP NASICON with the PBE, PBEsol and optB88-vdW exchange-correlation functionals.

Material	Method	B	G	E	ν
t-$Li_7La_3Zr_2O_{12}$	PBE	116.7	63.7	161.7	0.27
	PBEsol	127.4	68.9	175.1	0.27
	optB88-vdW	150.1	75.0	192.9	0.29
	Exp.[65]	102.8	59.6	149.8	0.26
$Li_{1/2}La_{1/2}TiO_3$	PBE	170.8	102.2	255.6	0.25
	PBEsol	183.5	104.0	262.4	0.26
	optB88-vdW	196.4	121.2	301.6	0.24
	Exp.[67]	133.3	80.0	200	0.25
$LiTi_2\,(PO_4)_3$	PBE	92.5	55.6	139.0	0.25
	PBEsol	95.0	57.6	143.7	0.25
	optB88-vdW	115.1	59.6	152.5	0.28
	Exp.[68]	-	-	115	-

[65] Al stablized cubic garnet $Li_{6.24}La_3Zr_2Al_{0.24}O_{11.98}$ with porosity 0.03, elastic moduli measured at room temperature.

[67] $Li_{0.33}La_{0.57}TiO_3$ obtained from solid-state procedure.

[68] High-purity, fine-grained $Li_{1.3}Al_{0.3}Ti_{1.7}\,(PO_4)_3$.

Overall, our assessment is that the PBEsol functional is an excellent choice for the study of the elastic properties of solid electrolytes, given that its much higher accuracy in reproducing the elastic constants of our tests systems compared to standard PBE.

4.5 Elastic Properties of Solid Electrolyte Candidates

Table 4.3: Calculated full elastic tensor (C_{ij}), bulk modulus (B), shear modulus (G), Young's modulus (E), Poisson's ratio (ν) and Pugh's ratio (G/B) using the PBEsol functional.

Formula	Space group	C_{ij} (GPa)	Number of independent c_{ij}	B (GPa)	G (GPa)	E (GPa)	ν	G/B
		NASICON						
$LiTi_2(PO_4)_3$	$R\bar{3}c$	$\begin{bmatrix} 226.0 & 86.7 & 43.9 & 7.9 & 0.0 & 0.0 \\ 86.7 & 226.0 & 43.9 & -7.9 & 0.0 & 0.0 \\ 43.9 & 43.9 & 116.3 & 0.0 & 0.0 & 0.0 \\ 7.9 & -7.9 & 0.0 & 48.6 & 0.0 & 0.0 \\ 0.0 & 0.0 & 0.0 & 0.0 & 48.6 & 7.9 \\ 0.0 & 0.0 & 0.0 & 0.0 & 7.9 & 69.6 \end{bmatrix}$	6	95.0	57.6	143.7	0.25	0.61
$NaZr_2(PO_4)_3$	$R\bar{3}c$	$\begin{bmatrix} 175.2 & 77.7 & 51.9 & 9.4 & 0.0 & 0.0 \\ 77.7 & 175.2 & 51.9 & -9.4 & 0.0 & 0.0 \\ 51.9 & 51.9 & 102.4 & 0.0 & 0.0 & 0.0 \\ 9.4 & -9.4 & 0.0 & 53.2 & 0.0 & 0.0 \\ 0.0 & 0.0 & 0.0 & 0.0 & 53.2 & 9.4 \\ 0.0 & 0.0 & 0.0 & 0.0 & 9.4 & 48.7 \end{bmatrix}$	6	86.3	47.7	120.9	0.27	0.55
		Phosphate						
Li_3PO_4	$Pnma$	$\begin{bmatrix} 116.5 & 45.4 & 36.5 & 0.0 & 0.0 & 0.0 \\ 45.4 & 123.9 & 62.5 & 0.0 & 0.0 & 0.0 \\ 36.5 & 62.5 & 127.4 & 0.0 & 0.0 & 0.0 \\ 0.0 & 0.0 & 0.0 & 38.9 & 0.0 & 0.0 \\ 0.0 & 0.0 & 0.0 & 0.0 & 41.1 & 0.0 \\ 0.0 & 0.0 & 0.0 & 0.0 & 0.0 & 53.9 \end{bmatrix}$	9	72.5	40.9	103.4	0.26	0.56
		Perovskite						
$Li_{1/8}La_{5/8}TiO_3$	$Pmm2$	$\begin{bmatrix} 309.6 & 105.3 & 102.0 & 0.0 & 0.0 & 0.0 \\ 105.3 & 335.0 & 130.3 & 0.0 & 0.0 & 0.0 \\ 102.0 & 130.3 & 295.3 & 0.0 & 0.0 & 0.0 \\ 0.0 & 0.0 & 0.0 & 73.1 & 0.0 & 0.0 \\ 0.0 & 0.0 & 0.0 & 0.0 & 89.8 & 0.0 \\ 0.0 & 0.0 & 0.0 & 0.0 & 0.0 & 96.4 \end{bmatrix}$	9	179.0	91.2	233.9	0.28	0.51
$Li_{1/2}La_{1/2}TiO_3$	$P2/c$	$\begin{bmatrix} 354.2 & 112.8 & 88.4 & 0.0 & -0.0 & 0.0 \\ 112.8 & 360.4 & 92.1 & 0.0 & -0.1 & 0.0 \\ 88.4 & 92.1 & 351.4 & 0.0 & -0.1 & 0.0 \\ 0.0 & 0.0 & 0.0 & 97.0 & 0.0 & -1.9 \\ -0.0 & -0.1 & -0.1 & 0.0 & 98.2 & 0.0 \\ 0.0 & 0.0 & 0.0 & -1.9 & 0.0 & 77.4 \end{bmatrix}$	13	183.5	104.0	262.5	0.26	0.57
		Garnet						
$Li_5La_3Nb_2O_{12}$	$Ia\bar{3}d$	$\begin{bmatrix} 176.7 & 78.6 & 78.6 & 0.0 & 0.0 & 0.0 \\ 78.6 & 176.7 & 78.6 & 0.0 & 0.0 & 0.0 \\ 78.6 & 78.6 & 176.7 & 0.0 & 0.0 & 0.0 \\ 0.0 & 0.0 & 0.0 & 58.9 & 0.0 & 0.0 \\ 0.0 & 0.0 & 0.0 & 0.0 & 58.9 & 0.0 \\ 0.0 & 0.0 & 0.0 & 0.0 & 0.0 & 58.9 \end{bmatrix}$	3	111.3	54.8	141.1	0.29	0.49

Continued on next page

Table 4.3 continued.

Continued from previous page

Formula	Space group	C_{ij} (GPa)	Number of independent c_{ij}	B (GPa)	G (GPa)	E (GPa)	ν	G/B
$Li_5La_3Ta_2O_{12}$	$Ia\bar{3}d$	$\begin{bmatrix} 179.6 & 78.1 & 78.1 & 0.0 & 0.0 & 0.0 \\ 78.1 & 179.6 & 78.1 & 0.0 & 0.0 & 0.0 \\ 78.1 & 78.1 & 179.6 & 0.0 & 0.0 & 0.0 \\ 0.0 & 0.0 & 0.0 & 59.9 & 0.0 & 0.0 \\ 0.0 & 0.0 & 0.0 & 0.0 & 59.9 & 0.0 \\ 0.0 & 0.0 & 0.0 & 0.0 & 0.0 & 59.9 \end{bmatrix}$	3	112.0	56.1	144.2	0.29	0.50
$Li_7La_3Zr_2O_{12}$	$I4_1/acd$	$\begin{bmatrix} 196.9 & 92.7 & 86.2 & 0.0 & 0.0 & 0.0 \\ 92.7 & 196.9 & 86.2 & 0.0 & 0.0 & 0.0 \\ 86.2 & 86.2 & 224.2 & 0.0 & 0.0 & 0.0 \\ 0.0 & 0.0 & 0.0 & 80.1 & 0.0 & 0.0 \\ 0.0 & 0.0 & 0.0 & 0.0 & 80.1 & 0.0 \\ 0.0 & 0.0 & 0.0 & 0.0 & 0.0 & 71.0 \end{bmatrix}$	6	127.4	68.9	175.1	0.27	0.54
		Anti-Perovskite						
Li_3OCl	$Pm\bar{3}m$	$\begin{bmatrix} 102.9 & 32.1 & 32.1 & 0.0 & 0.0 & 0.0 \\ 32.1 & 102.9 & 32.1 & 0.0 & 0.0 & 0.0 \\ 32.1 & 32.1 & 102.9 & 0.0 & 0.0 & 0.0 \\ 0.0 & 0.0 & 0.0 & 46.1 & 0.0 & 0.0 \\ 0.0 & 0.0 & 0.0 & 0.0 & 46.1 & 0.0 \\ 0.0 & 0.0 & 0.0 & 0.0 & 0.0 & 46.1 \end{bmatrix}$	3	55.7	41.5	99.7	0.20	0.74
Li_3OBr	$Pm\bar{3}m$	$\begin{bmatrix} 91.0 & 33.0 & 33.0 & 0.0 & 0.0 & 0.0 \\ 33.0 & 91.0 & 33.0 & 0.0 & 0.0 & 0.0 \\ 33.0 & 33.0 & 91.0 & 0.0 & 0.0 & 0.0 \\ 0.0 & 0.0 & 0.0 & 46.6 & 0.0 & 0.0 \\ 0.0 & 0.0 & 0.0 & 0.0 & 46.6 & 0.0 \\ 0.0 & 0.0 & 0.0 & 0.0 & 0.0 & 46.6 \end{bmatrix}$	3	52.3	38.5	92.8	0.20	0.74
Na_3OBr	$Pm\bar{3}m$	$\begin{bmatrix} 70.0 & 16.0 & 16.0 & 0.0 & 0.0 & 0.0 \\ 16.0 & 70.0 & 16.0 & 0.0 & 0.0 & 0.0 \\ 16.0 & 16.0 & 70.0 & 0.0 & 0.0 & 0.0 \\ 0.0 & 0.0 & 0.0 & 21.5 & 0.0 & 0.0 \\ 0.0 & 0.0 & 0.0 & 0.0 & 21.5 & 0.0 \\ 0.0 & 0.0 & 0.0 & 0.0 & 0.0 & 21.5 \end{bmatrix}$	3	34.0	23.6	57.4	0.22	0.69
Na_3OCl	$Pm\bar{3}m$	$\begin{bmatrix} 78.1 & 15.5 & 15.5 & 0.0 & 0.0 & 0.0 \\ 15.5 & 78.1 & 15.5 & 0.0 & 0.0 & 0.0 \\ 15.5 & 15.5 & 78.1 & 0.0 & 0.0 & 0.0 \\ 0.0 & 0.0 & 0.0 & 20.9 & 0.0 & 0.0 \\ 0.0 & 0.0 & 0.0 & 0.0 & 20.9 & 0.0 \\ 0.0 & 0.0 & 0.0 & 0.0 & 0.0 & 20.9 \end{bmatrix}$	3	36.4	24.6	60.2	0.22	0.68
		Thiophosphate: Li_3PS_4						
Li_3PS_4	$Pnma$	$\begin{bmatrix} 32.1 & 10.9 & 19.7 & 0.0 & 0.0 & 0.0 \\ 10.9 & 38.1 & 17.4 & 0.0 & 0.0 & 0.0 \\ 19.7 & 17.4 & 51.8 & 0.0 & 0.0 & 0.0 \\ 0.0 & 0.0 & 0.0 & 10.5 & 0.0 & 0.0 \\ 0.0 & 0.0 & 0.0 & 0.0 & 9.5 & 0.0 \\ 0.0 & 0.0 & 0.0 & 0.0 & 0.0 & 13.7 \end{bmatrix}$	9	23.3	11.4	29.5	0.29	0.49

Continued on next page

Table 4.3 continued.

Continued from previous page

Formula	Space group	C_{ij} (GPa)	Number of independent c_{ij}	B (GPa)	G (GPa)	E (GPa)	ν	G/B
Li_3PS_4	$Pmn2_1$	$\begin{bmatrix} 53.8 & 23.3 & 23.8 & 0.0 & 0.0 & 0.0 \\ 23.3 & 49.2 & 27.3 & 0.0 & 0.0 & 0.0 \\ 23.8 & 27.3 & 44.9 & 0.0 & 0.0 & 0.0 \\ 0.0 & 0.0 & 0.0 & 12.3 & 0.0 & 0.0 \\ 0.0 & 0.0 & 0.0 & 0.0 & 15.0 & 0.0 \\ 0.0 & 0.0 & 0.0 & 0.0 & 0.0 & 11.7 \end{bmatrix}$	9	32.9	12.6	33.4	0.33	0.38
Thiophosphate: $Li_{10}MP_2S_{12}$								
$Li_{10}GeP_2S_{12}$	$P4_2mc$	$\begin{bmatrix} 44.9 & 27.7 & 12.6 & 0.0 & 0.0 & 0.0 \\ 27.7 & 44.9 & 12.6 & 0.0 & 0.0 & 0.0 \\ 12.6 & 12.6 & 51.2 & 0.0 & 0.0 & 0.0 \\ 0.0 & 0.0 & 0.0 & 3.5 & 0.0 & 0.0 \\ 0.0 & 0.0 & 0.0 & 0.0 & 3.5 & 0.0 \\ 0.0 & 0.0 & 0.0 & 0.0 & 0.0 & 12.4 \end{bmatrix}$	6	27.3	7.9	21.7	0.37	0.29
$Li_{10}SiP_2S_{12}$	$P4_2mc$	$\begin{bmatrix} 45.7 & 28.2 & 13.2 & 0.0 & 0.0 & 0.0 \\ 28.2 & 45.7 & 13.2 & 0.0 & 0.0 & 0.0 \\ 13.2 & 13.2 & 50.4 & 0.0 & 0.0 & 0.0 \\ 0.0 & 0.0 & 0.0 & 5.2 & 0.0 & 0.0 \\ 0.0 & 0.0 & 0.0 & 0.0 & 5.2 & 0.0 \\ 0.0 & 0.0 & 0.0 & 0.0 & 0.0 & 12.2 \end{bmatrix}$	6	27.8	9.2	24.8	0.35	0.33
$Li_{10}SnP_2S_{12}$	$P4_2mc$	$\begin{bmatrix} 39.0 & 26.3 & 8.5 & 0.0 & 0.0 & 0.0 \\ 26.3 & 39.0 & 8.5 & 0.0 & 0.0 & 0.0 \\ 8.5 & 8.5 & 47.7 & 0.0 & 0.0 & 0.0 \\ 0.0 & 0.0 & 0.0 & 9.4 & 0.0 & 0.0 \\ 0.0 & 0.0 & 0.0 & 0.0 & 9.4 & 0.0 \\ 0.0 & 0.0 & 0.0 & 0.0 & 0.0 & 14.5 \end{bmatrix}$	6	23.5	11.2	29.1	0.29	0.48
Thiophosphate: $Li_7P_3S_{11}$								
$Li_7P_3S_{11}$	$P\bar{1}$	$\begin{bmatrix} 31.8 & 19.2 & 18.5 & 1.1 & -2.9 & -0.4 \\ 19.2 & 26.0 & 20.7 & -1.5 & 2.8 & 1.4 \\ 18.5 & 20.7 & 49.3 & -1.7 & -1.8 & 1.6 \\ 1.1 & -1.5 & -1.7 & 10.7 & 3.2 & 1.5 \\ -2.9 & 2.8 & -1.8 & 3.2 & 13.6 & -2.5 \\ -0.4 & 1.4 & 1.6 & 1.5 & -2.5 & 9.1 \end{bmatrix}$	21	23.9	8.1	21.9	0.35	0.34
Thiophosphate: Argyrodite								
Li_6PS_5Cl	$F\bar{4}3m$	$\begin{bmatrix} 39.9 & 23.1 & 23.1 & 0.0 & 0.0 & 0.0 \\ 23.1 & 39.9 & 23.1 & 0.0 & 0.0 & 0.0 \\ 23.1 & 23.1 & 39.9 & 0.0 & 0.0 & 0.0 \\ 0.0 & 0.0 & 0.0 & 7.8 & 0.0 & 0.0 \\ 0.0 & 0.0 & 0.0 & 0.0 & 7.8 & 0.0 \\ 0.0 & 0.0 & 0.0 & 0.0 & 0.0 & 7.8 \end{bmatrix}$	3	28.7	8.1	22.1	0.37	0.28
Li_6PS_5Br	$F\bar{4}3m$	$\begin{bmatrix} 40.9 & 23.0 & 23.0 & 0.0 & 0.0 & 0.0 \\ 23.0 & 40.9 & 23.0 & 0.0 & 0.0 & 0.0 \\ 23.0 & 23.0 & 40.9 & 0.0 & 0.0 & 0.0 \\ 0.0 & 0.0 & 0.0 & 9.6 & 0.0 & 0.0 \\ 0.0 & 0.0 & 0.0 & 0.0 & 9.6 & 0.0 \\ 0.0 & 0.0 & 0.0 & 0.0 & 0.0 & 9.6 \end{bmatrix}$	3	29.0	9.3	25.3	0.35	0.32

Continued on next page

Table 4.3 continued.

Continued from previous page

Formula	Space group	C_{ij} (GPa)	Number of independent c_{ij}	B (GPa)	G (GPa)	E (GPa)	ν	G/B
Li_6PS_5I	$F\bar{4}3m$	$\begin{bmatrix} 43.6 & 23.0 & 23.0 & 0.0 & 0.0 & 0.0 \\ 23.0 & 43.6 & 23.0 & 0.0 & 0.0 & 0.0 \\ 23.0 & 23.0 & 43.6 & 0.0 & 0.0 & 0.0 \\ 0.0 & 0.0 & 0.0 & 11.9 & 0.0 & 0.0 \\ 0.0 & 0.0 & 0.0 & 0.0 & 11.9 & 0.0 \\ 0.0 & 0.0 & 0.0 & 0.0 & 0.0 & 11.9 \end{bmatrix}$	3	29.9	11.3	30.0	0.33	0.38
		Thiophosphate: Na_3PS_4						
Na_3PS_4	$I\bar{4}3m$	$\begin{bmatrix} 42.2 & 11.1 & 11.1 & 0.0 & 0.0 & 0.0 \\ 11.1 & 42.2 & 11.1 & 0.0 & 0.0 & 0.0 \\ 11.1 & 11.1 & 42.2 & 0.0 & 0.0 & 0.0 \\ 0.0 & 0.0 & 0.0 & 11.7 & 0.0 & 0.0 \\ 0.0 & 0.0 & 0.0 & 0.0 & 11.7 & 0.0 \\ 0.0 & 0.0 & 0.0 & 0.0 & 0.0 & 11.7 \end{bmatrix}$	3	21.5	13.1	32.6	0.25	0.61
Na_3PS_4	$P\bar{4}2_1c$	$\begin{bmatrix} 49.8 & 11.4 & 15.7 & 0.0 & 0.0 & 0.0 \\ 11.4 & 49.8 & 15.7 & 0.0 & 0.0 & 0.0 \\ 15.7 & 15.7 & 42.9 & 0.0 & 0.0 & 0.0 \\ 0.0 & 0.0 & 0.0 & 11.1 & 0.0 & 0.0 \\ 0.0 & 0.0 & 0.0 & 0.0 & 11.1 & 0.0 \\ 0.0 & 0.0 & 0.0 & 0.0 & 0.0 & 11.7 \end{bmatrix}$	6	25.3	13.1	33.6	0.28	0.52

In Table 4.3, we tabulate the elastic tensor, bulk (B), shear (G) and Young's (E) modulus and Poisson's ratio (ν) of each solid electrolyte candidate studied in this work calculated using the PBEsol functional. We have also provided the PBE and optB88-vdW results in the Appendix A. To facilitate interpretation of the results, we have plotted the shear modulus (G) against the bulk modulus (B) for all investigated candidates in Figure 4.1. We may make the following observations from Table 4.3 and Figure 4.1:

1. Somewhat unsurprisingly, we find that the sulfide superionic conductors are predicted to have very small elastic moduli ($E < 50$ GPa, $B < 40$ GPa, $G < 20$ GPa) compared to the oxides.

2. The structure framework and anion chemistry is a primary determinant of the elastic properties of solid electrolyte candidates. All similar chemistries tend to have similar elastic moduli. The relative elastic moduli follow the order of thiophosphate $<$ anti-perovskite $<$ phosphate $<$ NASICON $<$ garnet $<$ perovskite.

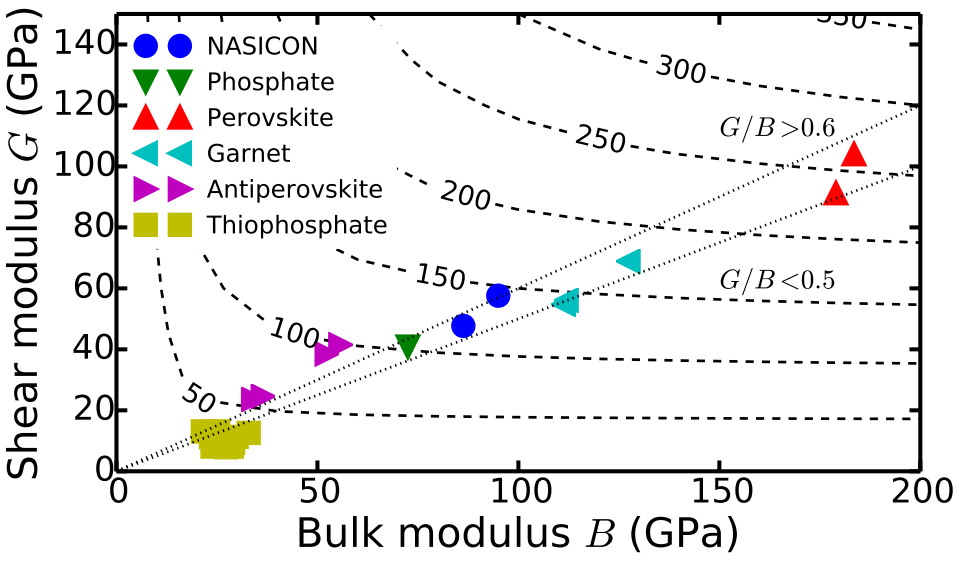

Figure 4.1: Plot of the shear modulus (G) vs bulk modulus (B) for all investigated solid electrolyte candidates calculated using the PBEsol functional. Dashed lines are the iso-Young's modulus lines in GPa. Two dotted lines correspond to $G/B = 0.5$ and $G/B = 0.6$.

3. Among the oxides, the phosphate (PO_4) framework structures such as the NASICON and Li_3PO_4 have significantly lower elastic moduli than the garnet and perovskites.

4. Within the same structural chemistries, we find that the Na version superionic conductor have smaller elastic moduli than the Li analogue. For example, the calculated Young's modulus of the Na_3OX (X: Cl, Br) anti-perovskites are approximately 50 GPa, while that of the Li_3OX are closer to 100 GPa. A similar trend is also observed for the NASICON-based structures $LiTi_2(PO_4)_3$ and $NaZr_2(PO_4)_3$. For the A_3PS_4 compounds, both polymorphs of Na_3PS_4 is predicted to have both a much smaller bulk modulus as well as a smaller shear modulus than the two polymorphs of Li_3PS_4. The overall Young's modulus of Na_3PS_4 is actually predicted to be similar to that of Li_3PS_4. It should be mentioned that the default step size of lattice displacement when calculating the elastic tensors produced negative c_{44} for cubic-Na_3PS_4, which can be attributed to "collapse" of the metastable cubic-Na_3PS_4. In this case, a very small strain ($\delta = 0.05\%$) was applied to evaluate its elastic tensor.

5. Among the garnet structures, we find that the tetragonal $Li_7La_3Zr_2O_{12}$ is predicted to have a much larger bulk, shear and Young's moduli than the cubic $Li_5La_3M_2O_{12}$ (M: Nb or Ta). As noted in the previous section, the calculated elastic moduli of the cubic Li5 are in fact extremely similar to the measured experimental values of cubic $Li_7La_3Zr_2O_{12}$. We hypothesize that the Li disorder and resulting structural symmetry has a substantial effect on the elastic moduli in this system. The transition metal cation (Nb/Ta) seem to have a relatively small effect on the elastic moduli, except in so far where aliovalent substitutions modifies Li concentration and the structural symmetry.[103] In essence, we speculate that though the garnet framework comprises of La-O dodecahedra and Zr-O octahedra, strong Li-O interactions act as a "glue" that nonetheless have significant influence on elastic properties.

6. The Pugh's ratio, G/B[104] is commonly used to evaluate the brittleness of materials from elastic moduli. A larger G/B indicates that the material is more brittle. This criterion has been applied in ceramic materials in Li-ion batteries.[105, 106, 71] From our calculations, thiophosphates have the most ductile with lowest G/B ratio (< 0.5) among all the chemistries with a few exceptions (e.g., c-Na_3PS_4). For most oxides, the G/B ratio lies between 0.5 and 0.6, while the high G/B ratio in anti-perovskites (~ 0.7) is an indication of their intrinsic brittle nature.

4.6 Implications on All-Solid-State Batteries

This work is an attempt at addressing a critical knowledge gap - the lack of comprehensive data on the elastic properties of solid electrolyte candidates. The mechanical properties of these candidates can have a profound impact on the design and performance of all-solid-state batteries in many different aspects, including fabrication, battery operation and potentially enabling the use of a Li metal anode.

4.6.1 Fabrication

One of the key requirements to fabricating a high-performing all-solid-state battery is achieving intimate conformal (pore and crack-free) contact of the solid electrolyte with the electrodes. Generally, such contact is harder to achieve in relatively “stiff" materials such as the LLTO and LLZO oxides, often requiring high-temperature sintering and densification techniques to achieve reasonable performance. Conversely, cold-press sintering is often sufficient to achieve a reasonably dense electrolyte with softer superionic conductors such the thiophosphates.[69] The residual stresses introduced by high-temperature fabrication routes, which depend on the magnitude as well as the anisotropy of the moduli, may make them prone to cracking and fracture. The full elastic modulus tensor, along with 3-D orientation maps of polycrystals from simulation of electron backscattering measurements, can be used to access the development of non-uniform local residual stresses as a result of anisotropic elastic properties.

In cases where there are limited thermal budgets (e.g., certain components of all-solid-state batteries may be prone to evaporation or where inter-diffusion between different materials or components needs to be limited), thermal shocking resistance, which depends critically on the average modulus, becomes important. Also, as all-solid-state batteries have multiple layers of materials, any high-temperature processing will naturally result thermal stresses that depend on both the differential thermal expansion coefficients and moduli of all components, and high thermal stresses will likely result in delamination.

4.6.2 Battery Operation

During the charge and discharge of an alkali-ion battery, the electrode materials typically undergo significant lattice parameter changes that are usually anisotropic. For instance, the commercial $LiCoO_2$ cathode material undergoes large c lattice parameter changes of up to 2.6%, with the a and b lattice parameters experiencing much smaller changes of -0.39%.[107] Similarly,

the $LiFePO_4$ olivine experience significant changes in the *a* lattice parameter upon delithiation, sometimes with fracture occurring in the cathode material itself.[108] For good electrochemical performance, the solid electrolyte must be able to deform and maintain good conformal contact with the electrode throughout these lattice parameter changes. In this respect, “softer" candidates would likely be able to accommodate these strains better while maintaining good electrode contact.

On the other hand, commercial batteries are often subject to mechanical abuse. A “harder" oxide solid electrolyte would be better able to withstand mechanical shocks that can potentially perforate the battery and cause shorting.

4.6.3 Enabling Li Metal Anode

One of the holy grails in rechargeable Li-ion battery technology is enabling the use of Li metal instead of graphitic carbon as the anode. Such Li metal anode has a much higher theoretical specific capacity of 3860 mAh/g compared to 372 mAh/g for graphite anode.[21]

The key challenge in the use of Li metal anodes is the formation of dendrites during deposition. A model proposed by Monroe et al. demonstrated that a blocking layer with shear modulus twice that of lithium (4.2 GPa) can effectively suppress the growth of lithium dendrites.[22] Based on this simple model, all materials studied in this work would be able to mechanically block the growth of lithium dendrites. However, Nagao et al. observed that $Li_2S-P_2S_5$ glass electrolyte cracks at high current density (> 1 mA/cm^2), and lithium dendrites grow along the crack. This is attributed to the failure of solid electrolyte in accommodating the vast volume change due to the deposition of lithium.[109] Similar phenomenon have also observed in LLZO.[110] We may surmise that the stiffness of the solid electrolyte is less of a practical issue than achieving a dense, crack-free material.

A recurring theme in the above analyses is that from the purely mechanical perspective, “softer" solid electrolytes would have the advantages of being able to achieve and maintain

intimate contact with the electrodes more easily. Achieving (and maintaining) good contact in "stiff" oxide solid electrolytes is largely an unresolved challenge today. A potential compromise is to use hybrid solid electrolytes, where electrolytes of different elastic moduli are combined into a composite electrolyte (assuming chemical compatibility). Yet another alternative is to incorporate a wetting liquid electrolyte with a "hard" oxide electrolyte, with possibly a reduction in the safety benefits.

4.7 Conclusion

To conclude, we have investigated the elastic properties, including the full elastic tensor, bulk, shear and Young's moduli, and Poisson's ratio of a broad spectrum of alkali superionic conductors using first principles calculations. We find that the computed elastic constants are in good agreement with experimental data wherever available and chemical bonding nature. In general, we find that Na superionic conductors are somewhat softer than the isostructures with Li, and the anion and structure type have a significant influence on the elastic properties. The data provided in this work would also provide a useful benchmark for future experimental investigations and computational modeling of solid electrolytes for all-solid-state battery applications.

Chapter 4, in full, is a reprint of the material "Elastic Properties of Alkali Superionic Conductor Electrolytes from First Principles Calculations" as it appears in Journal of the Electrochemical Society, Zhi Deng, Zhenbin Wang, Iek-Heng Chu, Jian Luo and Shyue Ping Ong, 2016, 163 (2), pp A67-A74. The dissertation author was the primary investigator and author of this paper. The data calculations were done by collaborator, Zhenbin Wang.

Chapter 5

Composition Optimization of the Lithium-Rich Anti-Perovskite

Discovering solid electrolytes with high ionic conductivity is the top priority in developing all-solid-state lithium batteries. A common strategy to further boost ionic conductivity in experiments is composition tuning. Simulations using first principles methods primarily focus on the effect of local atomic environments. A bridging model is required to connect localized effects to ionic conductivity at long range.

In this chapter, we present a composition optimization strategy by changing the anion framework in $Li_3OCl_{1-x}Br_x$ anti-perovskites. First, we investigate the halide sublattice ordering and the relationship between migration barriers and local halide environments from first principles calculations. Based on the results, we then develop a bond percolation model that is able to identify compositions with potentially improved ionic conductivity. In the end, we validate the predictions using AIMD simulations.

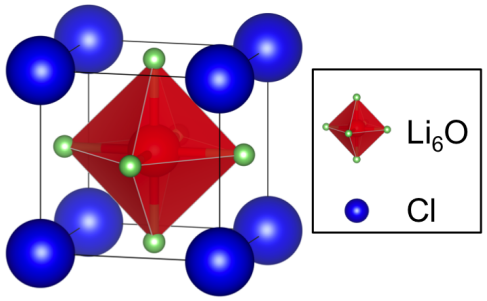

Figure 5.1: Unit cell of the Li_3OCl anti-perovskite. O occupies the body-centered site. Li occupy faced-centered sites forming a Li_6O octahedron with O. Cl occupies the corner sites.

5.1 Lithium-Rich $Li_3OCl(Br)$ Anti-Perovskite

The lithium-rich anti-perovskites (LiRAPs) with formula Li_3OX, where X = Cl, Br, or a mixture of both halogens, (shown in Figure 5.1) reported by Zhao *et al.* present an interesting class of superionic conductors with the potential in further composition optimization to increase the ionic conductivity.[82] Zhao *et al.* reported that the Li_3OCl end member has a room-temperature ionic conductivity of 0.85 mS/cm, and the mixed halide $Li_3OCl_{0.5}Br_{0.5}$ has a significantly higher conductivity of 1.94 mS/cm.[82] However, Li_3OBr shows much poorer conductivity compared with Li_3OCl and $Li_3OCl_{0.5}Br_{0.5}$ (though no actual conductivity value was reported). The authors postulated that the presence of smaller Cl creates larger channel for Li diffusion, while partial Br substitution prevents octahedral tilting from shrinking the channel size.

There have been several theoretical works on understanding the transport mechanisms in the LiRAPs. Using AIMD simulations, Zhang *et al.* demonstrated that Li vacancies and structural disorder promote the diffusion of Li in LiRAP.[83] Later, Emly *et al.* proposed a migration mechanism involving Li interstitial dumbbells, where the barrier is calculated to be around 50% lower than that for vacancy driven migration.[84] However, the authors also pointed out that this mechanism cannot explain the superionic conductivity of LiRAP due to the high formation energy of Li interstitial defects.[84] A work by Mouta *et al.* also showed that the formation energy of Li Frenkel defect is much higher than other intrinsic charge neutral defects in Li_3OCl.[111] While

these theoretical works have shed useful insights into the phase stability and ionic conductivity in the LiRAP superionic conductors, they stop short of providing a concrete optimization strategy for further enhancing their performance.

In this work, we present a comprehensive analysis of the phase stability and ionic conduction mechanisms in the LiRAPs using a combination of first principles calculations and percolation theory. Consistent with previous theoretical work, we find relatively low halide mixing energies in the LiRAPs, indicating that the mixed halide $Li_3OCl_{1-x}Br_x$ is likely to be disordered at room temperature. Using nudged elastic band (NEB) calculations, we elucidate the effect of the halide local environment on vacancy migration barriers. We then outline a rational composition optimization strategy for further enhancing the ionic conductivity of the LiRAP chemistry by incorporating the computed migration barriers into a bond percolation model. Finally, we provide supporting evidence from AIMD simulations that there exist potential compositions that yield even higher Li conductivities than $Li_3OCl_{0.5}Br_{0.5}$, the highest conductivity composition in the LiRAP chemistry identified experimentally thus far.

5.2 Computational Details

5.2.1 Structure Enumeration

For intermediate compositions of $Li_3OCl_{1-x}Br_x$, we enumerated all symmetrically distinct Cl and Br orderings at three compositions (x = 0.25, 0.5 and 0.75) in a $2 \times 2 \times 2$ supercell using the algorithm of Hart *et al.*[51] The ordered structures are shown in Figure 5.2.

5.2.2 Nudged Elastic Band Calculations

The nudged elastic band (NEB) method is frequently used to determine the barrier for Li migration under a specific path with certain nuclei configuration. In this method, a number of

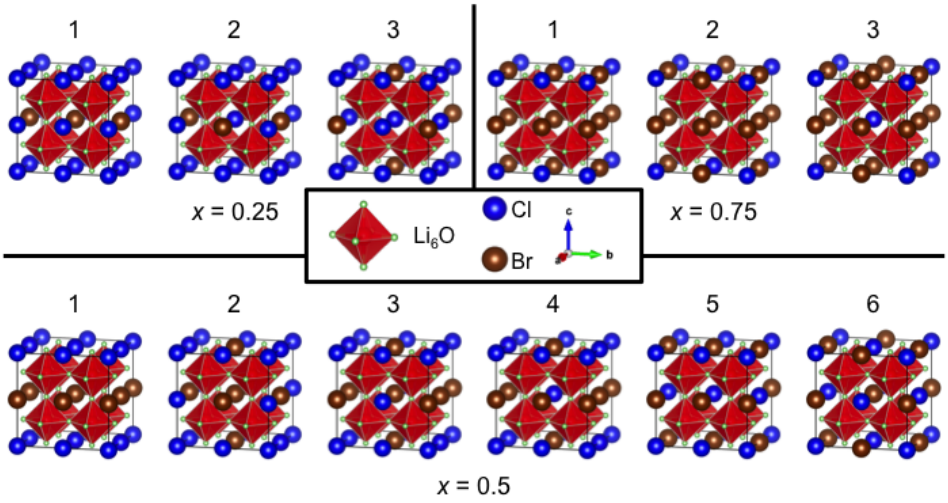

Figure 5.2: Ordered $Li_3OCl_{1-x}Br_x$ ($x = 0.25$, 0.5 and 0.75) $2 \times 2 \times 2$ supercells.

intermediate images along the migration path is optimized to find the lowest possible energy while maintaining spacing between neighboring images. This constrained optimization is achieved by adding "spring" forces along the band between images and projecting out the component of the force due to the potential perpendicular to the band.

In this work, NEB calculations were performed using $2 \times 2 \times 2$ supercells of $Li_3OCl_{1-x}Br_x$ with one negatively charged Li vacancy. The overall charge neutrality is preserved via a compensating background charge. Convergence tests with larger supercell sizes of Li_3OCl found that $2 \times 2 \times 2$ supercell is sufficient to obtain reasonably well-converged migration barrier. The migration pathway was constructed using five linearly interpolated images between fully relaxed initial and final points. Since our conclusions are predicated only on relative migration barrier differences, we did not perform any corrections for the interactions between periodic images of the charged vacancy; because the charges and structures are similar in all instances, the corrections would amount to approximately the same additive term.

To exclude the effect of the energy difference between the initial and final states, we calculated the the the kinetically resolved activation (KRA) barrier[112] for vacancy migration,

ΔE_{KRA}, as follows:

$$\Delta E_{\mathrm{KRA}} = E_{\mathrm{max}} - \frac{1}{2}\left(E_{\mathrm{init}} + E_{\mathrm{final}}\right), \tag{5.1}$$

where E_{max} is the saddle point energy along the pathway, E_{init} and E_{final} are the energy of the initial and final points, respectively. With hopping directions considered, the activation barrier is calculated as the following equation:

$$\Delta E_{\mathrm{f(b)}} = E_{\mathrm{max}} - E_{\mathrm{init(final)}}, \tag{5.2}$$

where ΔE_{f} is the activation barrier for the hop from the initial to the final point, and ΔE_{b} is the other way round.

5.2.3 AIMD simulations

We investigated the Li diffusivity and conductivity in anti-perovskite using AIMD simulations. Similar to the setup in previous work by Zhang *et al.*,[83] we carried out the AIMD simulations using a constant volume (NVT) ensemble on $2 \times 2 \times 2$ supercells of $Li_3OCl_{1-x}Br_x$ with a single Li vacancy. To ensure charge balance, a compensating background charge was applied. The volume and atomic positions of the unit cell were fully relaxed prior to the simulations. The integration of Newton's equation is based on the Verlet algorithm[113] implemented in VASP, and the time step of molecular dynamics was chosen to be 2 fs. At the start of the MD simulations, the samples were assigned an initial temperature of 300 K according to a Boltzmann distribution, then heated up to the desired temperature (900 to 2100 K) by velocity scaling and equilibrated at the desired temperature for 50000 time steps (100 ps) with a Nosé-Hoover thermostat.[114, 115] Although the MD simulations were performed at relatively high temperatures to ensure sufficient diffusion events and convergence of the diffusivity, no lattice melting was observed. The MD simulations then continued for approximately 300 ps until the diffusion coefficient was converged.

5.3 Halide Sublattice Ordering

To investigate the phase stability of the mixed halide $Li_3OCl_{1-x}Br_x$, we calculated the energies of all symmetrically distinct orderings at $x = 0.25$, 0.5 and 0.75 in a $2 \times 2 \times 2$ supercell and the two end members, Li_3OCl and Li_3OBr as well. The resulting Li_3OCl - Li_3OBr pseudo-binary phase diagram is shown in Figure 5.3a. The formation energies of all intermediate compositions are predicted to be small, positive values, suggesting solid solution behavior will likely prevail at room temperature. This is consistent with the fact that the $Li_3OCl_{0.5}Br_{0.5}$ compound has already been synthesized experimentally.[82] The narrow range of the formation energies at each composition further suggest that there is no single strongly preferred ordering of halide ions, indicating that the halide ion sublattice is likely to be disordered at temperatures of interest. These results are consistent with the earlier results reported by Emly *et al.*[84]

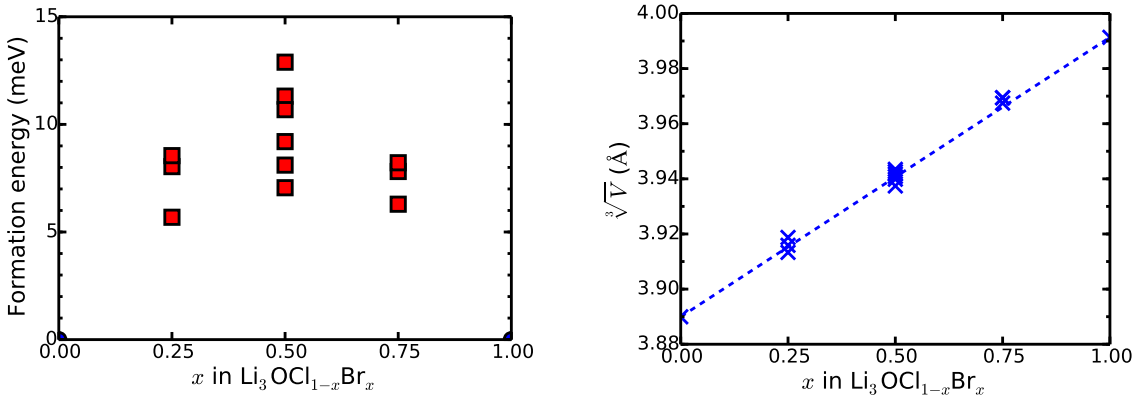

(a) (b)

Figure 5.3: (a) Computational Li_3OCl-Li_3OBr pseudo-binary phase diagram; (b) Calculated pseudo-cubic lattice parameter of $Li_3OCl_{1-x}Br_x$. The values in both figures are normalized to one formula unit of $Li_3OCl_{1-x}Br_x$.

The final relaxed lattice parameters of all calculated $Li_3OCl_{1-x}Br_x$ are plotted in Figure 5.3b. As all the final relaxed lattices have a pseudo-cubic structure with very minor differences in the lattice parameters in the *a*, *b* and *c* directions, we only report the averaged cubic lattice parameter for each structure. The calculated lattice parameters of the end members, Li_3OCl and

Li_3OBr are 3.89 Åand 3.99 Årespectively, in good agreement with the experimental lattice parameters and previous DFT calculations.[82, 83, 84] We find that the changes in lattice parameter with composition generally follow Vegard's law.

5.4 Dependence of Vacancy Migration Barrier on Halide Local Environment

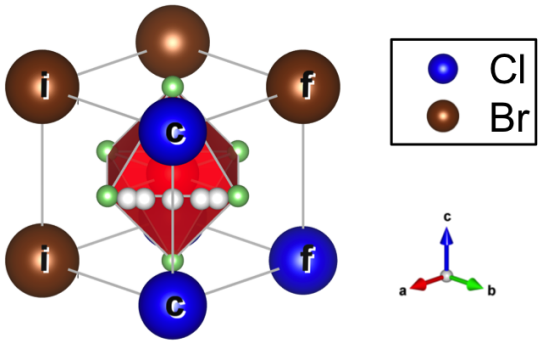

Figure 5.4: Schematic of BB-CC-BC pathway.

Figure 5.4 shows a schematic of a vacancy migration in the LiRAP structure. In LiRAP, each Li is coordinated by two oxygen ions (O) and four halide ions (X). Nearest neighbor Li share three coordinated anions (one O and two X). During a vacancy hop, the vacancy migrates from a Li site to a nearest Li site via a triangular channel comprising the three shared anions. We can then label such a hop using a $X_{ia}X_{ib}$-$X_{ca}X_{cb}$-$X_{fa}X_{fb}$ scheme, where $X_{ia}X_{ib}$ denotes the nearest neighbor halide ions to the initial site that are not shared with the final site, $X_{ca}X_{cb}$ denotes the halide ions in the channel shared between the initial and final sites, and $X_{fa}X_{fb}$ denotes the nearest neighbor halide ions to the final site that are not shared with the initial site. The letters i, c, and f represent "initial", "channel" and "final" respectively. The oxygen is not relevant for the labeling scheme since it is common to all hops. For example, the pathway in Figure 5.4 is labeled as BB-CC-BC (only the first letter for the halogen is used for brevity). It should be noted

that the specific order of the halide ions within each group is ignored, and we have excluded the effect of the energy differences between the initial and final sites by using the kinetically resolved activation (KRA) barrier.[112] In other words, the BB-CC-CB, BC-CC-BB and CB-CC-BB hops are considered equivalent to the BB-CC-BC hop. In general, we find that the effect of hopping direction on the barriers is negligible, which justifies the use of the KRA.

Based on the above labeling scheme, there are 18 distinct vacancy migration pathways in the mixed $Li_3OCl_{1-x}Br_x$ anti-perovskites. The majority of these pathways (12) can be found in at least one of the six distinct $2 \times 2 \times 2$ $Li_3OCl_{0.5}Br_{0.5}$ supercells, while the remaining (pathways containing a large number of halide ions of a particular type) can be found in the $Li_3OCl_{0.25}Br_{0.75}$ and $Li_3OCl_{0.75}Br_{0.25}$ structures. To exclude the effect of lattice parameter differences on the barrier, we minimized the number of different compositions used to perform the NEB calculations, though it was generally found that the minor differences in lattice parameters with composition have a relatively small effect on computed barriers.

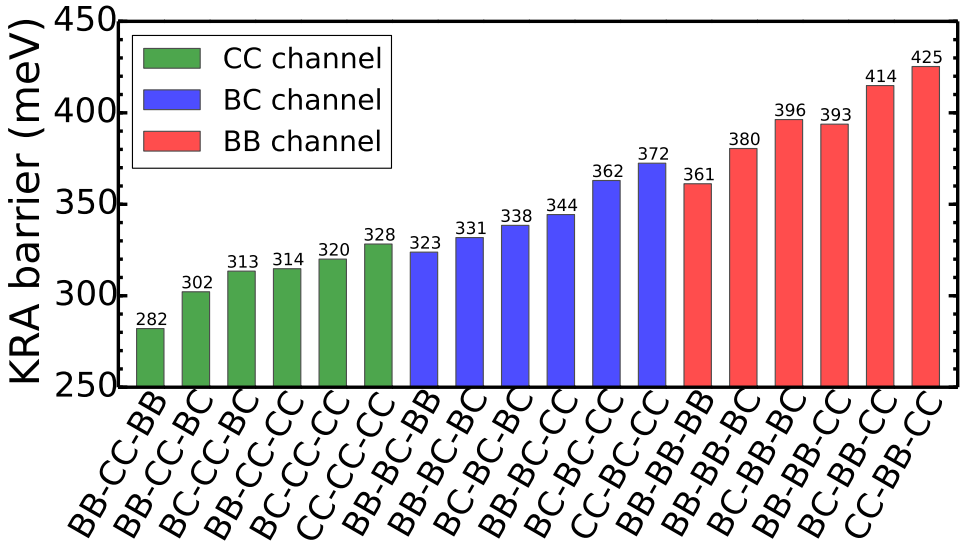

Figure 5.5: Vacancy migration barriers of different pathways from NEB calculations. The chart is divided into three regions according to the halide species in the channel.

Figure 5.5 shows the computed KRA barriers for all 18 distinct vacancy migration pathways. We note that the barriers obtained for the pure Li_3OCl and Li_3OBr (328 meV and 361

meV respectively) are consistently lower than those previously calculated by Zhang *et al.*[83] by about 40 meV, which is likely due to slight differences in calculation parameters. We may make a few key observations:

- The halide species in the channel have a large effect on the migration barrier. The migration barriers are significantly lower when the channel comprise only smaller Cl ions. The more Br ions are in the channel, the higher the migration barrier.

- The reverse trend is seen for the halide species that are not in the channel. Among pathways with a common channel XX, the CC-XX-CC pathway always has the highest migration barrier while increasing Br in the initial and final sites decreases the migration barrier.

We performed a multiple linear regression analysis to quantify the relationship between the vacancy migration barrier and the number of Br in the channel and endpoint (non-channel) sites. The relationship is given by the following equation:

$$\Delta E_a = 42.5 n_{\mathrm{c}}^{\mathrm{Br}} - 13.4 n_{\mathrm{e}}^{\mathrm{Br}} + 334.1, \tag{5.3}$$

where $n_{\mathrm{c}}^{\mathrm{Br}}$ and $n_{\mathrm{e}}^{\mathrm{Br}}$ are the number of Br at channel and endpoint sites respectively, and ΔE_a is the migration barrier in meV. We find that each Br in the channel sites increases the migration barrier by 43 meV, while each Br in the endpoint sites decreases the migration barrier by 13 meV.

It should be noted that Emly *et al.* performed a similar, but more limited analysis of the migration barrier in $Li_3OCl_{0.5}Br_{0.5}$ based on their proposed Li interstitial dumbbell mechanism.[84] Translating their results to our labeling scheme, they find that the relative migration barriers for three different dumbbell migration pathways are BC-CC-BC $<$ BC-BC-BC $<$ CC-BB-CC, which is qualitatively similar to our result that Cl in the channel leads to lower migration barriers. This is an important observation as it implies that the conclusion from the bond percolation analysis in the next section holds regardless of the specific diffusion mechanism.

5.5 Macroscopic Conductivity Modeling

Based on the results in the two preceding sections, we can conclude that (i) the mixed $Li_3OCl_{1-x}Br_x$ anti-perovskites are likely to exhibit disorder on the halide sublattice at temperatures of interest, and (ii) Cl in the channel and Br in the endpoints result in low energy migration pathways. However, these insights do not yet provide a concrete strategy for optimizing the conductivity in $Li_3OCl_{1-x}Br_x$. From purely the channel perspective, the Li_3OCl end member is already an "ideal" structure because all channels comprise Cl by definition; it is unclear what level of Br incorporation, if any, would result in a structure with increased conductivity. Any Br present would certainly increase the migration barriers of some pathways, while lowering the barriers of adjacent pathways. For macroscopically facile diffusion, a material must have low barrier paths that percolate through the entire crystal.

To derive an optimal Br concentration, we developed a bond percolation model for vacancy migration based on the halide-environment-dependent barriers from the NEB calculations. In this analysis, we define an "open bond" as a migration pathway whose energy barrier is less than a certain energy cut-off value. From the NEB calculations (Figure 5.5 and Equation 5.3), we note that the pure Cl channels generally result in the lowest migration barriers. We will therefore limit our analysis to the bonds with the pure Cl channels, and the barrier cutoffs can then be naturally selected based on the number of Br in the endpoints (n_e^{Br} in Equation 5.3). It should, however, be noted that the BB-BC-BB bond is predicted to have a lower barrier than the CC-CC-CC bond, though this type of bond only exists with significant probability at higher overall Br concentrations.

A key result from bond percolation theory is that there is a critical probability of open bonds, p_c, below which the network never percolates, and above which it does. Using the algorithm developed by Newman *et al.*[116], we estimate the bond percolation threshold of the lithium sublattice in the LiRAP structure to be 0.186, *i.e.*, percolation is achieved when

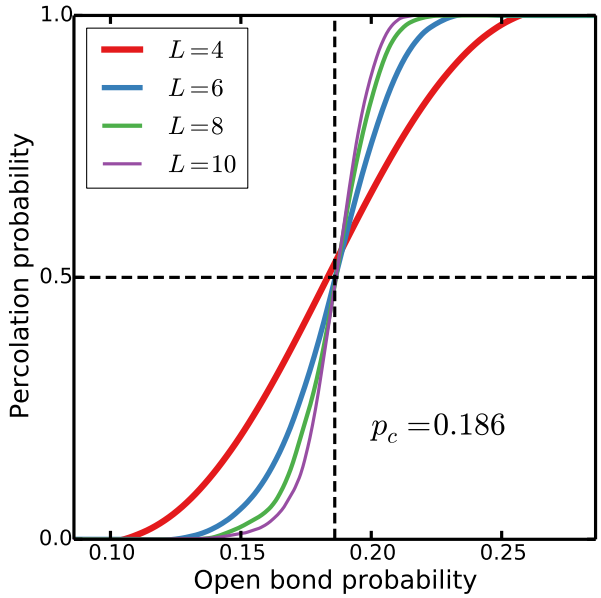

Figure 5.6: Percolation analysis of the Lithium sublattice in LiRAP structure using supercells of various sizes, $L : L \times L \times L$. Accounting for finite size effects, the bond percolation threshold, p_c, is calculated as 0.186, indicated by the vertical dotted line.

the probability of “open bonds" exceeds 0.186 in the LiRAP (Figure 5.6). We note that this threshold value is fairly close to that of the bcc structure (0.18),[117] which is consistent with the observation that in the LiRAP, each Li is similarly coordinated by 8 other Li ions.

Using a random sampling technique, we calculate the probability of open bonds in $Li_3OCl_{1-x}Br_x$ at various Br concentrations with different barrier cutoffs. As shown in Figure 5.7, when the barrier cutoff is set at 302 meV, only two types of bonds (BB-CC-BB and BB-CC-BC) are considered “open” and a percolating network of open bonds cannot be achieved at any concentration. When the cutoff is increased to 314 meV (bonds having at least 2 Br in the endpoints designated as open), percolation is achieved only within a narrow concentration range of $0.344 \leq x \leq 0.449$. The concentration range is further extended to $0.054 \leq x \leq 0.558$ when the cutoff is further increased to 323 meV. Finally, when the pure Cl halide environment (CC-CC-CC) is included as an open bond, percolation occurs from $0 \leq x \leq 0.565$, with the Li_3OCl having the highest probability (1.0) of having open bonds.

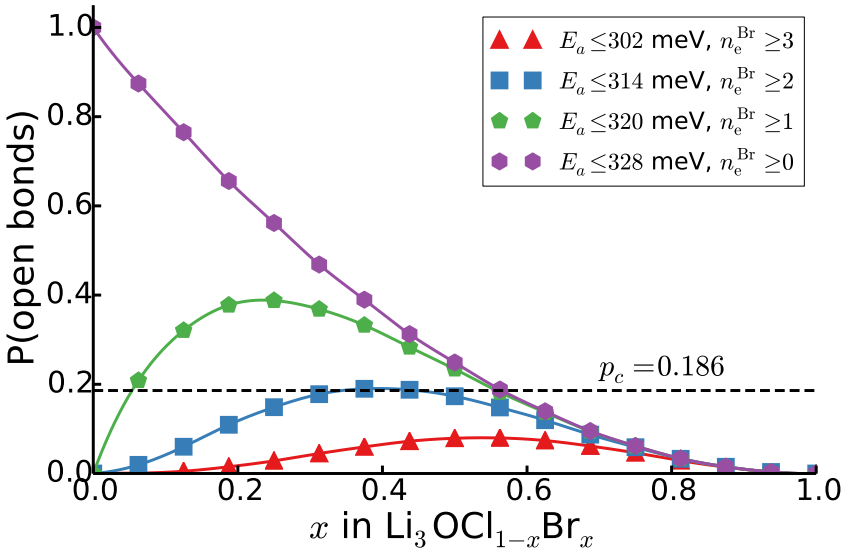

Figure 5.7: Probability of open bonds in $Li_3OCl_{1-x}Br_x$ at various Br concentrations. Each curve corresponds to a particular barrier cutoff. n_e^{Br} denotes the number of Br in the endpoints. The anti-perovskite bond percolation threshold is indicated by the black dashed line.

The proportion of open bonds for $n_e^{Br} \geq 2$ and 1 reaches a maximum of 0.191 and 0.388 at $x = 0.395$ and 0.235 respectively. The percolation analysis therefore suggests that there are potential compositions near $0.235 \leq x \leq 0.395$ that may yield conductivities higher than that of the $Li_3OCl_{0.5}Br_{0.5}$, the highest conductivity composition reported experimentally and theoretically thus far.

5.6 Confirmation from AIMD

To validate the predictions from our percolation model, we performed AIMD simulations for various halide orderings at $x = 0, 0.25, 0.5, 0.75, 1$. Figure 5.8 shows the ionic conductivities and activation energies associated with the highest Li conductivity at room temperature achieved at each composition. Both values come from the same structure as the ionic conductivity was extrapolated from Arrhenius equation. The overall trend in activation energies is similar to the NEB calculations. The extrapolated room temperature Li conductivities from our AIMD

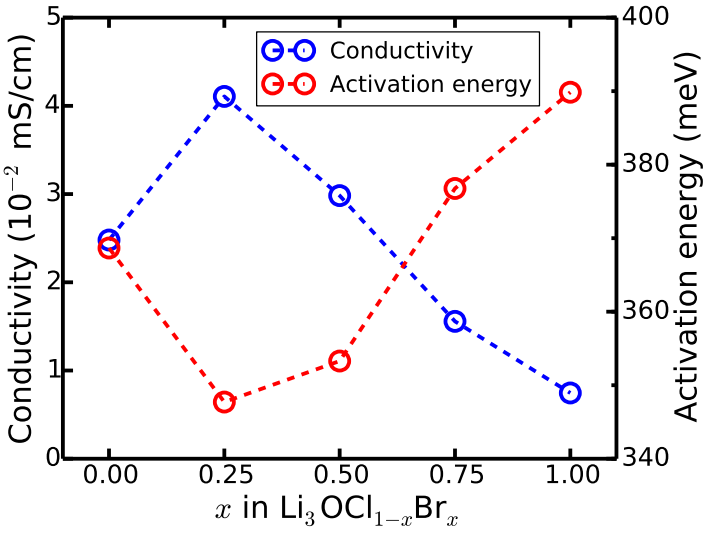

Figure 5.8: Overall activation energy, E_a and Li conductivity at room temperature as a function of x in $Li_3OCl_{1-x}Br_x$.

simulations are generally two orders of magnitude lower than those reported in the original experiments by Zhao *et al.*,[82] but are consistent with the values reported in a recent work by Lü *et al.*[118] Lü attributed the higher conductivities reported in the original experiments as possibly due to the formation of a depleted anti-perovskite $Li_{3-\delta}OCl_{1-\delta}$ or Al doping.[118] Nevertheless, the relevant observation here is the trend of conductivities with composition. Comparing the Li conductivities of $x = 0, 0.5, 1$, the trend in conductivity is $Li_3OCl_{0.5}Br_{0.5} > Li_3OCl > Li_3OBr$, in agreement with previous experimental and theoretical results.[82, 83] We also find that the maximum conductivity achieved by a $Li_3OCl_{0.75}Br_{0.25}$ is about 30% higher than that of $Li_3OCl_{0.5}Br_{0.5}$ composition, consistent with the predictions of our percolation model.

5.7 Discussion

Composition tuning is a frequently used and effective strategy for further enhancing ionic conductivity, particularly in lithium superionic conductors.[4, 119, 79] However, such tuning is typically carried out in a trial-and-error fashion, with only chemical intuition guiding

the selection of dopants and doping levels. For instance, while previous experimental work found the $Li_3OCl_{0.5}Br_{0.5}$ LiRAP to have a higher Li conductivity than the Li_3OCl and Li_3OBr end members, there was no indication, either from experiments or theory, on whether higher conductivity compositions exist within the the Li_3OCl-Li_3OBr pseudo-binary system.

Using a combination of first principles calculations and percolation theory, we have outlined a rational strategy to tune the disordered LiRAP composition to maximize the Li conductivity. We demonstrate that a Cl-rich channel with Br-rich endpoints leads to low vacancy migration barriers. By incorporating the computed local-environment-dependent migration barriers in a bond percolation model, we show that there are potentially higher conductivity $Li_3OCl_{1-x}Br_x$ structures near $0.235 \leq x \leq 0.395$. This prediction is further confirmed by AIMD simulations, which predict a higher conductivity for $Li_3OCl_{0.75}Br_{0.25}$ compared to $Li_3OCl_{0.5}Br_{0.5}$. It is our hope that this prediction will be verified experimentally subsequently.

The bond percolation model is key to the development of the composition optimization strategy. While the NEB calculations can provide insights into the local atomistic factors governing migration barriers, the bond percolation analysis extends that information to incorporate the compositional tradeoffs at the macroscopic level. Low levels of Br incorporation would increase the proportion of fast migration paths in the LiRAP structure, but an excess of Br incorporation would lead to "choking" in the channels and decreased conductivity. Our percolation analysis is similar in spirit to recent work by Urban *et al.*, who used a site percolation model to provide a unifying theory to explain the lithium exchange capacity of rocksalt-like structures.[120, 121] In this work, we have chosen to use a bond percolation analysis as it is more intuitively related to the facile pathways determined from NEB calculations. We also note that the specifics of the migration mechanism (vacancy or the earlier proposed interstitial dumbbell[84]) is largely irrelevant to the results from the bond percolation model; the only relevant factor is the relative migration barriers for different halide local environments, and this is similar for both mechanisms.

Finally, we wish to highlight that the approach and the percolation model outlined in

this work is surprisingly general and have applications beyond just Li conduction in the LiRAP system. For instance, oxygen ion conductivity in ABO_3 perovskites, such as $LaGaO_3$, is extremely important in fuel cells application.[122] A common strategy to boost the oxygen conductivity is to dope the A and B cation sites, such as Sr for La doping in the case of $LaGaO_3$. The LiRAP structures are isostructural with the ABO_3 perovskites, except that the sites occupied by the cations and anions are reversed. Hence, oxygen conduction in regular perovskites is equivalent to Li conduction in the anti-perovskite, and is governed by the same network topology and local environmental factors. Indeed, the optimal oxygen conductivity achieved in Sr doped $LaGaO_3$ thus far is at around 20% Sr doping level,[123] which is fairly close to the optimal Br doping level obtained in our model. Beyond the perovskite structure and topology, the model can also be trivially extended to study other diffusion network topologies.

5.8 Conclusion

In this work, we present a rational composition optimization strategy for maximizing the Li conductivity in the lithium-rich anti-perovskites (LiRAPs) guided by a combination of first principles calculations and percolation theory. The low mixing energies in the Li_3OCl-Li_3OBr pseudo-binary system indicate that halide disorder is likely at room temperature. Nudged elastic band (NEB) calculations find that a Cl-rich channel with Br-rich endpoints leads to low vacancy migration barriers in the LiRAP structure. By incorporating the computed NEB barriers in a bond percolation model, we show that there are potentially higher conductivity $Li_3OCl_{1-x}Br_x$ structures near $0.235 \leq x \leq 0.395$. We then confirm that this prediction using AIMD simulations, which predict a higher conductivity for $Li_3OCl_{0.75}Br_{0.25}$ compared to $Li_3OCl_{0.5}Br_{0.5}$, the highest conductivity composition in the anti-perovskite chemistry identified experimentally thus far. The approach developed in this work has applications beyond the LiRAP chemistry, and can potentially be extended to other perovskite ion-conducting systems such as the perovskite oxygen-

ion conductors of interest in solid-oxide fuel cells.

Chapter 5, in full, is a reprint of the material "Rational Composition Optimization of the Lithium-Rich $Li_3OCl_{1-x}Br_x$ Anti-Perovskite Superionic Conductors" as it appears in Chemistry of Materials, Zhi Deng, Balachandran Radhakrishnan and Shyue Ping Ong, 2015, 27 (10), pp 3749-3755. The dissertation author was the primary investigator and author of this paper.

Chapter 6

Developing Quantum-Accurate Force Field for Ionic Systems

While first principles calculations based on DFT are extremely powerful for modeling local atomic environments, phenomena regarding transport properties, such as diffusion and ionic conduction, usually occur at much larger time and length scales. A more general approach to break these constraints is constructing interatomic potentials via mapping local atomic environments to data (e.g., energy and force) from first principles calculations.

In this chapter, we present a quantum-accurate force field for ionic systems based on the spectral neighbor analysis potential (SNAP)[124] recently developed. We outline the process for constructing this force field including training data generation, proper feature engineering and the training/test iterations systematically improving energy and force predictions for MD simulations. We also demonstrate its application in large-scale Li diffusion studies.

6.1 Background

In recent years, a "mathematical" approach has gained popularity in constructing interatomic potentials with improved transferability over conventional empirical potentials.[38, 125, 39, 126, 124, 127] In this approach, the atomic coordinates are featurized using local environment descriptors that are invariant to translations, rotations and permutations of homo-nuclear atoms, and are differentiable and unique.[128, 126] A machine learning model is then trained to map the structural features to data (energies, forces, etc.) from first principles calculations. In general, such potentials have been demonstrated to achieve numerical accuracy close to first principles methods at much lower computational costs.[38, 39, 124, 127]

The coefficients of the bispectrum of local atomic density were first applied in the Gaussian approximation potential.[39] Thomson *et al.* later showed that a linear model of bispectrum coefficients from the lowest order - the so-called Spectral Neighbor Analysis Potential (SNAP) - can accurately reproduce DFT energies and forces as well as a variety of calculated properties (e.g., elastic constants and migration barrier for screw dislocation) in bcc Ta and W.[124, 129] More recently, the SNAP formalism has been extended to bcc Mo, fcc Ni and Cu, and the binary fcc Ni-bcc Mo alloy systems and showed that it outperforms conventional embedded atom method (EAM) and modified EAM potentials across a wide range of properties.[130, 131] Thus far, SNAP models have mainly been developed for metallic systems.

For ionic systems (e.g., superionic conductors), a common strategy in constructing interatomic potentials is to incorporate long-ranged electrostatic interactions (e.g., through the use of the Ewald summation) on top of energy model. This has been done for both traditional empirical models[132, 133] as well as modern local atomic environment descriptor-based potentials(e.g., GAP for the mixed ionic-covalent GaN[39] and neural network potential for ZnO[125]). In this work, we present a highly accurate electrostatic spectral neighbor analysis potential (eSNAP) for ionic α-Li_3N. We outline the process for constructing eSNAP, including training data generation,

proper feature engineering and the training/test iterations systematically improving energy and force predictions on MD simulations. The constructed eSNAP is not only accurate in energy and force predictions, but also excels traditional Coulomb-Buckingham potential in structural property calculations, such as lattice constants, elastic constants and phonon dispersion curves. We also demonstrate the application of eSNAP in large-scale Li diffusion studies. We are able to reproduce the high Li mobility and anisotropic diffusion in bulk α-Li_3N observed experimentally. In addition, we find the twist grain boundary may facilitate the Li diffusion in Li_3N. This work aims at providing an approach to developing quantum-accurate force fields for multicomponent ionic systems under the SNAP formalism, enabling large scale atomistic simulations.

6.2 Electrostatic SNAP (eSNAP) Model

6.2.1 Coefficients of Bispectrum

The atomic environment around atom i at coordinates $\mathbf{r}$ can be described by its atomic neighbor density $\rho_i(\mathbf{r})$ with the following equation[39, 124]:

$$\rho_i(\mathbf{r}) = \delta(\mathbf{r}) + \sum_{r_{ii'}<R_{ii'}} f_c(r_{ii'}) w_{i'} \delta(\mathbf{r} - \mathbf{r_{ii'}}), \tag{6.1}$$

where $\mathbf{r_{ii'}}$ is the vector joining the coordinates of central atom i and its neighbor atom i', the cutoff function f_c ensures that the neighbor atomic density decays smoothly to zero at cutoff radius $R_{ii'}$, and the dimensionless neighbor weights $w_{i'}$ distinguish atoms of different types. This density function can be expanded as a generalized Fourier series in the 4D hyper-spherical harmonics $U^j_{m,m'}(\theta,\phi,\theta_0)$ as follows:

$$\rho_i(\mathbf{r}) = \sum_{j=0,\frac{1}{2},\ldots}^{\infty} \sum_{m=-j}^{j} \sum_{m'=-j}^{j} u^j_{m,m'} U^j_{m,m'}(\theta,\phi,\theta_0), \tag{6.2}$$

where the coefficients $u^j_{m,m'}$ are given by the inner product $\langle U^j_{m,m'}|\rho\rangle$. The bispectrum coefficients are then given as:

$$B_{j_1,j_2,j} = \sum_{m_1,m_1'=-j_1}^{j_1} \sum_{m_2,m_2'=-j_2}^{j_2} \sum_{m,m'=-j}^{j} \left(u^j_{m,m'}\right)^* H^{jmm'}_{j_1 m_1 m_1' \; j_2 m_2 m_2'} u^{j_1}_{m_1,m_1'} u^{j_2}_{m_2,m_2'}, \tag{6.3}$$

where the constants $H^{jmm'}_{j_1 m_1 m_1' \; j_2 m_2 m_2'}$ are coupling coefficients.

In the original formulation of the non-ionic SNAP model,[124] the energy and forces are expressed as a linear function of the bispectrum coefficients, as follows:

$$E_{SNAP} = \sum_\alpha \left(\beta_{\alpha,0} N_\alpha + \sum_{k=\{j_1,j_2,j\}} \beta_{\alpha,k} \sum_{i=1}^{N_\alpha} B_{k,i}\right) \tag{6.4}$$

$$\mathbf{F}_{j,SNAP} = -\sum_\alpha \sum_{k=\{j_1,j_2,j\}} \beta_{\alpha,k} \sum_{i=1}^{N_\alpha} \frac{\partial B_{k,i}}{\partial \mathbf{r}_j}. \tag{6.5}$$

where α is the chemical identity of atoms and $\beta_{\alpha,k}$ are the coefficients in the linear SNAP model for type α atoms.

6.2.2 Energy Contributions in Ionic Systems

For ionic systems, electrostatic interactions spanning in the entire range of inter-atomic distances are indispensable in the construction of energy model due to the long-range tail beyond the cutoff distance for local environment description (see Figure 6.1). In our proposed electrostatic SNAP (eSNAP) model, we write the total potential energy as the sum of the electrostatic contributions and the local (SNAP) energy due to the variations in atomic local environments (SNAP), as follows:

$$E_p = \gamma E_{el} + E_{SNAP} \tag{6.6}$$

$$\mathbf{F}_j = -\bigtriangledown_j E_p = -\gamma \bigtriangledown_j E_{el} - F_{j,SNAP} \tag{6.7}$$

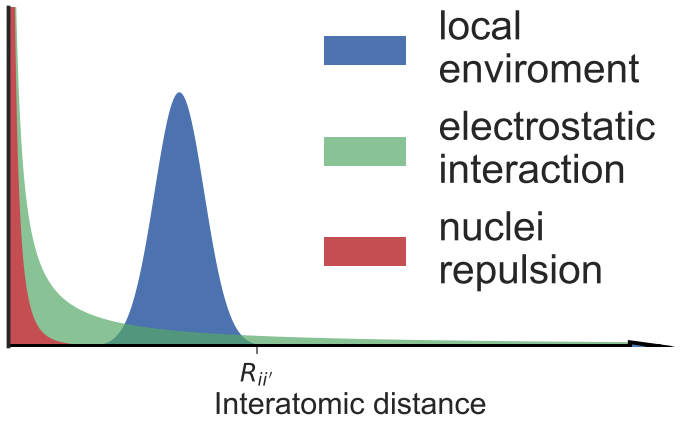

Figure 6.1: Schematic of energy contributions vs. interatomic distances in ionic systems. $R_{ii'}$ denotes the cutoff radius in considering contributions from local environment.

where E_{el} is the electrostatic energy computed using the Ewald summation approach[134] and γ is an effective screening prefactor for electrostatic interactions. The coefficients (γ and β) can be solved by fitting the linear model to total energies and forces from DFT calculations.

In addition, nuclei repulsion emerge at extremely short inter-atomic distances. In this work, the Ziegler-Biersack-Littmark (ZBL) potential is used to account for short-ranged nuclei repulsion.[135] To ensure that the fitting process captures the relevant relationship between the bispectrum coefficients and the DFT energies and forces, the cutoff distances of ZBL were chosen to be short enough ($R_i = 1.0$ Å, $R_o = 1.5$ Å) such that the ZBL potential has negligible contribution to energies or forces among the initial training configurations where extremely close inter-atomic distances were not sampled.

6.3 Potential Development

6.3.1 Training Data Generation

Figure 6.2 shows the hexagonal $P6/mmm$ unit cell of α-Li_3N, where Li2 sites form Li_2N layers with N sites in the ab plane and Li1 sites connect N sites in neighboring Li_2N layers along

the c axis. To sample a diverse set of configurations, the initial training set includes two major components:

1. Starting from the relaxed α-Li_3N unit cell, we first generated two series of unit cells with lattice distortions. One series samples different lattice constants a and c, and the other samples unit cells with different levels of strains (-1% to 1% at 0.2% intervals) applied in six different modes as described in the work by de Jong *et al.*[94]

2. Snapshots were extracted from *ab initio* molecular dynamic (AIMD) simulations at temperatures from 400 K to 1200 K at 200 K intervals under an NVT ensemble. Starting from a $3 \times 3 \times 3$ supercell with equilibrium volume, for each temperature, 200 snapshots were taken from a 40 ps AIMD simulation. A single Γ k-point and a much lower energy cutoff of 300 eV were used in AIMD simulations for rapid propagation of trajectories.

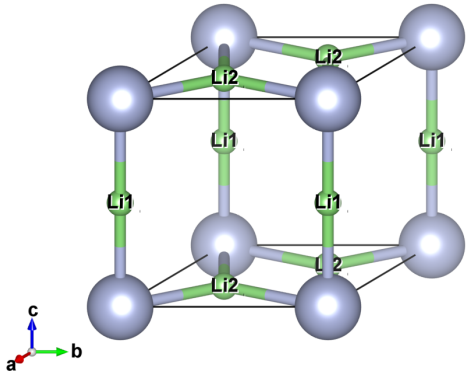

Figure 6.2: Unit cell of α-Li_3N.

To ensure accurate energies and forces, static DFT calculations were performed on all configurations with a plane-wave energy cutoff of 520 eV and Γ-centered k-point meshes with a density of at least 30 Å were employed.

Table 6.1: Number of configurations (N_{conf}), number of atoms (N_{atoms}), and sample weights on energy (w_E) and forces (w_F) for initial training data used in eSNAP model training.

Type	N_{conf}	N_{atoms}	w_E	w_F
Distorted unit cells	109	4	10^3	0
AIMD snapshots	1000	108	1	10^{-3}

6.3.2 Model Training and Test

Table 6.1 shows the weights applied on the different sets of training configurations during model training. As the initial training dataset contains many more configurations from AIMD snapshots with larger number of atoms, a much larger weight was applied on the energies of the distorted unit cells relative to those from the AIMD snapshots. A zero weight was applied on the negligibly small forces for the distorted unit cells.

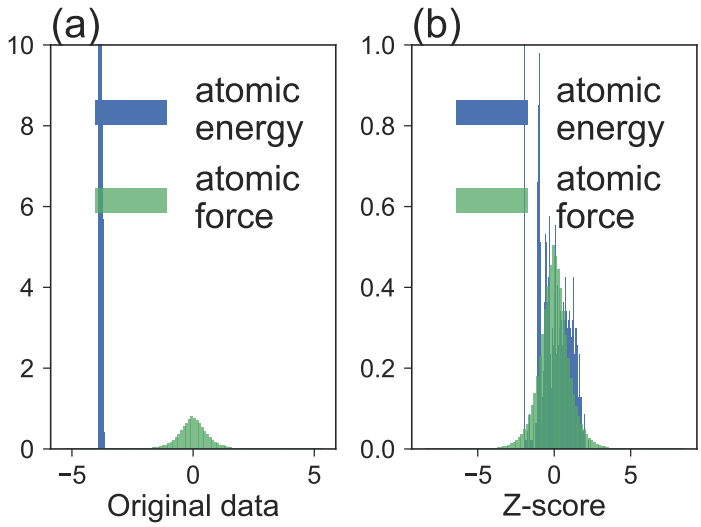

Figure 6.3: Distribution of (a) original atomic energies and forces and (b) normalized z-score of atomic energies and forces.

As shown in Figure 6.3a, the energies and forces differ greatly in magnitude and distribution due to differences in the scales and units. In the original SNAP training approach, the effect of this difference in magnitude and distribution is partially accounted for by treating the data weights as hyperparameters to be optimized.[130, 131] In this work, we use the standardized

z-scores of energies and forces (plotted in Figure 6.3b) as the targets in model training to avoid incorporating the effect of the distribution in the data weights, which are therefore fixed at the values in Table 6.1. The “standardized" eSNAP model in the fitting process is then given by the following:

$$\begin{bmatrix} \frac{e-\bar{e}}{\sigma_e} \\ \vdots \end{bmatrix} = \frac{1}{N\sigma_e} \begin{bmatrix} E_{el} & N_\alpha & \sum_{i=1}^{N_\alpha} B_{1,i} & \dots & \sum_{i=1}^{N_\alpha} B_{k,i} & \dots \\ \vdots & \vdots & \vdots & \dots & \vdots & \dots \end{bmatrix} \beta^{\mathrm{T}}, \tag{6.8}$$

$$\begin{bmatrix} \frac{\mathbf{F}_j}{\sigma_F} \\ \vdots \end{bmatrix} = \frac{1}{\sigma_F} \begin{bmatrix} -\frac{\partial E_{el}}{\partial \mathbf{r}_j} & 0 & -\sum_{i=1}^{N_\alpha} \frac{\partial B_{1,i}}{\partial \mathbf{r}_j} & \dots & -\sum_{i=1}^{N_\alpha} \frac{\partial B_{k,i}}{\partial \mathbf{r}_j} & \dots \\ \vdots & \vdots & \vdots & \dots & \vdots & \dots \end{bmatrix} \beta^{\mathrm{T}}, \tag{6.9}$$

where e is the energy per atom, $\bar{e}$ is the mean of e, and σ_e and σ_F are the standard deviations of e and F, respectively. The mean of forces is omitted since it is close to zero. The coefficient vector β^{T} to be solved can be written as:

$$\beta^{\mathrm{T}} = \begin{bmatrix} \gamma & \beta_{\alpha,0} - \bar{e} & \beta_{\alpha,1} & \dots & \beta_{\alpha,k} & \dots \end{bmatrix}^{\mathrm{T}}. \tag{6.10}$$

For bispectrum coefficient calculations, we used the implementation available in LAMMPS.[124] The two hyperparameters (cutoff distance R_α and atomic weight w_α) for each element (Li and N in the case of Li_3N) were determined using a two-step grid search scheme for the atomic weights and then followed by the cutoff distances. The mean absolute error (MAE) of forces from a linear model trained on the initial training set was chosen as the metric. For the atomic weights, it should be noted that the atomic density in ionic systems is generally higher than that in metallic systems; hence the search of atomic weights was performed in the range where $|w_\alpha| < 1$. Similarly, the search space for cutoff radius was limited to the range where $R_\alpha < 4$ Å. The results from grid search is shown in Figure 6.4, and the final hyperparameters are available in Table B.1.

Figure 6.5 show the flow chart of the iterative procedure used for training the eSNAP model in this work. A preliminary eSNAP model was first trained using the initial training set.

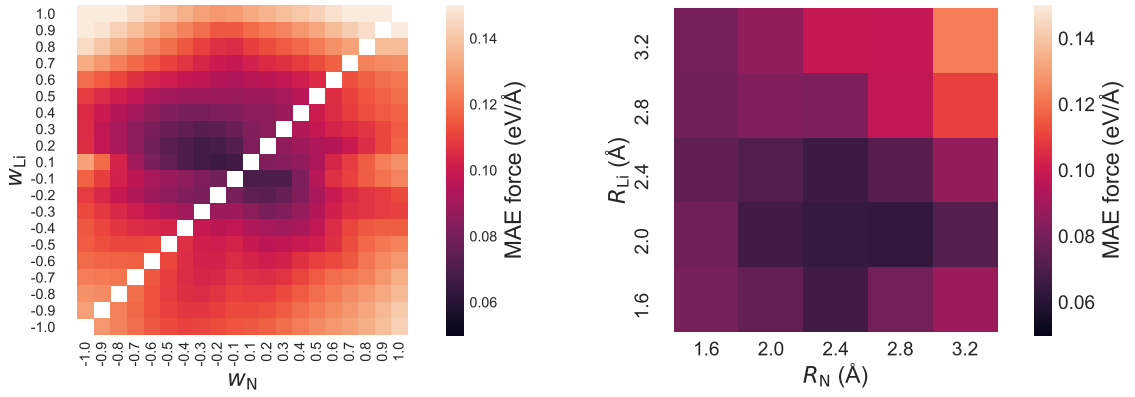

(a) (b)

Figure 6.4: Grid search of (a) atomic weights w_α and (b) cutoff distances R_α. Mean absolute error on forces is used as the metric.

Using this fitted eSNAP model, MD simulations were then carried out using a $3 \times 3 \times 3$ supercell in equilibrium volume at temperatures ranging from 300 K to 1200 K at 100 K intervals under an NVT ensemble for 40 ps. Ten snapshots were sampled from each MD simulation to form a new set of test configurations. Static DFT calculations were performed on these test configurations. If the test MAEs for both energies and forces are significantly larger than the corresponding training MAEs, the test set was then merged into the training set to form a new extended training set. The entire eSNAP fitting, simulation and testing procedure was repeated until there is no significant over-fitting. In this work, we use 150% of training MAE as the threshold to achieve a balance between the benefit gained by adding more training instances and the associated costs of performing more DFT calculations. It should be noted that this strategy is designed to bias the eSNAP model to improve the predictions on energy and force of MD snapshots, which is the target application of interest in this work.

6.3.3 Final Potential

The final hyperparameters and coefficients for SNAP are tabulated in Table B.1. For electrostatic interactions, the effective screening parameter γ is solved to be 0.057. All the MD

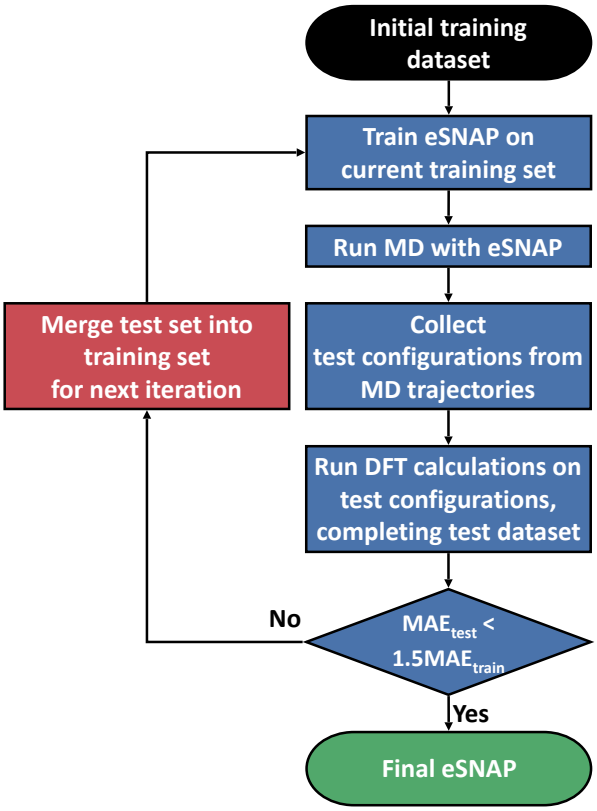

Figure 6.5: Flowchart of iterative procedure for eSNAP model training and test.

simulations with the eSNAP model were performed using LAMMPS.[136]

6.4 Performance of eSNAP

6.4.1 Energy and Force Predictions

Figures 6.6a-b shows the comparison between DFT calculated and eSNAP predicted energies and forces on both training and test dataset in the final iteration. Both energy and force predictions agree well with reference data from DFT calculations, indicating the eSNAP model has successfully captured the fundamental relationship between atomic environment and potential energy/atomic forces. The MAEs on energies and forces reached convergence after only two iterations, as shown in Figures 6.6c-d. In comparison, the MAE between DFT and the

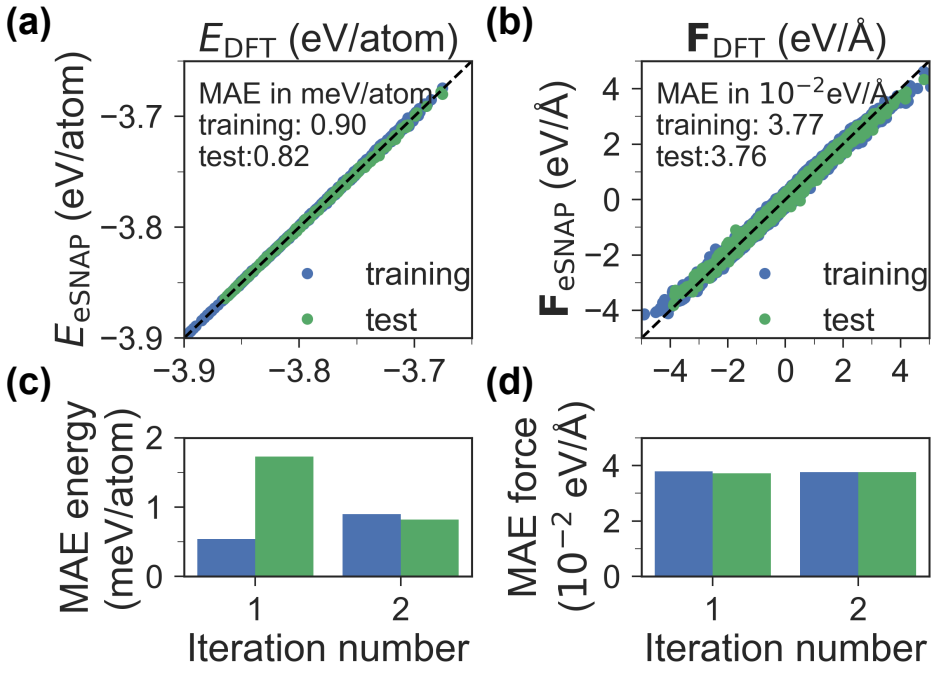

Figure 6.6: Energy and force prediction errors for eSNAP. Comparisons between DFT and eSNAP predictions for (a) energies and (b) forces on both training and test dataset in the final iteration. Convergence of the test and training MAEs for (c) energies and (d) forces with iteration number.

Coulomb-Buckingham potential by Walker and Catlow[137] on the initial training configuration pool are substantially higher for both energies (22 meV/atom) and forces (0.48 eV/Å).

6.4.2 Structural Properties

Table 6.2 compares the computed physical properties of α-Li_3N with different potential energy surfaces. The lattice constants calculated from eSNAP agree with those from DFT or experiments.[138] The elastic constants from eSNAP are close to those calculated using DFT, and surprisingly match experimental values except for c_{33}.[139] The agreements on structural properties can be expected from the fact that the energies of unit cells with various distortions have been fed to the model with a large sample weight. In comparison, the lattice constants and elastic constants from the Coulomb-Buckingham potential match poorly with either DFT or

Table 6.2: Calculated lattice constants a and c, elastic constants c_{ij} and Frenkel defect formation energies E_f (in two different configurations, intraplanar and interplanar) with DFT, eSNAP and Coulomb-Buckingham potential.[137] Lattice constants[138] and elastic constants[139] from experimental measurements are also listed for comparison.

	DFT	eSNAP	Coul-Buck	Exp.
a (Å)	3.641	3.641	3.528	3.648
c (Å)	3.874	3.872	3.628	3.875
c_{11} (GPa)	123	116	165	114
c_{33} (GPa)	137	144	193	118
c_{44} (GPa)	17	17	19	17
c_{66} (GPa)	48	39	53	38
$E_{f,\text{intra}}$ (eV)	0.60	0.64	0.50	
$E_{f,\text{inter}}$ (eV)	0.51	0.64	0.51	

experimental values, despite the fact that these physical properties were used to determine the potential parameters.[137]

We also calculated the formation energy of Li Frenkel defects, which contributes significantly to Li conductivity, in α-Li_3N (Table 6.2). Kishida *et al.* have shown earlier that vacancies are unlikely to form on Li1 sites,[140] and our investigations have found that any Frenkel defects created by introducing a vacancy on Li1 always relaxes back to the pristine Li_3N crystal in DFT. Here, we consider the two Frenkel configurations where a vacancy is introduced on Li2 and the interstitial Li is located at Li2 sites (intraplanar) or Li1 sites (interplanar). Both eSNAP and the Coulomb-Buckingham potential yield formation energies close to the values from DFT, but both of them failed at reproducing the energy difference between the two configurations.

Finally, Figure 6.7a compares the calculated phonon dispersion curves of α-Li_3N from eSNAP with those from DFT calculations. The phonon dispersion curves were calculated using the finite displacement approach on a $3 \times 3 \times 3$ supercell as implemented in the phonopy package.[141] We find that the phonon dispersion curves calculated from eSNAP are in good agreement with that from DFT. The only discrepancy is the imaginary phonon mode at Γ point observed in DFT phonon dispersion. According to Wu *et al.*, this lattice instability is associated with the vibration of Li2 sites along the c axis, resulting in a more stable phase that is only 0.3

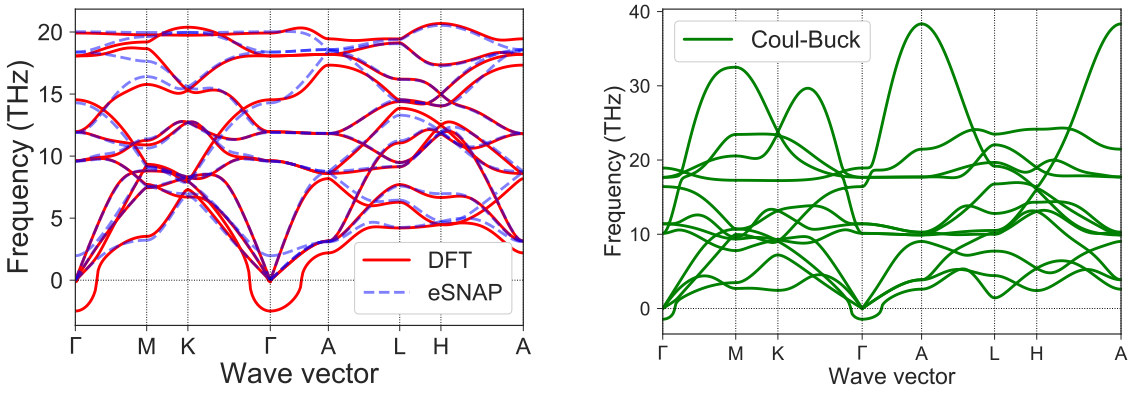

Figure 6.7: Phonon dispersion curves calculated from (a) DFT and eSNAP and (b) Coulomb-Buckingham potential.

meV/atom lower in energy after displacing Li2 site by ~ 0.1 Å.[142] This energy difference is well within the energy prediction error of the eSNAP model. We also note that the experimentally measured phonon dispersion curves at room temperature do not exhibit this lattice instability.[139] In contrast, the phonon dispersion curve calculated from the Coulomb-Buckingham potential show severely overestimated frequencies (Figure 6.7b) due to its unsatisfactory force prediction.

6.5 Large Scale Li Diffusion Studies

6.5.1 Bulk Diffusion

MD simulations were performed using the fitted eSNAP to investigate Li diffusion in bulk α-Li_3N. Built from the unit cell with equilibrium volume, the simulation box contains 4000 atoms ($10 \times 10 \times 10$ supercell). MD simulations were carried out at elevated temperatures from 600 to 1200 K in an NVT ensemble for 1 ns long or terminated early if the lattice melted.

The linear scaling with number of atoms and orders of magnitude lower computational cost of the eSNAP relative to DFT affords us the capability to compute the thermodynamic factor Θ. Using the approach proposed by Schnell[143], We estimated Θ from the fluctuation of

numbers of particles in a region that is representatively large but relatively small compared with the entire simulation box, using the following equation:

$$\Theta = \frac{\langle N \rangle}{\sigma_N^2}, \tag{6.11}$$

where $\langle N \rangle$ and σ_N are the mean and the standard deviation of number of particles over a period of time in that region, respectively. For the case of bulk α-Li_3N, we chose the center region with 1/8 volume of the simulation box and the fluctuation was calculated using the entire 1 ns long trajectory. Ionic conductivities were calculated using Equation 2.6, where D_σ is the product of self diffusivity D^* (from Equation 2.5) and thermodynamic factor Θ.

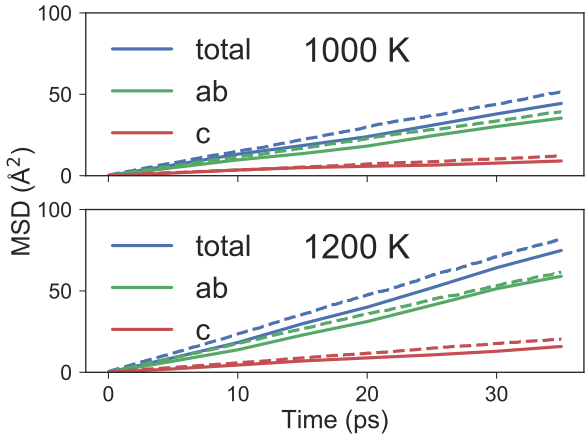

Figure 6.8: MSD vs. time plots for simulations running with AIMD (solid lines, smoothed) and eSNAP (dashed lines) at 1000 (upper) and 1200 (lower) K.

We calculated the MSD of Li with the trajectories from AIMD simulations at high temperatures (1000 and 1200 K) used for generating the initial training set. Runs at lower temperatures were not chosen due to the poor convergence of diffusivity at limited simulation length (40 ps). To compare the MSD observed in eSNAP MD, we smoothed the curve from AIMD in the time interval of 10 ps. As shown in Figure 6.8, the similar slopes observed in both AIMD and eSNAP suggest high Li mobility and anisotropic diffusion in α-Li_3N are successfully reproduced with eSNAP MD simulations. The MSD calculated from eSNAP MD is slightly

higher, which might be attributed to the difficulties to reach statistical convergence in AIMD with limited system size.

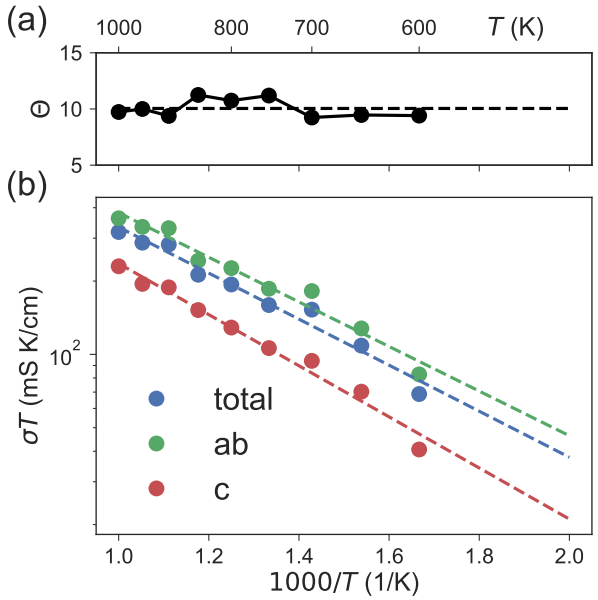

Figure 6.9: (a) Calculated thermodynamic factors and (b) Arrhenius plot for Li conductivity in bulk α-Li_3N obtained from eSNAP MD simulations.

Conductivity was calculated for temperatures ($\leq$ 1000 K) where the lattice did not melt during MD simulation. The thermodynamic factor Θ is plotted in Figure 6.9a. Throughout the entire simulated temperature range, the thermodynamic factor remains a constant $\sim$ 10, suggesting the diffusion is strongly influenced by the interactions among Li ions. As shown in Figure 6.9b, σT generally follows an Arrhenius relationship for both directions (in *ab* plane and along *c* axis) as well as the total value. The activation energies and extrapolated room temperature conductivities are tabulated in Table 6.3. The values in *ab* plane obtained in eSNAP MD are in reasonably good agreement with experiments measured with single crystals.[3] The major discrepancy is found for the values along *c* axis, where the much lower activation energy leads to overestimation in room temperature ionic conductivity. It should be noted that though the majority of modeling attempts were able to reveal the anisotropic diffusion in α-Li_3N, they failed at reproducing or explaining the high activation energy along *c* axis measured experimentally.[144, 145] Unfortunately, eSNAP

is not able to make a breakthrough, probably because it was constructed based on *ab initio* simulations and the issue is thus inherited.

Table 6.3: Comparison of activation energy (E_a) and room temperature ionic conductivity (σ_{RT}) obtained from eSNAP MD and experiments. Both values are reported by directions to directly compare with experimental measurements.[3]

		eSNAP MD	Exp.[3]
E_a	*ab*	0.248	0.290
(eV)	*c*	0.274	0.490
	total	0.254	
σ_{RT}	*ab*	1.52	1.2
(mS/cm)	*c*	0.46	0.01
	total	1.14	

6.5.2 Grain Boundary Diffusion

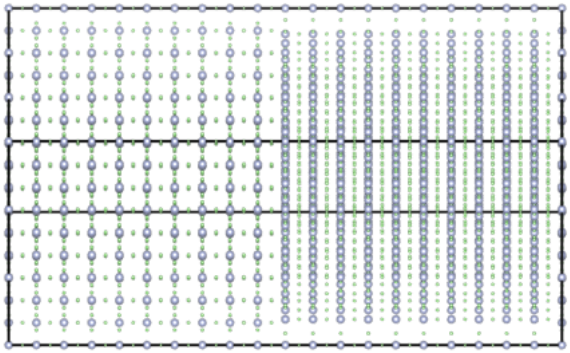

Figure 6.10: Constructed simulation boxes with twist Σ7 [0001] grain boundaries.

To investigate Li diffusion in grain boundaries, we constructed a simulation box with twist Σ7 [0001] grain boundaries as shown in Figure 6.10. Due to the default periodic boundary condition, two grain boundaries separated by 10× lattice vector *c* present in the box. The whole box contains 5040 atoms in total. Similar with diffusion study in the bulk, MD simulation was carried out under an NVT ensemble. At equilibrium stage, the simulation box was thermalized at 300 K for 30 ps. The simulation then continued for 1 ns at 300 K.

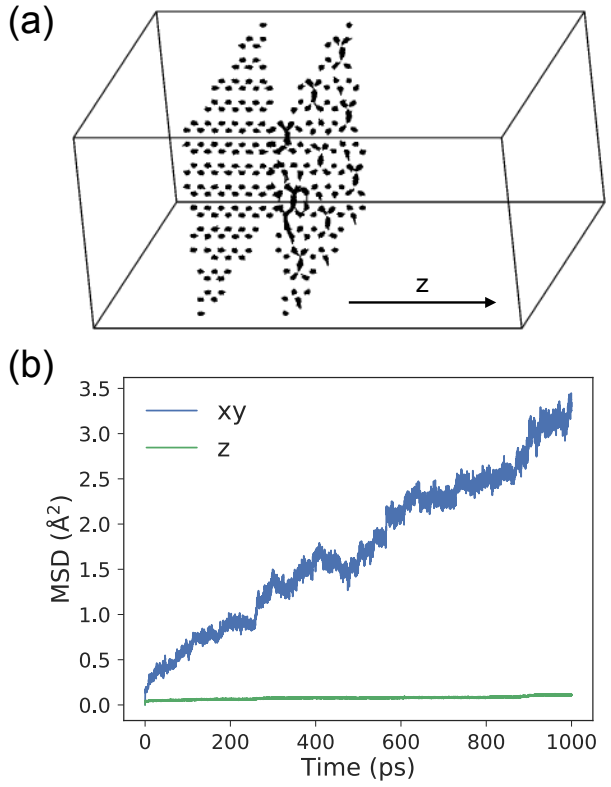

Figure 6.11: (a) Trajectories for selected Li ions in the box with twist grain boundaries in 0.5 ns. Li ions on the left lie in the bulk region, and the ones on the right are close to one of the grain boundaries. (b) MSD vs. time plot for Li ions in twist grain boundaries during simulation. The grain boundaries are in parallel with xy plane.

By visualizing the trajectories of Li ions, we can observe that:

1. As shown in Figure 6.11a, the Li ions near the twist grain boundary undergo countable nearest neighbor migration events, while the ones in the bulk barely moved in the 0.5 ns duration of MD simulation;

2. Migrations only occur along the directions (x and y) parallel to the grain boundaries, suggesting no Li ion exchanging between bulk and grain boundary.

We quantify the grain boundary diffusivity of Li by tracing the Li ions in the grain boundary region. Figure 6.11b shows the MSD for Li ions within grain boundaries during MD simulation. The 2D self-diffusivity calculated is 7.09×10^{-8} cm^2/s, about 3 times of extrapolated total value

(2.24×10^{-8} cm^2/s in 3D) in the bulk at 300 K.

6.6 Discussion

Developing an interatomic potential for any multicomponent systems has always been challenging majorly due to the increased number of parameters to be determined. For a multicomponent system sharing similar physical properties as elemental systems forming its composition (e.g., SiC and alloys), simple mixing rules utilizing potential parameters for elemental systems might not be sufficient, thus requiring either additional parameters or additional data with intermediate compositions in model fitting.[146, 131] The mixing rules will become completely broken for simple binary ionic systems like Li_3N, of which the properties are totally different from elements. An overlooked benefit of SNAP model is the number of parameters (coefficients of linear model) linearly scaling with the number of elements in the system, and they can be determined in one-shot linear regression. Thus constructing interatomic potentials for multicomponent systems becomes much easier from a mathematical standpoint, even for systems like Li_3N where everything has to be built from scratch. The machine learning algorithm used in SNAP model training is simple linear regression, not in need of a huge number of data points and unlikely to suffer from overfitting, but still systematically improvable by feeding more training data. It has enabled the training/test iteration we proposed to be done within reasonable computational budget on performing DFT calculations. It should be noted that we did not apply quadratic SNAP in our model for the sake of cost saving, where the additional quadratic terms may require a lot more data points, though it can potentially yield better accuracy in energy and force predictions.[129]

Although the fitting procedure seems straightforward, completing the entire process is still in need of human intervention. To the authors' experience, the choice of hyperparameters, especially the atomic weight w_α, is critical to the success of eSNAP for Li_3N. Using wrong atomic weights may result in similar predictive power on the training configurations, but the force

field will fail when running MD simulations with it. Erratic behaviors, such as atomic segregation with potential energy a few thousands eV lower than normal crystals, will appear in MD with constructed potential. Since such issues are difficult to identify in the model training stage, the generation of additional test configurations by running MD with constructed potential is thus even more important. This also applies to other potentials based on parametric models, where the existence of unreasonable configurations in a deep potential well is unknown. Whether a systematic approach for determining atomic weights in arbitrary multicomponent SNAP models exists or not, remains an open question to be discussed with more specific cases.

Unlike in earlier works where the sample weights are treated as hyperparameters optimized towards structural properties (lattice constants, elastic constants, etc.),[130, 131] here we used fixed sample weights in linear regression as the different scales between energies and forces are unified by using standardized Z-score as targets. As a result of large sample weights on the energies of unit cells with distortions, lattice constants and elastic constants are well matched as expected. Other properties where the calculations involves atomic relaxations, such as defect formation energies, are more difficult to match as the relevant atomic environment might not be covered in the training configuration pool.

With eSNAP for α-Li_3N, we are able to run MD simulations on much larger systems and access longer time scale while enjoying similar accuracy compared with AIMD. One example is the calculation of thermodynamic factor. A large value (> 1) might apply for other superionic conductors like Li_3N since the Li ions are condensed and interacting with each other. Large thermodynamic factors might be one of the reasons to explain the overestimated ionic conductivities from AIMD simulations.[147, 36] Another study concludes that the presence of grain boundaries facilitates Li diffusion in Li_3N. It is quite counterintuitive since grain boundaries are believed to have high resistance for ionic conduction. It should be noted that the grain boundaries in real polycrystalline materials may have much more complex atomic arrangements, with the presence of not just defects, but also other substances such as secondary phases or even impurities.

Potential impact on diffusion from these micro structures, however, might be beyond the scope of MD simulations with grain boundaries.

As a final note, the constructed eSNAP model only works with solid α-Li_3N phase. In principle, the transferability across other phases, such as molten state and other solid phases, can be achieved by feeding relevant configurations to the model. However, including many other atomic local environments may reduce the predictive power on those of more interests. We argue that the selection of training configurations should be based on the application of potential, rather than having all the possibilities exist or do not even exist in nature.

6.7 Conclusion

In this work, we present a highly accurate electrostatic spectral neighbor analysis potential (eSNAP) for ionic α-Li_3N. We outline the process for constructing eSNAP, including training data generation, proper feature engineering and the training/test iterations systematically improving energy and force predictions on MD snapshots. The constructed eSNAP is not only accurate in energy and force predictions, but also excels traditional Coulomb-Buckingham potential in structural property calculations, such as lattice constants, elastic constants and phonon dispersion curves. We also demonstrate the application of eSNAP in large-scale Li diffusion studies. We are able to reproduce the high Li mobility and anisotropic diffusion in bulk α-Li_3N observed experimentally. In addition, we find the twist grain boundary may facilitate the Li diffusion in Li_3N. This work aims at providing an approach to developing quantum-accurate force fields for multicomponent ionic systems under the SNAP formalism, enabling large scale atomistic simulations for these systems.

Chapter 6, in full, is currently being prepared for submission for publication of the material “An Electrostatic Spectral Neighbor Analysis Potential (eSNAP) for Lithium Nitride”, Zhi Deng, Chi Chen, Xiang-Guo Li and Shyue Ping Ong. The dissertation author was the primary

investigator and author of this paper.

Chapter 7

Summary and Outlook

Inorganic solid electrolyte is the key component in an all-solid-state lithium battery. Developing solid electrolytes, with not only high ionic conductivity, but also good electrochemical stability and suitable mechanical properties, will always be the primary task in realizing all-solid-state lithium batteries with expected long cycle life and high energy density. In the first part of this thesis, we have employed first principles methods based on density functional theory (DFT) in investigating a series of properties required for solid electrolytes on a wide variety of candidate materials.

1. For the newly discovered lithium rich anti-perovskite (LiRAP) superionic conductor, we present a rational composition optimization strategy for maximizing its Li conductivity guided by a combination of first principles calculations and percolation theory. Using nudged elastic band (NEB) calculations, we show that a Cl-rich channel with Br-rich endpoints configuration leads to low vacancy migration barriers in the LiRAP structure. By incorporating the halide-environment-dependent NEB barriers in a bond percolation model, we predict that there are potentially higher conductivity $Li_3OCl_{1-x}Br_x$ structures near $0.235 \leq x \leq 0.395$. This prediction is confirmed by AIMD simulation that finds $Li_3OCl_{0.75}Br_{0.25}$ to have a higher Li conductivity than $Li_3OCl_{0.5}Br_{0.5}$, the highest conduc-

tivity LiRAP identified experimentally thus far. These results highlight that there is scope for further enhancing the conductivity in the LiRAP chemistry. The general approach developed can potentially be extended to other ion-conducting systems, such as the structurally similar perovskite oxygen-ion conductors of interest in solid-oxide fuel cells as well as other superionic conductors.

2. For argyrodite Li_6PS_5Cl superionic conductor, we present a detailed investigation on its phase stability, electrochemical stability and ionic conductivity using first principles methods aided by modern information technology infrastructure and software tools. We find that Li_6PS_5Cl is metastable with limited intrinsic electrochemical window of 1.7 ~ 2.3 V vs. Li/Li^+. In addition, we show that Li excess is crucial to enhancing its conductivity by increasing the occupancy of interstitial sites that promote long-range Li diffusion between cage-like frameworks.

3. Suitable mechanical properties are also desired for solid electrolytes, and less attention has been paid in this perspective. We present a comprehensive investigation of the elastic properties (the full elastic tensor, bulk, shear and Young's moduli, and Poisson's ratio) of 23 well-known ceramic alkali solid electrolyte candidates using first principles calculations. We find that the computed elastic moduli are in good agreement with experimental data (wherever available) and chemical bonding nature. The anion species and structural framework has a significant influence on the elastic properties, and the relative elastic moduli of the various classes of materials follow the order thiophosphate $<$ antiperovskite $<$ phosphate $<$ NASICON $<$ garnet $<$ perovskite. We discuss the implications of these findings in the context of fabrication, battery operation, and enabling a Li metal anode. The data computed in this work will also serve as a useful reference for future experiments as well as theoretical modeling of solid electrolytes for all-solid-state lithium batteries.

High computational costs, even with modern efficient DFT-based methods, generally

limit the application of first principles methods in MD simulations to relatively small and simple systems containing up to a few hundreds of atoms and sub-nanosecond time scales. Empirical potentials are cheaper, but generally fall short in numerical accuracy and transferability. In the second part of this thesis, we present a highly accurate electrostatic spectral neighbor analysis potential (eSNAP) for ionic α-Li_3N. We outline the process for constructing eSNAP, including training data generation, proper feature engineering and the training/test iterations systematically improving energy and force predictions on MD snapshots. The constructed eSNAP is not only accurate in energy and force predictions, but also excels traditional Coulomb-Buckingham potential in structural property calculations, such as lattice constants, elastic constants and phonon dispersion curves. We also demonstrate the application of eSNAP in large-scale Li diffusion studies. We are able to reproduce the high Li mobility and anisotropic diffusion in bulk α-Li_3N observed experimentally. In addition, we find the twist grain boundary may facilitate the Li diffusion in Li_3N. This work aims at providing an approach to developing quantum-accurate force fields for multicomponent ionic systems under the SNAP formalism, enabling large scale atomistic simulations.

Ionic conductivity has been, and still will be the primary consideration for developing inorganic solid electrolytes. In this thesis, we have advanced the understanding of factors controlling the ionic conductivity for anti-perovskite $Li_3OCl_{1-x}Br_x$ and argyrodite Li_6PS_5Cl. These rules, however, are strictly limited to a certain class of material. Universal rules for ionic conduction that apply for the majority of solid electrolyte materials are still lacking. The ionic conductivity itself is technically not an intrinsic property that can be obtained from DFT calculations only on the crystal structure. Several factors, such as defect level and disordered Li sites, can sometimes beyond the reach of DFT calculations due to the size limitation. Though the existence of such universal rules is unknown, they will be of great help in identifying new materials. Electrochemical stability is another critical factor for a solid electrolyte. Historically, solid electrolytes were expected to be firmly stable during battery cycling. However, just like

argyrodite, the majority of solid electrolytes have limited intrinsic electrochemical window. In Li-ion batteries, the formation of stable solid-electrolyte interphase (SEI) is the key for extended cycle life. Electrolyte additives can be used to manipulate SEI, while for solid electrolytes, dopants may achieve a similar role as the additives. Another interesting observation is, it seems like high ionic conductivity and stability (not limited to electrochemical) can be hardly achieved simultaneously. Hence, a comprehensive evaluation on both ends is necessary in characterizing a candidate material.

Having long been ignored, the issues with mechanical properties for solid electrolytes have emerged as more studies start to shift the focus onto real devices. In essence, these issues are part of the solid-solid interfacial issues in all-solid-state lithium batteries. Due to the buried nature of such interfaces, all the interfacial issues fall in the "forbidden area" for experimental characterizations. It is equivalently challenging for theoretical modelings as the phenomena span in multiple time and length scales. For example, simulations of chemical reactions need to be performed at electronic level using first principles methods, while the modeling of mechanical responses might require much larger scales even beyond atomistic simulations. Unfortunately, a simulation method that is able to capture all the phenomena at different levels does not exist. The scale has to be specified with certain approximations, such as elastic region in mechanical responses used in this thesis. To obtain insights at different levels, an effective method must be carefully chosen.

To study Li diffusion in a solid electrolyte, electronic level simulations are not necessarily irreplaceable and may have additional constraints in both time and length scales. We have made an attempt training the eSNAP model to learn the mapping between local atomic environment and DFT calculated energy and force in Li_3N. The force field successfully helps us performing large scale MD simulations, breaking the constraints of first principles methods. In principle, the improved transferability in this type of force fields should enable automatic generation of interatomic potentials from DFT calculations with little human intervention. However, there

are still a few roadblocks to complete automation, such as hyperparameter determination for descriptors. More robust strategies are to be discussed when more specific cases become available.

Appendix A

Elastic Properties Calculated from PBE and optB88-vdW functionals

Table A.1: Calculated full elastic tensor (C_{ij}), bulk modulus (B), shear modulus (G), Young's modulus (E), Poisson's ratio (ν) and Pugh's ratio (G/B) using the PBE functional.

Formula	Space group	C_{ij} (GPa)	Number of independent c_{ij}	B (GPa)	G (GPa)	E (GPa)	ν	G/B
		NASICON						
$LiTi_2(PO_4)_3$	$R\bar{3}c$	$\begin{bmatrix} 218.1 & 82.2 & 43.2 & 8.5 & 0.0 & 0.0 \\ 82.2 & 218.1 & 43.2 & -8.5 & 0.0 & 0.0 \\ 43.2 & 43.2 & 115.2 & 0.0 & 0.0 & 0.0 \\ 8.5 & -8.5 & 0.0 & 46.5 & 0.0 & 0.0 \\ 0.0 & 0.0 & 0.0 & 0.0 & 46.5 & 8.5 \\ 0.0 & 0.0 & 0.0 & 0.0 & 8.5 & 68.0 \end{bmatrix}$	6	92.5	55.6	139.0	0.25	0.60
$NaZr_2(PO_4)_3$	$R\bar{3}c$	$\begin{bmatrix} 173.3 & 77.2 & 53.9 & 9.8 & 0.0 & 0.0 \\ 77.2 & 173.3 & 53.9 & -9.8 & 0.0 & 0.0 \\ 53.9 & 53.9 & 105.8 & 0.0 & 0.0 & 0.0 \\ 9.8 & -9.8 & 0.0 & 52.8 & 0.0 & 0.0 \\ 0.0 & 0.0 & 0.0 & 0.0 & 52.8 & 9.8 \\ 0.0 & 0.0 & 0.0 & 0.0 & 9.8 & 48.0 \end{bmatrix}$	6	87.7	47.2	120.0	0.27	0.54
		Phosphate						
Li_3PO_4		$\begin{bmatrix} 117.5 & 42.5 & 33.1 & 0.0 & 0.0 & 0.0 \\ 42.5 & 119.1 & 57.4 & 0.0 & 0.0 & 0.0 \\ 33.1 & 57.4 & 124.9 & 0.0 & 0.0 & 0.0 \\ 0.0 & 0.0 & 0.0 & 39.4 & 0.0 & 0.0 \\ 0.0 & 0.0 & 0.0 & 0.0 & 40.7 & 0.0 \\ 0.0 & 0.0 & 0.0 & 0.0 & 0.0 & 53.3 \end{bmatrix}$	9	69.5	41.3	103.4	0.25	0.59
		Perovskite						
$Li_{1/8}La_{5/8}TiO_3$	$Pmm2$	$\begin{bmatrix} 282.8 & 104.5 & 98.3 & 0.0 & 0.0 & 0.0 \\ 104.5 & 285.5 & 123.9 & 0.0 & 0.0 & 0.0 \\ 98.3 & 123.9 & 269.9 & 0.0 & 0.0 & 0.0 \\ 0.0 & 0.0 & 0.0 & 70.3 & 0.0 & 0.0 \\ 0.0 & 0.0 & 0.0 & 0.0 & 82.1 & 0.0 \\ 0.0 & 0.0 & 0.0 & 0.0 & 0.0 & 93.2 \end{bmatrix}$	9	165.6	82.7	212.7	0.29	0.50
$Li_{1/2}La_{1/2}TiO_3$	$P2/c$	$\begin{bmatrix} 332.6 & 99.7 & 85.1 & 0.1 & 0.0 & 0.9 \\ 99.7 & 339.0 & 86.9 & 0.2 & -0.0 & 0.2 \\ 85.1 & 86.9 & 323.1 & 0.3 & 0.0 & 1.5 \\ 0.1 & 0.2 & 0.3 & 92.5 & 0.0 & -0.4 \\ 0.0 & -0.0 & 0.0 & 0.0 & 93.8 & -0.0 \\ 0.9 & 0.2 & 1.5 & -0.4 & -0.0 & 88.6 \end{bmatrix}$	13	170.8	102.2	255.6	0.25	0.60
		Garnet						
$Li_5La_3Nb_2O_{12}$	$Ia\bar{3}d$	$\begin{bmatrix} 160.4 & 72.7 & 72.7 & 0.0 & 0.0 & 0.0 \\ 72.7 & 160.4 & 72.7 & 0.0 & 0.0 & 0.0 \\ 72.7 & 72.7 & 160.4 & 0.0 & 0.0 & 0.0 \\ 0.0 & 0.0 & 0.0 & 53.5 & 0.0 & 0.0 \\ 0.0 & 0.0 & 0.0 & 0.0 & 53.5 & 0.0 \\ 0.0 & 0.0 & 0.0 & 0.0 & 0.0 & 53.5 \end{bmatrix}$	3	101.9	49.4	127.6	0.29	0.48
$Li_5La_3Ta_2O_{12}$	$Ia\bar{3}d$	$\begin{bmatrix} 163.6 & 72.8 & 72.8 & 0.0 & 0.0 & 0.0 \\ 72.8 & 163.6 & 72.8 & 0.0 & 0.0 & 0.0 \\ 72.8 & 72.8 & 163.6 & 0.0 & 0.0 & 0.0 \\ 0.0 & 0.0 & 0.0 & 56.4 & 0.0 & 0.0 \\ 0.0 & 0.0 & 0.0 & 0.0 & 56.4 & 0.0 \\ 0.0 & 0.0 & 0.0 & 0.0 & 0.0 & 56.4 \end{bmatrix}$	3	103.0	51.7	132.9	0.28	0.50

Continued on next page

Table A.1 continued.

Continued from previous page

Formula	Space group	C_{ij} (GPa)	Number of independent c_{ij}	B (GPa)	G (GPa)	E (GPa)	ν	G/B
$Li_7La_3Zr_2O_{12}$	$I4_1/acd$	$\begin{bmatrix} 177.1 & 86.4 & 79.5 & 0.0 & 0.0 & 0.0 \\ 86.4 & 177.1 & 79.5 & 0.0 & 0.0 & 0.0 \\ 79.5 & 79.5 & 206.9 & 0.0 & 0.0 & 0.0 \\ 0.0 & 0.0 & 0.0 & 75.5 & 0.0 & 0.0 \\ 0.0 & 0.0 & 0.0 & 0.0 & 75.5 & 0.0 \\ 0.0 & 0.0 & 0.0 & 0.0 & 0.0 & 67.8 \end{bmatrix}$	6	116.7	63.7	161.6	0.27	0.55
		Anti-Perovskite						
Li_3OCl	$Pm\bar{3}m$	$\begin{bmatrix} 94.7 & 30.3 & 30.3 & 0.0 & 0.0 & 0.0 \\ 30.3 & 94.7 & 30.3 & 0.0 & 0.0 & 0.0 \\ 30.3 & 30.3 & 94.7 & 0.0 & 0.0 & 0.0 \\ 0.0 & 0.0 & 0.0 & 42.1 & 0.0 & 0.0 \\ 0.0 & 0.0 & 0.0 & 0.0 & 42.1 & 0.0 \\ 0.0 & 0.0 & 0.0 & 0.0 & 0.0 & 42.1 \end{bmatrix}$	3	51.8	37.8	91.2	0.21	0.73
Li_3OBr	$Pm\bar{3}m$	$\begin{bmatrix} 84.1 & 31.2 & 31.2 & 0.0 & 0.0 & 0.0 \\ 31.2 & 84.1 & 31.2 & 0.0 & 0.0 & 0.0 \\ 31.2 & 31.2 & 84.1 & 0.0 & 0.0 & 0.0 \\ 0.0 & 0.0 & 0.0 & 43.0 & 0.0 & 0.0 \\ 0.0 & 0.0 & 0.0 & 0.0 & 43.0 & 0.0 \\ 0.0 & 0.0 & 0.0 & 0.0 & 0.0 & 43.0 \end{bmatrix}$	3	48.8	35.4	85.5	0.21	0.72
Na_3OBr	$Pm\bar{3}m$	$\begin{bmatrix} 64.2 & 16.3 & 16.3 & 0.0 & 0.0 & 0.0 \\ 16.3 & 64.2 & 16.3 & 0.0 & 0.0 & 0.0 \\ 16.3 & 16.3 & 64.2 & 0.0 & 0.0 & 0.0 \\ 0.0 & 0.0 & 0.0 & 20.7 & 0.0 & 0.0 \\ 0.0 & 0.0 & 0.0 & 0.0 & 20.7 & 0.0 \\ 0.0 & 0.0 & 0.0 & 0.0 & 0.0 & 20.7 \end{bmatrix}$	3	32.3	22.0	53.7	0.22	0.68
Na_3OCl	$Pm\bar{3}m$	$\begin{bmatrix} 70.5 & 14.3 & 14.3 & 0.0 & 0.0 & 0.0 \\ 14.3 & 70.5 & 14.3 & 0.0 & 0.0 & 0.0 \\ 14.3 & 14.3 & 70.5 & 0.0 & 0.0 & 0.0 \\ 0.0 & 0.0 & 0.0 & 18.9 & 0.0 & 0.0 \\ 0.0 & 0.0 & 0.0 & 0.0 & 18.9 & 0.0 \\ 0.0 & 0.0 & 0.0 & 0.0 & 0.0 & 18.9 \end{bmatrix}$	3	33.0	22.2	54.3	0.23	0.67
		Thiophosphate: Li_3PS_4						
Li_3PS_4	$Pnma$	$\begin{bmatrix} 29.6 & 10.5 & 17.8 & 0.0 & 0.0 & 0.0 \\ 10.5 & 37.3 & 16.5 & 0.0 & 0.0 & 0.0 \\ 17.8 & 16.5 & 50.1 & 0.0 & 0.0 & 0.0 \\ 0.0 & 0.0 & 0.0 & 12.4 & 0.0 & 0.0 \\ 0.0 & 0.0 & 0.0 & 0.0 & 10.1 & 0.0 \\ 0.0 & 0.0 & 0.0 & 0.0 & 0.0 & 13.0 \end{bmatrix}$	9	22.1	11.7	29.9	0.27	0.53
Li_3PS_4	$Pmn2_1$	$\begin{bmatrix} 55.2 & 20.0 & 21.4 & 0.0 & 0.0 & 0.0 \\ 20.0 & 49.2 & 25.1 & 0.0 & 0.0 & 0.0 \\ 21.4 & 25.1 & 44.1 & 0.0 & 0.0 & 0.0 \\ 0.0 & 0.0 & 0.0 & 13.9 & 0.0 & 0.0 \\ 0.0 & 0.0 & 0.0 & 0.0 & 15.2 & 0.0 \\ 0.0 & 0.0 & 0.0 & 0.0 & 0.0 & 12.3 \end{bmatrix}$	9	31.3	13.6	35.6	0.31	0.43

Continued on next page

Table A.1 continued.

Continued from previous page

Formula	Space group	C_{ij} (GPa)	Number of independent c_{ij}	B (GPa)	G (GPa)	E (GPa)	ν	G/B
		Thiophosphate: $Li_{10}MP_2S_{12}$						
$Li_{10}GeP_2S_{12}$	$P4_2mc$	$\begin{bmatrix} 40.1 & 26.8 & 12.0 & 0.0 & 0.0 & 0.0 \\ 26.8 & 40.1 & 12.0 & 0.0 & 0.0 & 0.0 \\ 12.0 & 12.0 & 45.0 & 0.0 & 0.0 & 0.0 \\ 0.0 & 0.0 & 0.0 & 7.5 & 0.0 & 0.0 \\ 0.0 & 0.0 & 0.0 & 0.0 & 7.5 & 0.0 \\ 0.0 & 0.0 & 0.0 & 0.0 & 0.0 & 14.8 \end{bmatrix}$	6	25.1	10.1	26.7	0.32	0.40
$Li_{10}SnP_2S_{12}$	$P4_2mc$	$\begin{bmatrix} 38.9 & 26.4 & 10.4 & 0.0 & 0.0 & 0.0 \\ 26.4 & 38.9 & 10.4 & 0.0 & 0.0 & 0.0 \\ 10.4 & 10.4 & 45.9 & 0.0 & 0.0 & 0.0 \\ 0.0 & 0.0 & 0.0 & 8.2 & 0.0 & 0.0 \\ 0.0 & 0.0 & 0.0 & 0.0 & 8.2 & 0.0 \\ 0.0 & 0.0 & 0.0 & 0.0 & 0.0 & 14.3 \end{bmatrix}$	6	24.2	10.4	27.2	0.31	0.43
$Li_{10}SiP_2S_{12}$	$P4_2mc$	$\begin{bmatrix} 40.9 & 27.8 & 13.4 & 0.0 & 0.0 & 0.0 \\ 27.8 & 40.9 & 13.4 & 0.0 & 0.0 & 0.0 \\ 13.4 & 13.4 & 43.5 & 0.0 & 0.0 & 0.0 \\ 0.0 & 0.0 & 0.0 & 8.3 & 0.0 & 0.0 \\ 0.0 & 0.0 & 0.0 & 0.0 & 8.3 & 0.0 \\ 0.0 & 0.0 & 0.0 & 0.0 & 0.0 & 13.4 \end{bmatrix}$	6	25.9	10.1	26.8	0.33	0.39
		Thiophosphate: $Li_7P_3S_{11}$						
$Li_7P_3S_{11}$	$P\bar{1}$	$\begin{bmatrix} 32.6 & 17.1 & 15.4 & 0.9 & 0.2 & -1.2 \\ 17.1 & 31.7 & 16.0 & 2.4 & 1.8 & 4.4 \\ 15.4 & 16.0 & 51.0 & -0.3 & -1.8 & 0.2 \\ 0.9 & 2.4 & -0.3 & 9.6 & -0.2 & 1.3 \\ 0.2 & 1.8 & -1.8 & -0.2 & 13.8 & -0.1 \\ -1.2 & 4.4 & 0.2 & 1.3 & -0.1 & 9.0 \end{bmatrix}$	21	23.0	10.1	26.5	0.31	0.44
		Thiophosphate: Argyrodite						
Li_6PS_5Cl	$F\bar{4}3m$	$\begin{bmatrix} 41.1 & 22.5 & 22.5 & 0.0 & 0.0 & 0.0 \\ 22.5 & 41.1 & 22.5 & 0.0 & 0.0 & 0.0 \\ 22.5 & 22.5 & 41.1 & 0.0 & 0.0 & 0.0 \\ 0.0 & 0.0 & 0.0 & 10.9 & 0.0 & 0.0 \\ 0.0 & 0.0 & 0.0 & 0.0 & 10.9 & 0.0 \\ 0.0 & 0.0 & 0.0 & 0.0 & 0.0 & 10.9 \end{bmatrix}$	3	28.7	10.2	27.4	0.34	0.36
Li_6PS_5Br	$F\bar{4}3m$	$\begin{bmatrix} 42.0 & 22.3 & 22.3 & 0.0 & 0.0 & 0.0 \\ 22.3 & 42.0 & 22.3 & 0.0 & 0.0 & 0.0 \\ 22.3 & 22.3 & 42.0 & 0.0 & 0.0 & 0.0 \\ 0.0 & 0.0 & 0.0 & 6.0 & 0.0 & 0.0 \\ 0.0 & 0.0 & 0.0 & 0.0 & 6.0 & 0.0 \\ 0.0 & 0.0 & 0.0 & 0.0 & 0.0 & 6.0 \end{bmatrix}$	3	28.8	7.4	20.3	0.38	0.26
Li_6PS_5I	$F\bar{4}3m$	$\begin{bmatrix} 42.8 & 20.3 & 20.3 & 0.0 & 0.0 & 0.0 \\ 20.3 & 42.8 & 20.3 & 0.0 & 0.0 & 0.0 \\ 20.3 & 20.3 & 42.8 & 0.0 & 0.0 & 0.0 \\ 0.0 & 0.0 & 0.0 & 11.4 & 0.0 & 0.0 \\ 0.0 & 0.0 & 0.0 & 0.0 & 11.4 & 0.0 \\ 0.0 & 0.0 & 0.0 & 0.0 & 0.0 & 11.4 \end{bmatrix}$	3	27.8	11.3	30.0	0.32	0.41

Continued on next page

Table A.1 continued.

Continued from previous page

Formula	Space group	C_{ij} (GPa)	Number of independent c_{ij}	B (GPa)	G (GPa)	E (GPa)	ν	G/B
		Thiophosphate: Na_3PS_4						
Na_3PS_4	$I\bar{4}3m$	$\begin{bmatrix} 45.3 & 12.5 & 12.5 & 0.0 & 0.0 & 0.0 \\ 12.5 & 45.3 & 12.5 & 0.0 & 0.0 & 0.0 \\ 12.5 & 12.5 & 45.3 & 0.0 & 0.0 & 0.0 \\ 0.0 & 0.0 & 0.0 & 7.7 & 0.0 & 0.0 \\ 0.0 & 0.0 & 0.0 & 0.0 & 7.7 & 0.0 \\ 0.0 & 0.0 & 0.0 & 0.0 & 0.0 & 7.7 \end{bmatrix}$	3	23.4	10.4	27.3	0.31	0.45
Na_3PS_4	$P\bar{4}2_1c$	$\begin{bmatrix} 42.7 & 8.0 & 16.1 & 0.0 & 0.0 & 0.0 \\ 8.0 & 42.7 & 16.1 & 0.0 & 0.0 & 0.0 \\ 16.1 & 16.1 & 43.8 & 0.0 & 0.0 & 0.0 \\ 0.0 & 0.0 & 0.0 & 10.1 & 0.0 & 0.0 \\ 0.0 & 0.0 & 0.0 & 0.0 & 10.1 & 0.0 \\ 0.0 & 0.0 & 0.0 & 0.0 & 0.0 & 10.1 \end{bmatrix}$	6	23.2	11.7	30.1	0.28	0.51

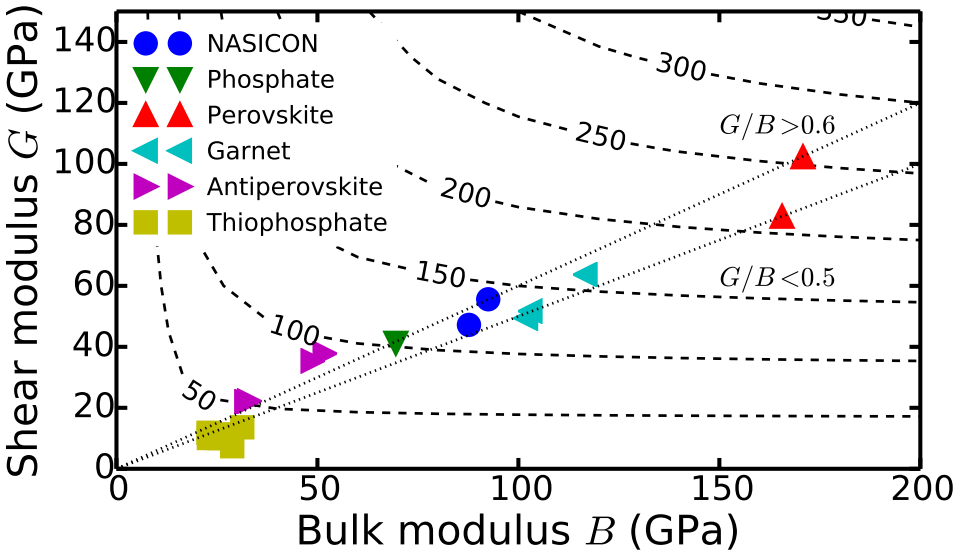

Figure A.1: Plot of the shear modulus (G) vs bulk modulus (B) for all investigated candidates calculated using the PBE functional. Dashed lines are the iso-Young's modulus lines in GPa. Two dotted lines correspond to $G/B = 0.5$ and $G/B = 0.6$.

Table A.2: Calculated full elastic tensor (C_{ij}), bulk modulus (B), shear modulus (G), Young's modulus (E), Poisson's ratio (ν) and Pugh's ratio (G/B) using the optB88-vdW functional.

Formula	Space group	C_{ij} (GPa)	Number of independent c_{ij}	B (GPa)	G (GPa)	E (GPa)	ν	G/B
		NASICON						
$LiTi_2(PO_4)_3$	$R\bar{3}c$	$\begin{bmatrix} 243.1 & 108.5 & 61.3 & 4.1 & 0.0 & 0.0 \\ 108.5 & 243.1 & 61.3 & -4.1 & 0.0 & 0.0 \\ 61.3 & 61.3 & 142.9 & 0.0 & 0.0 & 0.0 \\ 4.1 & -4.1 & 0.0 & 51.9 & 0.0 & 0.0 \\ 0.0 & 0.0 & 0.0 & 0.0 & 51.9 & 4.1 \\ 0.0 & 0.0 & 0.0 & 0.0 & 4.1 & 67.3 \end{bmatrix}$	6	115.1	59.6	152.4	0.28	0.52
$NaZr_2(PO_4)_3$	$R\bar{3}c$	$\begin{bmatrix} 180.0 & 93.2 & 62.6 & -1.8 & 0.0 & 0.0 \\ 93.2 & 180.0 & 62.6 & 1.8 & 0.0 & 0.0 \\ 62.6 & 62.6 & 115.3 & 0.0 & 0.0 & 0.0 \\ -1.8 & 1.8 & 0.0 & 21.3 & 0.0 & 0.0 \\ 0.0 & 0.0 & 0.0 & 0.0 & 21.3 & -1.8 \\ 0.0 & 0.0 & 0.0 & 0.0 & -1.8 & 43.4 \end{bmatrix}$	6	97.4	32.2	87.0	0.35	0.33
		Phosphate						
Li_3PO_4		$\begin{bmatrix} 121.0 & 48.6 & 40.4 & 0.0 & 0.0 & 0.0 \\ 48.6 & 131.1 & 67.9 & 0.0 & 0.0 & 0.0 \\ 40.4 & 67.9 & 132.7 & 0.0 & 0.0 & 0.0 \\ 0.0 & 0.0 & 0.0 & 39.2 & 0.0 & 0.0 \\ 0.0 & 0.0 & 0.0 & 0.0 & 41.8 & 0.0 \\ 0.0 & 0.0 & 0.0 & 0.0 & 0.0 & 54.6 \end{bmatrix}$	9	77.1	41.6	105.8	0.27	0.54
		Perovskite						
$Li_{1/8}La_{5/8}TiO_3$	$Pmm2$	$\begin{bmatrix} 271.4 & 97.7 & 96.0 & 0.0 & 0.0 & 0.0 \\ 97.7 & 314.0 & 124.2 & 0.0 & 0.0 & 0.0 \\ 96.0 & 124.2 & 273.9 & 0.0 & 0.0 & 0.0 \\ 0.0 & 0.0 & 0.0 & 74.5 & 0.0 & 0.0 \\ 0.0 & 0.0 & 0.0 & 0.0 & 87.0 & 0.0 \\ 0.0 & 0.0 & 0.0 & 0.0 & 0.0 & 95.8 \end{bmatrix}$	9	165.4	87.0	222.2	0.28	0.53
$Li_{1/2}La_{1/2}TiO_3$	$P2/c$	$\begin{bmatrix} 387.5 & 134.1 & 86.3 & 0.0 & -0.1 & -0.0 \\ 134.1 & 383.3 & 95.6 & 0.0 & -0.1 & -0.0 \\ 86.3 & 95.6 & 368.9 & 0.0 & -0.1 & -0.0 \\ 0.0 & 0.0 & 0.0 & 103.8 & -0.0 & 0.2 \\ -0.1 & -0.1 & -0.1 & -0.0 & 104.2 & 0.0 \\ -0.0 & -0.0 & -0.0 & 0.2 & 0.0 & 129.7 \end{bmatrix}$	13	196.4	121.2	301.7	0.24	0.62
		Garnet						
$Li_5La_3Nb_2O_{12}$	$Ia\bar{3}d$	$\begin{bmatrix} 174.9 & 77.5 & 77.5 & 0.0 & 0.0 & 0.0 \\ 77.5 & 174.9 & 77.5 & 0.0 & 0.0 & 0.0 \\ 77.5 & 77.5 & 174.9 & 0.0 & 0.0 & 0.0 \\ 0.0 & 0.0 & 0.0 & 57.1 & 0.0 & 0.0 \\ 0.0 & 0.0 & 0.0 & 0.0 & 57.1 & 0.0 \\ 0.0 & 0.0 & 0.0 & 0.0 & 0.0 & 57.1 \end{bmatrix}$	3	110.0	53.6	138.3	0.29	0.49
$Li_5La_3Ta_2O_{12}$	$Ia\bar{3}d$	$\begin{bmatrix} 176.8 & 78.1 & 78.1 & 0.0 & 0.0 & 0.0 \\ 78.1 & 176.8 & 78.1 & 0.0 & 0.0 & 0.0 \\ 78.1 & 78.1 & 176.8 & 0.0 & 0.0 & 0.0 \\ 0.0 & 0.0 & 0.0 & 60.2 & 0.0 & 0.0 \\ 0.0 & 0.0 & 0.0 & 0.0 & 60.2 & 0.0 \\ 0.0 & 0.0 & 0.0 & 0.0 & 0.0 & 60.2 \end{bmatrix}$	3	111.0	55.6	142.9	0.29	0.50

Continued on next page

Table A.2 continued.

Continued from previous page

Formula	Space group	C_{ij} (GPa)	Number of independent c_{ij}	B (GPa)	G (GPa)	E (GPa)	ν	G/B
$Li_7La_3Zr_2O_{12}$	$I4_1/acd$	$\begin{bmatrix} 228.2 & 108.5 & 104.6 & 0.0 & 0.0 & 0.0 \\ 108.5 & 228.2 & 104.6 & 0.0 & 0.0 & 0.0 \\ 104.6 & 104.6 & 260.9 & 0.0 & 0.0 & 0.0 \\ 0.0 & 0.0 & 0.0 & 85.9 & 0.0 & 0.0 \\ 0.0 & 0.0 & 0.0 & 0.0 & 85.9 & 0.0 \\ 0.0 & 0.0 & 0.0 & 0.0 & 0.0 & 73.7 \end{bmatrix}$	6	150.1	75.0	192.9	0.29	0.50
		Anti-Perovskite						
Li_3OCl	$Pm\bar{3}m$	$\begin{bmatrix} 106.9 & 31.4 & 31.4 & 0.0 & 0.0 & 0.0 \\ 31.4 & 106.9 & 31.4 & 0.0 & 0.0 & 0.0 \\ 31.4 & 31.4 & 106.9 & 0.0 & 0.0 & 0.0 \\ 0.0 & 0.0 & 0.0 & 46.1 & 0.0 & 0.0 \\ 0.0 & 0.0 & 0.0 & 0.0 & 46.1 & 0.0 \\ 0.0 & 0.0 & 0.0 & 0.0 & 0.0 & 46.1 \end{bmatrix}$	3	56.6	42.6	102.1	0.20	0.75
Li_3OBr	$Pm\bar{3}m$	$\begin{bmatrix} 95.3 & 32.8 & 32.8 & 0.0 & 0.0 & 0.0 \\ 32.8 & 95.3 & 32.8 & 0.0 & 0.0 & 0.0 \\ 32.8 & 32.8 & 95.3 & 0.0 & 0.0 & 0.0 \\ 0.0 & 0.0 & 0.0 & 47.1 & 0.0 & 0.0 \\ 0.0 & 0.0 & 0.0 & 0.0 & 47.1 & 0.0 \\ 0.0 & 0.0 & 0.0 & 0.0 & 0.0 & 47.1 \end{bmatrix}$	3	53.6	40.0	96.0	0.20	0.75
Na_3OBr	$Pm\bar{3}m$	$\begin{bmatrix} 72.3 & 16.3 & 16.3 & 0.0 & 0.0 & 0.0 \\ 16.3 & 72.3 & 16.3 & 0.0 & 0.0 & 0.0 \\ 16.3 & 16.3 & 72.3 & 0.0 & 0.0 & 0.0 \\ 0.0 & 0.0 & 0.0 & 22.3 & 0.0 & 0.0 \\ 0.0 & 0.0 & 0.0 & 0.0 & 22.3 & 0.0 \\ 0.0 & 0.0 & 0.0 & 0.0 & 0.0 & 22.3 \end{bmatrix}$	3	35.0	24.5	59.5	0.22	0.70
Na_3OCl	$Pm\bar{3}m$	$\begin{bmatrix} 80.9 & 15.7 & 15.7 & 0.0 & 0.0 & 0.0 \\ 15.7 & 80.9 & 15.7 & 0.0 & 0.0 & 0.0 \\ 15.7 & 15.7 & 80.9 & 0.0 & 0.0 & 0.0 \\ 0.0 & 0.0 & 0.0 & 21.6 & 0.0 & 0.0 \\ 0.0 & 0.0 & 0.0 & 0.0 & 21.6 & 0.0 \\ 0.0 & 0.0 & 0.0 & 0.0 & 0.0 & 21.6 \end{bmatrix}$	3	37.4	25.5	62.3	0.22	0.68
		Thiophosphate: Li_3PS_4						
Li_3PS_4	$Pnma$	$\begin{bmatrix} 37.1 & 12.2 & 20.5 & 0.0 & 0.0 & 0.0 \\ 12.2 & 39.4 & 18.8 & 0.0 & 0.0 & 0.0 \\ 20.5 & 18.8 & 56.4 & 0.0 & 0.0 & 0.0 \\ 0.0 & 0.0 & 0.0 & 10.1 & 0.0 & 0.0 \\ 0.0 & 0.0 & 0.0 & 0.0 & 10.6 & 0.0 \\ 0.0 & 0.0 & 0.0 & 0.0 & 0.0 & 19.7 \end{bmatrix}$	9	25.4	12.9	33.1	0.28	0.51
Li_3PS_4	$Pmn2_1$	$\begin{bmatrix} 60.8 & 23.9 & 24.2 & 0.0 & 0.0 & 0.0 \\ 23.9 & 54.4 & 29.4 & 0.0 & 0.0 & 0.0 \\ 24.2 & 29.4 & 50.6 & 0.0 & 0.0 & 0.0 \\ 0.0 & 0.0 & 0.0 & 13.7 & 0.0 & 0.0 \\ 0.0 & 0.0 & 0.0 & 0.0 & 15.7 & 0.0 \\ 0.0 & 0.0 & 0.0 & 0.0 & 0.0 & 13.1 \end{bmatrix}$	9	35.6	14.2	37.6	0.32	0.40

Continued on next page

Table A.2 continued.

Continued from previous page

Formula	Space group	C_{ij} (GPa)	Number of independent c_{ij}	B (GPa)	G (GPa)	E (GPa)	ν	G/B
		Thiophosphate: $Li_{10}MP_2S_{12}$						
$Li_{10}GeP_2S_{12}$	$P4_2mc$	$\begin{bmatrix} 46.5 & 30.2 & 14.3 & 0.0 & 0.0 & 0.0 \\ 30.2 & 46.5 & 14.3 & 0.0 & 0.0 & 0.0 \\ 14.3 & 14.3 & 53.3 & 0.0 & 0.0 & 0.0 \\ 0.0 & 0.0 & 0.0 & 9.8 & 0.0 & 0.0 \\ 0.0 & 0.0 & 0.0 & 0.0 & 9.8 & 0.0 \\ 0.0 & 0.0 & 0.0 & 0.0 & 0.0 & 16.6 \end{bmatrix}$	6	29.3	12.3	32.3	0.32	0.42
$Li_{10}SnP_2S_{12}$	$P4_2mc$	$\begin{bmatrix} 60.9 & 43.2 & 21.3 & 0.0 & 0.0 & 0.0 \\ 43.2 & 60.9 & 21.3 & 0.0 & 0.0 & 0.0 \\ 21.3 & 21.3 & 73.8 & 0.0 & 0.0 & 0.0 \\ 0.0 & 0.0 & 0.0 & 16.3 & 0.0 & 0.0 \\ 0.0 & 0.0 & 0.0 & 0.0 & 16.3 & 0.0 \\ 0.0 & 0.0 & 0.0 & 0.0 & 0.0 & 21.0 \end{bmatrix}$	6	40.7	16.9	44.4	0.32	0.41
$Li_{10}SiP_2S_{12}$	$P4_2mc$	$\begin{bmatrix} 65.4 & 41.1 & 22.6 & 0.0 & 0.0 & 0.0 \\ 41.1 & 65.4 & 22.6 & 0.0 & 0.0 & 0.0 \\ 22.6 & 22.6 & 74.7 & 0.0 & 0.0 & 0.0 \\ 0.0 & 0.0 & 0.0 & 8.3 & 0.0 & 0.0 \\ 0.0 & 0.0 & 0.0 & 0.0 & 8.3 & 0.0 \\ 0.0 & 0.0 & 0.0 & 0.0 & 0.0 & 16.5 \end{bmatrix}$	6	41.9	13.2	35.9	0.36	0.32
		Thiophosphate: $Li_7P_3S_{11}$						
$Li_7P_3S_{11}$	$P\bar{1}$	$\begin{bmatrix} 37.6 & 21.0 & 22.1 & 1.5 & -3.2 & -0.4 \\ 21.0 & 31.7 & 21.6 & -0.8 & 2.7 & 0.7 \\ 22.1 & 21.6 & 54.8 & -3.1 & -1.9 & 2.5 \\ 1.5 & -0.8 & -3.1 & 13.6 & 3.3 & 1.8 \\ -3.2 & 2.7 & -1.9 & 3.3 & 14.8 & -2.5 \\ -0.4 & 0.7 & 2.5 & 1.8 & -2.5 & 10.6 \end{bmatrix}$	21	27.4	10.5	27.9	0.33	0.38
		Thiophosphate: Argyrodite						
Li_6PS_5Cl	$F\bar{4}3m$	$\begin{bmatrix} 43.6 & 25.2 & 25.2 & 0.0 & 0.0 & 0.0 \\ 25.2 & 43.6 & 25.2 & 0.0 & 0.0 & 0.0 \\ 25.2 & 25.2 & 43.6 & 0.0 & 0.0 & 0.0 \\ 0.0 & 0.0 & 0.0 & 11.2 & 0.0 & 0.0 \\ 0.0 & 0.0 & 0.0 & 0.0 & 11.2 & 0.0 \\ 0.0 & 0.0 & 0.0 & 0.0 & 0.0 & 11.2 \end{bmatrix}$	3	31.4	10.3	27.9	0.35	0.33
Li_6PS_5Br	$F\bar{4}3m$	$\begin{bmatrix} 44.8 & 25.0 & 25.0 & 0.0 & 0.0 & 0.0 \\ 25.0 & 44.8 & 25.0 & 0.0 & 0.0 & 0.0 \\ 25.0 & 25.0 & 44.8 & 0.0 & 0.0 & 0.0 \\ 0.0 & 0.0 & 0.0 & 13.0 & 0.0 & 0.0 \\ 0.0 & 0.0 & 0.0 & 0.0 & 13.0 & 0.0 \\ 0.0 & 0.0 & 0.0 & 0.0 & 0.0 & 13.0 \end{bmatrix}$	3	31.6	11.6	31.1	0.34	0.37
Li_6PS_5I	$F\bar{4}3m$	$\begin{bmatrix} 46.4 & 23.5 & 23.5 & 0.0 & 0.0 & 0.0 \\ 23.5 & 46.4 & 23.5 & 0.0 & 0.0 & 0.0 \\ 23.5 & 23.5 & 46.4 & 0.0 & 0.0 & 0.0 \\ 0.0 & 0.0 & 0.0 & 13.6 & 0.0 & 0.0 \\ 0.0 & 0.0 & 0.0 & 0.0 & 13.6 & 0.0 \\ 0.0 & 0.0 & 0.0 & 0.0 & 0.0 & 13.6 \end{bmatrix}$	3	31.1	12.7	33.5	0.32	0.41

Continued on next page

Table A.2 continued.

Continued from previous page

Formula	Space group	C_{ij} (GPa)	Number of independent c_{ij}	B (GPa)	G (GPa)	E (GPa)	ν	G/B
		Thiophosphate: Na_3PS_4						
Na_3PS_4	$I\bar{4}3m$	$\begin{bmatrix} 55.3 & 16.4 & 16.4 & 0.0 & 0.0 & 0.0 \\ 16.4 & 55.3 & 16.4 & 0.0 & 0.0 & 0.0 \\ 16.4 & 16.4 & 55.3 & 0.0 & 0.0 & 0.0 \\ 0.0 & 0.0 & 0.0 & 12.0 & 0.0 & 0.0 \\ 0.0 & 0.0 & 0.0 & 0.0 & 12.0 & 0.0 \\ 0.0 & 0.0 & 0.0 & 0.0 & 0.0 & 12.0 \end{bmatrix}$	3	29.4	14.5	37.5	0.29	0.50
Na_3PS_4	$P\bar{4}2_1c$	$\begin{bmatrix} 55.4 & 13.8 & 18.8 & 0.0 & 0.0 & 0.0 \\ 13.8 & 55.4 & 18.8 & 0.0 & 0.0 & 0.0 \\ 18.8 & 18.8 & 45.9 & 0.0 & 0.0 & 0.0 \\ 0.0 & 0.0 & 0.0 & 13.3 & 0.0 & 0.0 \\ 0.0 & 0.0 & 0.0 & 0.0 & 13.3 & 0.0 \\ 0.0 & 0.0 & 0.0 & 0.0 & 0.0 & 14.9 \end{bmatrix}$	6	28.8	15.1	38.6	0.28	0.52

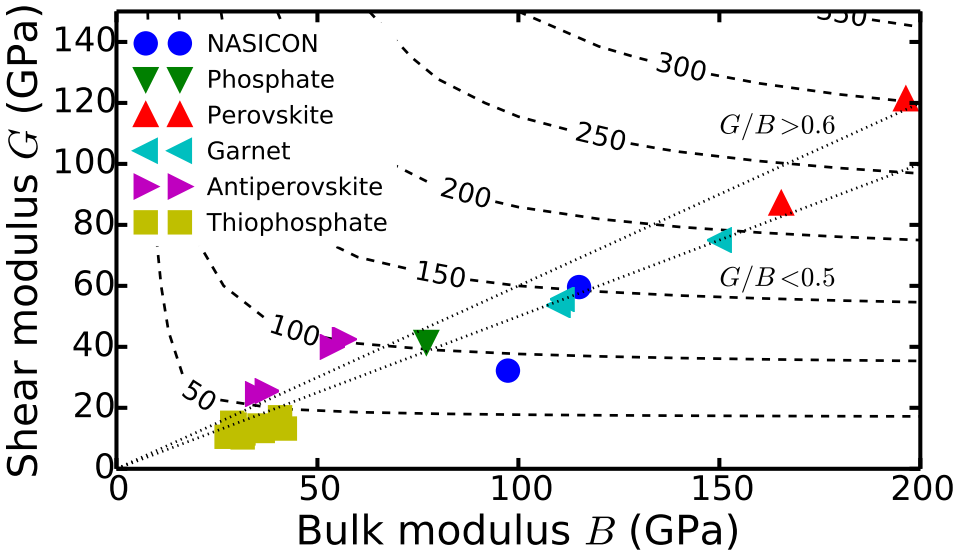

Figure A.2: Plot of the shear modulus (G) vs bulk modulus (B) for all investigated candidates calculated using the optB88-vdW functional. Dashed lines are the iso-Young's modulus lines in GPa. Two dotted lines correspond to $G/B = 0.5$ and $G/B = 0.6$.

Appendix B

SNAP parameters for Li_3N eSNAP

Table B.1: Final hyperparameters and coefficients of SNAP in Li_3N eSNAP.

				Li ($w = 0.1, R = 2.0$)	N ($w = -0.1, R = 2.8$)
k	$2j_1$	$2j_2$	$2j$	$\beta_{\mathrm{Li},k}$	$\beta_{\mathrm{N},k}$
0				-41.973239307589510000	5.070489350565292000
1	0	0	0	-0.006975291543708552	1.456429449741217000
2	1	0	1	1.943443830363772200	-0.741751895178898800
3	1	1	2	1.943960665209158600	1.391487252718133000
4	2	0	2	1.896372127297504700	-0.057993919814256490
5	2	1	3	0.818415025331073900	4.490489555500009000
6	2	2	2	-0.115525745627534120	1.038809274414984000
7	2	2	4	0.024662060558673055	2.017342084202995000
8	3	0	3	0.645913664832655000	0.297752638364790700
9	3	1	4	0.029473213939390678	2.234672087302177000
10	3	2	3	-0.835569404051590300	0.864212802963693300
11	3	2	5	0.260421577039490040	2.027941600818144300
12	3	3	4	-0.531877413286821100	0.534495092798581400
13	3	3	6	0.297955449169754300	0.299436757239075040
14	4	0	4	0.100238669102941730	-0.149453371719054230
15	4	1	5	-0.569297582876690400	0.541280152554589700
16	4	2	4	-0.683610621813019800	0.181446484735933700
17	4	2	6	0.076839221845524830	0.324534968809946260
18	4	3	5	0.157477937603063170	-0.112365239839474810
19	4	4	4	0.245396146771298870	0.143146336052880570
20	4	4	6	0.218995247596486900	0.008000929122986318
21	5	0	5	-0.203265539796318980	-0.191267051611771400
22	5	1	6	-0.232726613086012750	-0.167152854094159280
23	5	2	5	-0.352838031703020600	-0.369717312625315600
24	5	3	6	0.112930317776087000	-0.123035057771956320
25	5	4	5	0.537951697554698000	0.559745649003179100
26	5	5	6	0.082284784064962830	0.290496672932174600
27	6	0	6	-0.178966722576012600	-0.029092905917972420
28	6	2	6	-0.283676416415676500	-0.180134374249985380
29	6	4	6	0.089012939842931950	0.252331183046023500
30	6	6	6	0.044042461635336136	0.008318824055866198

Bibliography

[1] John B. Goodenough and Kyu Sung Park. The Li-ion rechargeable battery: A perspective. *J. Am. Chem. Soc.*, 135(4):1167–1176, 2013.

[2] https://phys.org/news/2016-03-solid-electrolytes-doors-solid-state-batteries.html.

[3] U V Alpen, A Rabenau, and G H Talat. Ionic conductivity in Li3N single crystals. *Appl. Phys. Lett.*, 30(12):621–623, 1977.

[4] Philippe Knauth. Inorganic solid Li ion conductors: An overview. *Solid State Ionics*, 180(14-16):911–916, 2009.

[5] Kazunori Takada. Progress and prospective of solid-state lithium batteries. *Acta Mater.*, 61(3):759–770, 2013.

[6] Kang Xu. Nonaqueous Liquid Electrolytes for Lithium-Based Rechargeable Batteries. *Chem. Rev.*, 104(10):4303–4418, oct 2004.

[7] H Y-P. Hong. Crystal structure and ionic conductivity of Li14Zn(GeO4)4 and other new Li+ superionic conductors. *Mater. Res. Bull.*, 13(2):117–124, 1978.

[8] J Kuwano and A.R. West. New Li+ ion conductors in the system, Li4GeO4-Li3VO4. *Mater. Res. Bull.*, 15(11):1661–1667, 1980.

[9] A. Khorassani, G. Izquierdo, and A. R. West. The solid electrolyte system, Li3PO4Li4SiO4. *Mater. Res. Bull.*, 16(12):1561–1567, 1981.

[10] Hiromichi Aono, Eisuke Sugimoto, Yoshihiko Sadaoka, Nobuhito Imanaka, and Gin-ya Adachi. Ionic Conductivity of the Lithium Titanium Phosphate (Li1+ X M X Ti2âĹŠ X (PO 4) 3, M= Al, Sc, Y, and La) Systems. *J. Electrochem. Soc.*, 136:590–591, 1989.

[11] Yoshiyuki Inaguma, Chen Liquan, Mitsuru Itoh, and Tetsuro Nakamura. High Ionic Conductivity in Lithium Lanthanum Titanate. *Solid State Commun.*, 86(10):689–693, 1993.

[12] Ryoji Kanno and Masahiro Murayama. Lithium Ionic Conductor Thio-LISICON: The Li[sub 2]S-GeS[sub 2]-P[sub 2]S[sub 5] System. *J. Electrochem. Soc.*, 148(7):A742, 2001.

[13] Fuminori Mizuno, Akitoshi Hayashi, Kiyoharu Tadanaga, and Masahiro Tatsumisago. New, highly ion-conductive crystals precipitated from Li 2S-P2S5 glasses. *Adv. Mater.*, 17(7):918–921, 2005.

[14] Ramaswamy Murugan, Venkataraman Thangadurai, and Werner Weppner. Fast lithium ion conduction in garnet-type Li7La3Zr2O12. *Angew. Chemie Int. Ed.*, 46(41):7778–7781, jan 2007.

[15] Noriaki Kamaya, Kenji Homma, Yuichiro Yamakawa, Masaaki Hirayama, Ryoji Kanno, Masao Yonemura, Takashi Kamiyama, Yuki Kato, Shigenori Hama, Koji Kawamoto, and Akio Mitsui. A lithium superionic conductor. *Nat. Mater.*, 10(9):682–686, 2011.

[16] Yuki Kato, Satoshi Hori, Toshiya Saito, Kota Suzuki, Masaaki Hirayama, Akio Mitsui, Masao Yonemura, Hideki Iba, and Ryoji Kanno. High-power all-solid-state batteries using sulfide superionic conductors. *Nat. Energy*, 1(4):16030, 2016.

[17] Yifei Mo, Shyue Ping Ong, and Gerbrand Ceder. First Principles Study of the Li$_{10}$GeP$_2$S$_{12}$ Lithium Super Ionic Conductor Material. *Chem. Mater.*, 24(1):15–17, jan 2012.

[18] Yizhou Zhu, Xingfeng He, and Yifei Mo. Origin of Outstanding Stability in the Lithium Solid Electrolyte Materials: Insights from Thermodynamic Analyses Based on First-Principles Calculations. *ACS Appl. Mater. Interfaces*, 7(42):23685–23693, 2015.

[19] Fudong Han, Yizhou Zhu, Xingfeng He, Yifei Mo, and Chunsheng Wang. Electrochemical Stability of Li10GeP2S12and Li7La3Zr2O12Solid Electrolytes. *Adv. Energy Mater.*, 6(8):1–9, 2016.

[20] William H Woodford, W Craig Carter, and Yet-Ming Chiang. Design criteria for electrochemical shock resistant battery electrodes. *Energy Environ. Sci.*, 5(7):8014, 2012.

[21] Wu Xu, Jiulin Wang, Fei Ding, Xilin Chen, Eduard Nasybulin, Yaohui Zhang, and Ji-Guang Zhang. Lithium metal anodes for rechargeable batteries. *Energy Environ. Sci.*, 7:513, 2014.

[22] Charles Monroe and John Newman. The Impact of Elastic Deformation on Deposition Kinetics at Lithium/Polymer Interfaces. *J. Electrochem. Soc.*, 152(2):A396, 2005.

[23] Zhi Deng, Yifei Mo, and Shyue Ping Ong. Computational studies of solid-state alkali conduction in rechargeable alkali-ion batteries. *NPG Asia Mater.*, 8(3):e254, 2016.

[24] Alexander Urban, Dong-Hwa Seo, and Gerbrand Ceder. Computational understanding of Li-ion batteries. *npj Comput. Mater.*, 2(October 2015):16002, 2016.

[25] Anubhav Jain, Shyue Ping Ong, Geoffroy Hautier, Wei Chen, William Davidson Richards, Stephen Dacek, Shreyas Cholia, Dan Gunter, David Skinner, Gerbrand Ceder, and Kristin A Persson. Commentary: The Materials Project: A materials genome approach to accelerating materials innovation. *APL Mater.*, 1(1):11002, 2013.

[26] Shyue Ping Ong, William Davidson Richards, Anubhav Jain, Geoffroy Hautier, Michael Kocher, Shreyas Cholia, Dan Gunter, Vincent L Chevrier, Kristin a. Persson, and Gerbrand Ceder. Python Materials Genomics (pymatgen): A robust, open-source python library for materials analysis. *Comput. Mater. Sci.*, 68:314–319, 2013.

[27] Anubhav Jain, Shyue Ping Ong, Wei Chen, Bharat Medasani, Xiaohui Qu, Michael Kocher, Miriam Brafman, Guido Petretto, Gian-Marco Rignanese, Geoffroy Hautier, Daniel Gunter, and Kristin A Persson. FireWorks: a dynamic workflow system designed for highthroughput applications. *Concurr. Comput. Pr. Exp.*, 27:5037–5059, 2015.

[28] P. Hohenberg and W. Kohn. Inhomogeneous electron gas. *Phys. Rev.*, 136(3B):B864, 1964.

[29] W. Kohn and L. J. Sham. Self-consistent equations including exchange and correlation effects. *Phys. Rev.*, 140(4A):A1133, 1965.

[30] Philipp Haas, Fabien Tran, and Peter Blaha. Calculation of the lattice constant of solids with semilocal functionals. *Phys. Rev. B - Condens. Matter Mater. Phys.*, 79(8):1–10, 2009.

[31] G Kresse and J Furthmüller. Efficient iterative schemes for \textit{ab initio} total-energy calculations using a plane-wave basis set. *Phys. Rev. B*, 54(16):11169–11186, oct 1996.

[32] P E Blöchl. Projector augmented-wave method. *Phys. Rev. B*, 50(24):17953–17979, 1994.

[33] Jp Perdew, K Burke, and M Ernzerhof. Generalized Gradient Approximation Made Simple. *Phys. Rev. Lett.*, 77(18):3865–3868, oct 1996.

[34] M. C. Payne, M. P. Teter, D. C. Allan, T. A. Arias, and J. D. Joannopoulos. Iterative minimization techniques for ab initio total-energy calculations: Molecular dynamics and conjugate gradients. *Rev. Mod. Phys.*, 64(4):1045–1097, 1992.

[35] Shyue Ping Ong, Yifei Mo, William Davidson Richards, Lincoln Miara, Hyo Sug Lee, and Gerbrand Ceder. Phase stability, electrochemical stability and ionic conductivity of the Li10Âś1MP2X12 (M = Ge, Si, Sn, Al or P, and X = O, S or Se) family of superionic conductors. *Energy Environ. Sci.*, 6(1):148, 2013.

[36] Zhi Deng, Zhuoying Zhu, Iek Heng Chu, and Shyue Ping Ong. Data-driven first-principles methods for the study and design of alkali superionic conductors. *Chem. Mater.*, 29(1):281–288, 2017.

[37] https://materialsproject.github.io/custodian/.

[38] Jörg Behler and Michele Parrinello. Generalized neural-network representation of high-dimensional potential-energy surfaces. *Phys. Rev. Lett.*, 98(14):1–4, 2007.

[39] Albert P. Bartók, Mike C. Payne, Risi Kondor, and Gábor Csányi. Gaussian approximation potentials: The accuracy of quantum mechanics, without the electrons. *Phys. Rev. Lett.*, 104(13):1–4, 2010.

[40] W. F. Kuhs, R. Nitsche, and K. Scheunemann. The argyrodites - A new family of tetrahedrally close-packed structures. *Mater. Res. Bull.*, 14(2):241–248, 1979.

[41] Hans-Jorg Deiseroth, Shiao-Tong Kong, Hellmut Eckert, Julia Vannahme, Christof Reiner, Torsten Zaiß, and Marc Schlosser. Li6PS5X: A class of crystalline Li-rich solids with an unusually high Li+ mobility. *Angew. Chemie Int. Ed.*, 47(4):755–758, 2008.

[42] Florian Stadler and Christopher Fietzek. Crystalline Halide Substituted Li-Argyrodites as Solid Electrolytes for Lithium Secondary Batteries. *ECS Trans.*, 25(36):177–183, 2010.

[43] Sylvain Boulineau, Matthieu Courty, Jean-Marie Tarascon, and Virginie Viallet. Mechanochemical synthesis of Li-argyrodite Li6PS5X (X=Cl, Br, I) as sulfur-based solid electrolytes for all solid state batteries application. *Solid State Ionics*, 221:1–5, 2012.

[44] Sylvain Boulineau, Jean-Marie Tarascon, Jean Bernard Leriche, and Virginie Viallet. Electrochemical properties of all-solid-state lithium secondary batteries using Li-argyrodite Li6PS5Cl as solid electrolyte. *Solid State Ionics*, 242:45–48, 2013.

[45] R Prasada Rao, N Sharma, V K Peterson, and S Adams. Formation and conductivity studies of lithium argyrodite solid electrolytes using in-situ neutron diffraction. *Solid State Ionics*, 230:72–76, 2013.

[46] Maohua Chen, Rayavarapu Prasada Rao, and Stefan Adams. High capacity all-solid-state Cu-Li2S/Li6PS5Br/In batteries. *Solid State Ionics*, 262:183–187, 2014.

[47] Maohua Chen, Rayavarapu Prasada Rao, and Stefan Adams. The unusual role of Li6PS5Br in all-solid-state CuS/Li6PS5Br/In-Li batteries. *Solid State Ionics*, 268(PB):300–304, 2014.

[48] Maohua Chen and Stefan Adams. High performance all-solid-state lithium/sulfur batteries using lithium argyrodite electrolyte. *J. Solid State Electrochem.*, 19(3):697–702, 2015.

[49] Maohua Chen, Xuesong Yin, M. V. Reddy, and Stefan Adams. All-solid-state MoS<inf>2</inf>/Li<inf>6</inf>PS<inf>5</inf>Br/In-Li batteries as a novel type of Li/S battery. *J. Mater. Chem. A*, 3(20):10698–10702, 2015.

[50] G Bergerhoff, R Hundt, R Sievers, and I D Brown. The inorganic crystal structure data base. *J. Chem. Inf. Comput. Sci.*, 23(2):66–69, 1983.

[51] Gus Hart and Rodney Forcade. Algorithm for generating derivative structures. *Phys. Rev. B*, 77(22):224115, jun 2008.

[52] Hao Min Chen, Chen Maohua, and Stefan Adams. Stability and ionic mobility in argyrodite-related lithium-ion solid electrolytes. *Phys. Chem. Chem. Phys.*, 17(25):16494–16506, 2015.

[53] C Bradford Barber, David P Dobkin, and Hannu Huhdanpaa. The quickhull algorithm for convex hulls. *ACM Trans. Math. Softw.*, 22(4):469–483, 1996.

[54] Shyue Ping Ong, Lei Wang, Byoungwoo Kang, and Gerbrand Ceder. Li-Fe-P-O2 Phase Diagram from First Principles Calculations. *Chem. Mater.*, 20(5):1798–1807, 2008.

[55] Shyue Ping Ong, Shreyas Cholia, Anubhav Jain, Miriam Brafman, Dan Gunter, Gerbrand Ceder, and Kristin a. Persson. The Materials Application Programming Interface (API): A simple, flexible and efficient API for materials data based on REpresentational State Transfer (REST) principles. *Comput. Mater. Sci.*, 97:209–215, feb 2015.

[56] Shyue Ping Ong, Yifei Mo, William Davidson Richards, Lincoln Miara, Hyo Sug Lee, and Gerbrand Ceder. Phase stability, electrochemical stability and ionic conductivity of the Li 10Âś1 MP 2 X 12 (M = Ge, Si, Sn, Al or P, and X = O, S or Se) family of superionic conductors. *Energy Environ. Sci.*, 6(1):148–156, 2013.

[57] M K Aydinol, A F Kohan, G Ceder, K Cho, and J Joannopoulos. Ab initio study of lithium intercalation in metal oxides and metal dichalcogenides. *Phys. Rev. B*, 56(3):1354–1365, 1997.

[58] Yan Wang, William Davidson Richards, Shyue Ping Ong, Lincoln J Miara, Jae Chul Kim, Yifei Mo, and Gerbrand Ceder. Design principles for solid-state lithium superionic conductors. *Nat. Mater.*, 14(10):1026–1031, 2015.

[59] http://guide.materialsvirtuallab.org/pymatgen-diffusion/.

[60] R P Rao and S Adams. Studies of lithium argyrodite solid electrolytes for all-solid-state batteries. *Phys. Status Solidi*, 208(8):1804–1807, 2011.

[61] Yoshikatsu Seino, Tsuyoshi Ota, Kazunori Takada, Akitoshi Hayashi, and Masahiro Tatsumisago. A sulphide lithium super ion conductor is superior to liquid ion conductors for use in rechargeable batteries. *Energy Environ. Sci.*, 7(2):627–631, 2014.

[62] Zhuoying Zhu, Iek-Heng Chu, Zhi Deng, and Shyue Ping Ong. Role of Na+ Interstitials and Dopants in Enhancing the Na+ Conductivity of the Cubic Na3PS4 Superionic Conductor. *Chem. Mater.*, 27(24):8318–8325, 2015.

[63] Iek-Heng Chu, Han Nguyen, Sunny Hy, Yuh-Chieh Lin, Zhenbin Wang, Zihan Xu, Zhi Deng, Ying Shirley Meng, and Shyue Ping Ong. Insights into the Performance Limits of the Li7P3S11 Superionic Conductor: A Combined First-Principles and Experimental Study. *ACS Appl. Mater. Interfaces*, 8:7843–7853, 2016.

[64] Hui Wu and Yi Cui. Designing nanostructured Si anodes for high energy. *Nano Today*, 7:414–429, 2012.

[65] Jennifer E Ni, Eldon D Case, Jeffrey S Sakamoto, Ezhiyl Rangasamy, and Jeffrey B Wolfenstine. Room temperature elastic moduli and Vickers hardness of hot-pressed LLZO cubic garnet. *J. Mater. Sci.*, 47(23):7978–7985, 2012.

[66] Jeff Wolfenstine, Hyungyung Jo, Yong-Hun Cho, Isabel N David, Per Askeland, Eldon D Case, Hyunjoong Kim, Heeman Choe, and Jeff Sakamoto. A preliminary investigation of fracture toughness of Li7La3Zr2O12 and its comparison to other solid Li-ionconductors. *Mater. Lett.*, 96:117–120, 2013.

[67] Yong-Hun Cho, Jeff Wolfenstine, Ezhiylmurugan Rangasamy, Hyunjoong Kim, Heeman Choe, and Jeff Sakamoto. Mechanical properties of the solid Li-ion conducting electrolyte: Li0.33La0.57TiO3. *J. Mater. Sci.*, 47(16):5970–5977, 2012.

[68] Spencer D Jackman and Raymond A Cutler. Effect of microcracking on ionic conductivity in LATP. *J. Power Sources*, 218:65–72, 2012.

[69] Atsushi Sakuda, Akitoshi Hayashi, and Masahiro Tatsumisago. Sulfide solid electrolyte with favorable mechanical property for all-solid-state lithium battery. *Sci. Rep.*, 3:2261, 2013.

[70] R M Spriggs. Expression for Effect of Porosity on Elastic Modulus of Polycrystalline Refractory Materials, Particularly Aluminum Oxide. *J. Am. Ceram. Soc.*, 44(12):628–629, 1961.

[71] Z Q Wang, M S Wu, G Liu, X L Lei, B Xu, and C Y Ouyang. Elastic Properties of New Solid State Electrolyte Material Li 10 GeP 2 S 12 : A Study from First-Principles Calculations. *Int. J. Electrochem. Sci.*, 9:562–568, 2014.

[72] John P Perdew, Kieron Burke, and Matthias Ernzerhof. Generalized Gradient Approximation Made Simple [Phys. Rev. Lett. 77, 3865 (1996)]. *Phys. Rev. Lett.*, 77:3865, feb 1996.

[73] John P Perdew, Adrienn Ruzsinszky, Gabor I Csonka, Oleg A Vydrov, Gustavo E Scuseria, Lucian A Constantin, Xiaolan Zhou, and Kieron Burke. Generalized gradient approximation for solids and their surfaces. *Phys. Rev. Lett.*, 100(13):136406, apr 2007.

[74] JiÅŹ\'\i Klimeš, David R Bowler, and Angelos Michaelides. Chemical accuracy for the van der Waals density functional. *J. Physics. Condens. Matter*, 22(2):22201, 2010.

[75] J B Goodenough, H Y.-P. Hong, and J A Kafalas. Fast Na+-ion Transport in Skeleton Structures. *Mater. Res. Bull.*, 11:203–220, 1976.

[76] H Y-P. Hong. Crystal structures and crystal chemistry in the system Na1+xZr2SixP3âĹŠxO12. *Mater. Res. Bull.*, 11(2):173–182, 1976.

[77] Xiaohua Yu, J B Bates, G E Jellison, and F X Hart. A Stable Thin-Film Lithium Electrolyte: Lithium Phosphorus Oxynitride. *J. Electrochem. Soc.*, 144(2):524, 1997.

[78] N J Dudney. Solid-state thin-film rechargeable batteries. *Mater. Sci. Eng. B*, 116(3 SPEC.ISS.):245–249, 2005.

[79] Venkataraman Thangadurai, Heiko Kaack, and Werner J F Weppner. Novel Fast Lithium Ion Conduction in Garnet-Type Li$_5$La$_3$M$_2$O$_{12}$ (M: Nb, Ta). *J. Am. Ceram. Soc.*, 34(27):437–440, jul 2003.

[80] Masashi Kotobuki, Hirokazu Munakata, Kiyoshi Kanamura, Yosuke Sato, and Toshihiro Yoshida. Compatibility of Li[sub 7]La[sub 3]Zr[sub 2]O[sub 12] Solid Electrolyte to All-Solid-State Battery Using Li Metal Anode. *J. Electrochem. Soc.*, 157(10):A1076, 2010.

[81] Junji Awaka, Norihito Kijima, Hiroshi Hayakawa, and Junji Akimoto. Synthesis and structure analysis of tetragonal Li7La3Zr2O12 with the garnet-related type structure. *J. Solid State Chem.*, 182(8):2046–2052, 2009.

[82] Yusheng Zhao and Luke L Daemen. Superionic conductivity in lithium-rich anti-perovskites. *J. Am. Chem. Soc.*, 134(36):15042–15047, sep 2012.

[83] Yi Zhang, Yusheng Zhao, and Changfeng Chen. \textit{Ab initio} study of the stabilities of and mechanism of superionic transport in lithium-rich antiperovskites. *Phys. Rev. B*, 87(13):134303, apr 2013.

[84] Alexandra Emly, Emmanouil Kioupakis, and Anton Van der Ven. Phase Stability and Transport Mechanisms in Antiperovskite Li$_3$OCl and Li$_3$OBr Superionic Conductors. *Chem. Mater.*, 25(23):4663–4670, 2013.

[85] Zhi Deng, Balachandran Radhakrishnan, and Shyue Ping Ong. Rational Composition Optimization of the Lithium-Rich Li 3 OCl 1- x Br x Anti-Perovskite Superionic Conductors. *Chem. Mater.*, 27:3749–3755, 2015.

[86] Yonggang Wang, Qingfei Wang, Zhenpu Liu, Zhengyang Zhou, Shuai Li, Jinlong Zhu, Ruqiang Zou, Yingxia Wang, Jianhua Lin, and Yusheng Zhao. Structural manipulation approaches towards enhanced sodium ionic conductivity in Na-rich antiperovskites. *J. Power Sources*, 293:735–740, 2015.

[87] Zengcai Liu, Wujun Fu, E Andrew Payzant, Xiang Yu, Zili Wu, Nancy J Dudney, Jim Kiggans, Kunlun Hong, Adam J Rondinone, and Chengdu Liang. Anomalous High Ionic Conductivity of Nanoporous β âĂŚ Li 3 PS 4. *J. Am. Chem. Soc.*, 135(3):975–978, 2013.

[88] Philipp Bron, Sebastian Johansson, Klaus Zick, Jörn Schmedt auf der Günne, Stefanie Susanne Dehnen, and Bernhard Roling. Li10SnP2S12 - An Affordable Lithium Superionic Conductor Li 10 SnP 2 S 12 - An Affordable Lithium Superionic Conductor. *J. Am. Chem. Soc.*, 135(42):15694–15697, 2013.

[89] Alexander Kuhn, Oliver Gerbig, Changbao Zhu, Frank Falkenberg, Joachim Maier, and Bettina V Lotsch. A new ultrafast superionic Li-conductor: ion dynamics in Li$_{11}$Si$_2$PS$_{12}$ and comparison with other tetragonal LGPS-type electrolytes. *Phys. Chem. Chem. Phys.*, 16(28):14669–14674, 2014.

[90] H Yamane, M Shibata, Y Shimane, T Junke, Y Seino, S Adams, K Minami, a Hayashi, and M Tatsumisago. Crystal structure of a superionic conductor, Li7P3S11. *Solid State Ionics*, 178(15-18):1163–1167, jun 2007.

[91] Akitoshi Hayashi, Kousuke Noi, Atsushi Sakuda, and Masahiro Tatsumisago. Superionic glass-ceramic electrolytes for room-temperature rechargeable sodium batteries. *Nat. Commun.*, 3:856, may 2012.

[92] Naoto Tanibata, Kousuke Noi, Akitoshi Hayashi, Naoto Kitamura, Yasushi Idemoto, and Masahiro Tatsumisago. X-ray Crystal Structure Analysis of Sodium-Ion Conductivity in 94 Na 3 PS 4 âŃĚ6 Na 4 SiS 4 Glass-Ceramic Electrolytes. *ChemElectroChem*, 1(7):1130–1132, 2014.

[93] JiÅŹ\'\i Klimeš, David R Bowler, and Angelos Michaelides. Van der Waals density functionals applied to solids. *Phys. Rev. B*, 83(19):195131, may 2011.

[94] Maarten de Jong, Wei Chen, Thomas Angsten, Anubhav Jain, Randy Notestine, Anthony Gamst, Marcel Sluiter, Chaitanya Krishna Ande, Sybrand Van Der Zwaag, Jose J Plata, Cormac Toher, Stefano Curtarolo, Gerbrand Ceder, Kristin a Persson, and Mark Asta. Charting the complete elastic properties of inorganic crystalline compounds. *Sci. Data*, 2, 2015.

[95] Yvon Le Page and Paul Saxe. Symmetry-general least-squares extraction of elastic data for strained materials from ab initio calculations of stress. *Phys. Rev. B*, 65(10):104104, 2002.

[96] R Hill. The Elastic Behaviour of a Crystalline Aggregate. *Proc. Phys. Soc. Sect. A*, 65(5):349–354, 2002.

[97] Max Born. On the stability of crystal lattices. I. *Math. Proc. Cambridge Philos. Soc.*, 36(02):160, apr 1940.

[98] Félix Mouhat and François-Xavier Coudert. Necessary and sufficient elastic stability conditions in various crystal systems. *Phys. Rev. B*, 90:224104, 2014.

[99] W Buehrer, F Altorfer, J Mesot, H Bill, P Carron, and H G Smith. Lattice dynamics and the diffuse phase transition of lithium sulphide investigated by coherent neutron scattering. *J. Phys. Condens. Matter*, 3(9):1055–1064, 1991.

[100] S Hull, T W D Farley, W Hayes, and M T Hutchings. The elastic properties of lithium oxide and their variation with temperature. *J. Nucl. Mater.*, 160(2-3):125–134, 1988.

[101] B Bertheville, D Low, H Bill, and F Kubel. Ionic conductivity of Na2S single crystals between 295 and 1350 K experimental setup and first results. *J. Phys. Chem. Solids*, 58(10):1569–1577, 1997.

[102] W Buhrer and H Bill. Phononen-Dispersion in Na2S. *Helv. Phys. Acta*, 50(4):431–438, 1977.

[103] N Bernstein, M Johannes, and Khang Hoang. Origin of the Structural Phase Transition in Li_{7}La_{3}Zr_{2}O_{12}. *Phys. Rev. Lett.*, 109(20):205702, nov 2012.

[104] S F Pugh. XCII. Relations between the elastic moduli and the plastic properties of polycrystalline pure metals. *Philos. Mag. Ser. 7*, 45(367):823–843, 1954.

[105] Shun-Li Shang, Louis G Hector, Siqi Shi, Yue Qi, Yi Wang, and Zi-Kiu Liu. Lattice dynamics, thermodynamics and elastic properties of monoclinic Li2CO3 from density functional theory. *Acta Mater.*, 60(13-14):5204–5216, 2012.

[106] Y Qi, L G Hector, C James, and K J Kim. Lithium Concentration Dependent Elastic Properties of Battery Electrode Materials from First Principles Calculations. *J. Electrochem. Soc.*, 161(11):F3010—-F3018, 2014.

[107] Jan N Reimers and J R Dahn. Electrochemical and in situ XâĂŘray diffraction studies of lithium intercalation in Li x CoO2. *J. Electrochem. Soc.*, 139(8):2091–2097, 1992.

[108] Nongluk Meethong, Hsiao Ying Shadow Huang, Scott A Speakman, W Craig Carter, and Yet Ming Chiang. Strain accommodation during phase transformations in olivine-based cathodes as a materials selection criterion for high-power rechargeable batteries. *Adv. Funct. Mater.*, 17(7):1115–1123, 2007.

[109] Motohiro Nagao, Akitoshi Hayashi, Masahiro Tatsumisago, Tsukasa Kanetsuku, Tetsuya Tsuda, and Susumu Kuwabata. In situ SEM study of a lithium deposition and dissolution mechanism in a bulk-type solid-state cell with a Li2S-P2S5 solid electrolyte. *Phys. Chem. Chem. Phys.*, 15(42):18600–18606, 2013.

[110] Yaoyu Ren, Yang Shen, Yuanhua Lin, and Ce-Wen Nan. Direct observation of lithium dendrites inside garnet-type lithium-ion solid electrolyte. *Electrochem. commun.*, 57:27–30, 2015.

[111] Rodolpho Mouta, Maria A B Melo, Eduardo M Diniz, and Carlos William A Paschoal. Concentration of Charge Carriers, Migration, and Stability in Li$_3$OCl Solid Electrolytes. *Chem. Mater.*, 26(24):7137–7144, 2014.

[112] A Van der Ven, G Ceder, M Asta, and P Tepesch. First-principles theory of ionic diffusion with nondilute carriers. *Phys. Rev. B*, 64(18):184307, oct 2001.

[113] Loup Verlet. Computer “Experiments" on Classical Fluids. I. Thermodynamical Properties of Lennard-Jones Molecules. *Phys. Rev.*, 159(5):98, 1967.

[114] Shuichi Nose, Shuichi Nosé, and Shuichi NoseÌĄ. A unified formulation of the constant temperature molecular dynamics methods. *J. Chem. Phys.*, 81(1984):511–519, 1984.

[115] William G Hoover. Canonical dynamics: Equilibrium phase-space distributions. *Phys. Rev. A*, 31(3):1695–1697, 1985.

[116] M E J Newman and R M Ziff. Efficient Monte Carlo Algorithm and High-Precision Results for Percolation. *Phys. Rev. Lett.*, 85(19):4104–4107, 2000.

[117] Christian D Lorenz and Robert M Ziff. Precise determination of the bond percolation thresholds and finite-size scaling corrections for the s.c., f.c.c., and b.c.c. lattices. *Phys. Rev. E*, 57(1):230–236, 1998.

[118] Xujie Lü, Gang Wu, John W Howard, Aiping Chen, Yusheng Zhao, Luke L Daemen, and Quanxi Jia. Li-rich anti-perovskite Li$_3$OCl films with enhanced ionic conductivity. *Chem. Commun.*, 50(78):11520–11522, 2014.

[119] S Stramare, V Thangadurai, and W Weppner. Lithium Lanthanum Titanates: A Review. *Chem. Mater.*, 15(21):3974–3990, 2003.

[120] Alexander Urban, Jinhyuk Lee, and Gerbrand Ceder. The Configurational Space of Rocksalt-Type Oxides for High-Capacity Lithium Battery Electrodes. *Adv. Energy Mater.*, 4:1000478, 2014.

[121] Jinhyuk Lee, Alexander Urban, Xin Li, Dong Su, Geoffroy Hautier, and Gerbrand Ceder. Unlocking the Potential of Cation-Disordered Oxides for Rechargeable Lithium Batteries. *Science.*, 343(January):519–522, 2014.

[122] T Ishihara, H Matsuda, and Y Takita. Doped LaGaO$_3$ Perovskite Type Oxide as a New Oxide Ionic Conductor. *J. Am. Chem. Soc.*, 116(9):3801–3803, 1994.

[123] Keqin Huang, Robin S Tichy, and John B Goodenough. Superior Perovskite Oxide-Ion Conductor; Strontium-and Magnesium-Doped LaGaO$_3$: I, Phase Relationships and Electrical Properties. *J. Am. Ceram. Soc.*, 81(10):2565, 1998.

[124] A P Thompson, L P Swiler, C R Trott, S M Foiles, and G J Tucker. Spectral neighbor analysis method for automated generation of quantum-accurate interatomic potentials. *J. Comput. Phys.*, 285:316–330, mar 2015.

[125] Nongnuch Artrith, Tobias Morawietz, and Jörg Behler. High-dimensional neural-network potentials for multicomponent systems: Applications to zinc oxide. *Phys. Rev. B*, 83:153101, 2011.

[126] Albert P Bartók, Risi Kondor, and Gábor Csányi. On representing chemical environments. *Phys. Rev. B - Condens. Matter Mater. Phys.*, 87(18):1–16, 2013.

[127] Alexander V Shapeev. Moment tensor potentials: A class of systematically improvable interatomic potentials. *Multiscale Model. Simul.*, 14(3):1153–1173, 2016.

[128] Jörg Behler. Atom-centered symmetry functions for constructing high-dimensional neural network potentials. *J. Chem. Phys.*, 134:74106, 2011.

[129] Mitchell A Wood and Aidan P Thompson. Extending the accuracy of the SNAP interatomic potential form. *J. Chem. Phys.*, 148(24), 2018.

[130] Chi Chen, Zhi Deng, Richard Tran, Hanmei Tang, Iek-Heng Chu, and Shyue Ping Ong. Accurate Force Field for Molybdenum by Machine Learning Large Materials Data. *Phys. Rev. Mater.*, 1:43603, 2017.

[131] Xiang-Guo Li, Chongze Hu, Chi Chen, Zhi Deng, Jian Luo, and Shyue Ping Ong. Quantum-Accurate Spectral Neighbor Analysis Potential Models for Ni-Mo Binary Alloys and FCC Metals. *arXiv Prepr.*, 2018.

[132] G V Lewis and C R A Catlow. Potential models for ionic oxides. *J. Phys. C Solid State Phys.*, 18:1149, 1985.

[133] Eunkoo Lee, Kwang Ryeol Lee, M I Baskes, and Byeong Joo Lee. A modified embedded-atom method interatomic potential for ionic systems: 2NNMEAM+Qeq. *Phys. Rev. B*, 93:144110, 2016.

[134] P P Ewald. Die Berechnung optischer und elektrostatischer Gitterpotentiale. *Ann. Phys.*, 369(3):253–287, 1921.

[135] J F Ziegler, J P Biersack, and U Littmark. *The stopping and range of ions in matter, Vol. 1*. Pergamon Press, New York, 1985.

[136] Steve Plimpton. Fast Parallel Algorithms for Short-Range Molecular Dynamics. *J. Comput. Phys.*, 117(1):1–19, 1995.

[137] J R Walker and C R A Catlow. Defect structure and ionic conductivity in lithium nitride. *Philos. Mag. A*, 43(2):265–272, 1981.

[138] A Rabenau and Heinz Schulz. Re-evaluation of the lithium nitride structure. *J. Less-Common Met.*, 50(1):155–159, 1976.

[139] W Kress, H Grimm, W Press, and J Lefebvre. Lattice vibrations in lithium nitride, Li3N. *Phys. Rev. B*, 22(10):4620–4625, 1980.

[140] Ippei Kishida, Fumiyasu Oba, Yukinori Koyama, Akihide Kuwabara, and Isao Tanaka. Variable anisotropy of ionic conduction in lithium nitride: Effect of duplex-charge transfer. *Phys. Rev. B - Condens. Matter Mater. Phys.*, 80(2):1–6, 2009.

[141] Atsushi Togo and Isao Tanaka. First principles phonon calculations in materials science. *Scr. Mater.*, 108:1–5, 2015.

[142] Gang Wu, Shunnian Wu, and Ping Wu. Doping-enhanced lithium diffusion in lithium-ion batteries. *Phys. Rev. Lett.*, 107(11):1–5, 2011.

[143] Sondre K Schnell, Xin Liu, Jean Marc Simon, André Bardow, Dick Bedeaux, Thijs J H Vlugt, and Signe Kjelstrup. Calculating thermodynamic properties from fluctuations at small scales. *J. Phys. Chem. B*, 115(37):10911–10918, 2011.

[144] M L Wolf, J R Walker, and C R A Catlow. A molecular dynamics simulation study of the superionic conductor lithium nitride. I. *J. Phys. C Solid State Phys.*, 17(36):6623–6634, 1984.

[145] Wen Li, Guotao Wu, C Moysés Araújo, Ralph H Scheicher, Andreas Blomqvist, Rajeev Ahuja, Zhitao Xiong, Yuanping Feng, and Ping Chen. Li+ion conductivity and diffusion mechanism in α-Li3N and β-Li3N. *Energy Environ. Sci.*, 3(10):1524–1530, 2010.

[146] J Tersoff. Modeling solid-state chemistry: Interatomic potentials for multicomponent systems. *Phys. Rev. B*, 39(8):5566–5568, 1989.

[147] William D Richards, Yan Wang, Lincoln J Miara, Jae Chul Kim, and Gerbrand Ceder. Design of Li 1+2x Zn 1âĹŠx PS 4 , a new lithium ion conductor. *Energy Environ. Sci.*, 9(10):3272–3278, 2016.